Progress Towards the Creation of an On-Demand Single Photon Source Using Rydberg Atoms

by

Jason Owen Day

A dissertation submitted in partial fulfillment

of the requirements for the degree of

Doctor of Philosophy

(Physics)

at the

UNIVERSITY OF WISCONSIN-MADISON

2008

0.1 Abstract

This dissertation describes experiments performed on Rydberg atoms in order to facilitate the construction of an on-demand, single-photon source. We performed two-photon excitation on atoms in a Magneto-Optical Trap (MOT) up to high n-level Rydberg states. We developed a novel technique for measuring the linewidths of atomic transitions at timescales shorter than 100 μs, and measured the linewidths of the $5S \rightarrow nS, D$ Rydberg transitions to be 8 MHz for Rydberg principal quantum number 28, 43, and 58. We also employ another novel technique, a state-probe laser which stimulates atomic emission out of the Rydberg level and allows us to observe the timescale of Rydberg atom transitions.

By employing the state-probe laser and observing trap loss from the MOT, we are able to determine that atoms are transferred out of the Rydberg state faster than collisional processes and blackbody transition rates. We have developed a model of superradiance which predicts the transition rates we observe in the experiment. Based on this, we have concluded that superradiant emission out of the Rydberg excitation state is a much greater factor in the μs-scale Rydberg transfer rates observed in the literature than any other study had previously reported.

We have performed non-degenerate four-wave mixing through Rydberg states using a non-collinear geometry as a precursor to an on-demand, single-photon source. In addition, this is among the first demonstrations of the coherent manipulations of Rydberg atoms found in the literature. We have developed a model of four-wave mixing that agrees with our observations of the phase-matched count rate and fraction of phase-matched light to within a factor of 3. With the excitation beams detuned from the two-photon Rydberg transition, we observe up to 50% of the emitted light radiated into the preferred phase-matched direction.

CONTENTS

LIST OF FIGURES

LIST OF TABLES

1. INTRODUCTION

1.1 Motivation

The goal of efficient quantum information processing has been one of the driving forces in the field of atomic physics for some years now. It was Richard Feynman who first conceived of using an ensemble of quantum objects (or qubits) as a type of computer, though he envisioned using the ensemble to model physical quantum systems. Interest has also arisen in using these ensembles for quantum computation, using the qubits as a type of Turing machine to perform operations.

Many of the details of quantum computing are outside the scope of this work and can be found elsewhere [Nielsen *et al.*, 2000], but in short the interest in quantum computation comes from the entanglement that may be exhibited by pairs of qubits. That is, pairs of qubits may interact in such a way that the state of one object cannot be written without referring to the state of the other. As an example, if two qubits $|a\rangle$ and $|b\rangle$ can be in state 0 or 1, then an (unnormalized) entangled state would look like $|ab\rangle = |01\rangle + |10\rangle$. This quantum entanglement can be used to perform some operations faster than with a classical computer [Shor, 1996], [Grover, 1996].

In order to produce a usable ensemble of qubits, however, a number of conditions must be met [DiVincenzo, 2000]. To mention but a few, one must be able to initialize and manipulate the quantum state of individual qubits of the ensemble, and the interaction of the qubits with their environment must be slow enough that many state-

changing operations can be performed on the qubits before coupling to the environment results in decoherence of the qubits. It would also be useful to transmit entangled information from one ensemble to another using, for example, polarization states of a photon to encode the information.

Atom traps are good candidates for quantum information protocols because the atoms can be localized for up to a few seconds, a time much longer than the timescale for state-changing operations (typically $\sim$1 μs or faster). In addition, the energy levels of atoms in the trap provide quasi two-level systems that can be used as qubits, and lasers tuned to the transition frequency between the two levels can be used to change the state of the qubit. The difficulty arises when attempting to address individual atoms by laser excitation since atom traps typically contain thousands to millions of atoms. It is possible to reduce the atomic loading rate into the trap so that on average only one atom is present in the trap [Yavuz *et al.*, 2006]; however this is a statistical average and thus the trap will often have zero, two, or more atoms confined. This is undesirable, thus it would be expedient to be able to trap a single atom, on demand, which could then be used as a qubit in a quantum computation of some form.

Lukin *et al.*,'s proposal of a dipole blockade [Lukin *et al.*, 2001] using Rydberg atoms has the potential to provide just such a source of on-demand single atoms for quantum information protocols. In the dipole blockade, one atom out of an ensemble of trapped atoms is excited to a high-level Rydberg state via laser excitation. The dipole moment of this Rydberg atom causes interactions with neighboring atoms in the ground state which shift the energy levels of these atoms. If this energy shift is large enough, the laser which excited the initial Rydberg atom will not be resonant with the ground-to-Rydberg transition of the surrounding atoms, and thus none of these atoms will be excited to the Rydberg level. If the size of the ensemble is small enough that the energy levels of all of the atoms in the ensemble are shifted out of resonance with

the excitation laser, then we say - somewhat whimsically - that the single Rydberg atom has established a "blockade" that prevents subsequent Rydberg atom excitation. This effect has recently been observed between two atoms separated by 10 μm by my colleagues in the Quantum Computing group here at the University of Wisconsin [Urban *et al.*, 2008]. If a second laser resonant with some other ground-to-excited state transition is then applied to the atoms, the atoms may be "pushed" out of the trap while only the Rydberg atom remains, thus producing, in theory, a single atom in the trap with a high level of fidelity [Saffman and Walker, 2002]. Additionally, if this atom can be made to radiate a photon in a pre-determined direction upon decaying from the Rydberg state, this would produce a single-photon source.

An efficient, on-demand, single-photon source that could produce single photons at a rate of $\sim$MHz would also be of great use to the goal of quantum information processing. Using such a source, it is possible to implement potentially unbreakable quantum cryptographic protocols based on Quantum Key Distribution (QKD) [Gisin *et al.*, 2002]. In addition, in a paper by Knill *et al.* [Knill *et al.*, 2001], a proposal for using passive linear optics to perform quantum gates using photons with qubit information encoded in polarization states is presented. This Linear Optic Quantum Computation (LOQC) scheme requires a high-rate, single-photon source such as that which could potentially be developed in this setup. Thus, single-photon sources could be used in theory for many of the same applications discussed for atom-based quantum information processing. Other possible uses include random number generation [Rarity *et al.*, 1994], quantum information transmission, and experimental tests of Bell's inequalities [Pan *et al.*, 2000].

At the moment, such experiments usually involve parametric down-conversion, which uses a nonlinear crystal to convert a pump photon into signal and idler photons, providing a heralded source of single photons. The difficulty here is that this

source has a Poissonian photon number distribution, so to prevent multiple photon transmission, the fluence rate must be drastically reduced. The benefit of an atomic source utilizing a strong dipole blockade is that a sub-Poissonian photon number distribution is guaranteed with no need to reduce the fluence rate.

1.2 Summary of Thesis

It is upon this premise of the design of a single-photon source that this thesis is predicated. All of the experiments described within have been performed in order to obtain a better understanding of Rydberg atom physics so that in the near future a single-photon source may be implemented using this experimental apparatus. I will begin the thesis with a description of the experimental apparatus. We use 10^8 Rubidium-87 atoms in a Magneto-Optical Trap (MOT) as our ensemble of quantum objects. Two lasers, a 780 nm laser and a 480 nm laser, are used to excite atoms from the $5S$ ground state in the MOT up to an S- or D-level Rydberg state. The 780 nm laser is an external cavity diode laser purchased from Toptica, while the 480 nm laser was built in the lab using a 960 nm diode which is amplified and then frequency doubled in a cavity containing a periodically-poled Potassium Titanyl-Phosphate (PPKTP) crystal. A 1015 nm diode laser is used to de-excite the atoms from the Rydberg level to the $6P_{3/2}$ state, and two photon-counting modules are used to collect the decay photons from the $6P_{3/2} \rightarrow 5S_{1/2}$ transition. The 480 and 1015 nm lasers can each be focused to a 12 μm spot at the atoms, and the 39° angle of intersection between the 480 nm and 780 nm lasers defines the Rydberg excitation volume.

The third chapter discusses the theory and implementation of frequency doubling used in the construction of the 480 nm laser. I present the equation for frequency doubling of plane waves in a nonlinear crystal. Using this as a starting point, I discuss

modifications to this equation based on the strong focusing of the 960 nm pump in the crystal, as well as the concept of quasi-phase matching. I calculate the range of temperatures for which the PPKTP crystal will be properly phase-matched, and then work out the expected single pass conversion efficiency of the 960 nm pump into 480 nm light. I then discuss the design of the optical cavity containing the doubling crystal and detail a procedure for aligning the cavity.

Next I turn to a series of two-photon excitation experiments we performed in order to evaluate our control over the Rydberg excitation process. Surprisingly, we find that our Rydberg transition linewidths are 8-10 MHz wide, wider than we would expect from doppler broadening or excitation laser linewidths. I then present a novel technique for measuring the Rydberg transition linewidths at timescales on the order of 100 μs and shorter. The measurements using this technique verify the 8 MHz linewidths of our two-photon Rydberg excitation. I discuss our attempts to coherently excite atoms to the Rydberg state and then de-excite back to the ground state using stimulated Raman adiabatic passage. These attempts were ultimately unsuccessful as decoherence mechanisms prevent coherent de-excitation from the Rydberg state. Finally, we dressed the Rydberg D-state with a nearby F-state using resonant microwave fields in order to create dipole-dipole interactions among the Rydberg atoms.

The content of Chapters 5 and 6 covers the same content described in our most recent publication [Day *et al.*, 2008]. In this article, we excited Rydberg atoms at lower densities than the groups that observe signatures of plasma formation. At these densities, we found atoms were still transferred out of the Rydberg state much faster than would be effected by blackbody radiation. We developed a "state-probe" laser to de-excite the atoms from the excitation Rydberg state before atoms could be transferred to another state and thus obtained information about the rate of this transfer process. Using a simplified three level model for Rydberg atom interactions, we were able to

quantify the transfer rate out of the excitation Rydberg state and show that collisional processes could not be the primary cause of this transfer. In Chapter 6, I posit that superradiant decay of Rydberg atoms from the excitation state is the cause of the observed transfer rates. A model of collective emission from Rydberg atoms in the MOT was developed and based on this a transfer rate was calculated which agreed well with our observed transfer rates. Finally, I argue that blackbody ionization from these other Rydberg states is likely to be the cause of the observed MOT trap loss.

Chapter 7 presents our experiments using phase-matched four-wave mixing in a non-collinear geometry with intermediate Rydberg states, as described in our recently submitted paper [Brekke *et al.*, 2008]. This geometry provides an excellent setup for our proposed single-photon source since photons are preferentially emitted in a narrow cone which is not coincident with any other laser in the system. We compared the phase-matched signal to the total amount of light radiated by the atoms and find that as much as 50% of the light is emitted in the phase-matched direction. We then developed a model of four-wave mixing by calculating the dipole moments of the atoms in the sample and find that the calculated photon emission rates agree with the observed rates for both the phase-matched and non-phase-matched light to within a factor of 3.

The final chapter looks to the future of the experiment and to the steps that remain before the implementation of a true on-demand, single-photon source. Although some methods exist for obtaining sources of single photons, such as the aforementioned parametric down-conversion [Barreiro *et al.*, 2008], single atoms in ultra-high-finesse cavities [McKeever *et al.*, 2004], and other methods such as photoluminescence of carbon nanotubes [Högele *et al.*, 2008], a reliable, efficient, on-demand manner of creating indistinguishable single photons would be a great aide to the field of quantum information processing. With the work presented in this thesis, that goal is nearer to actualization.

2. EXPERIMENTAL SETUP

2.1 Introduction

In this chapter, I will describe the experimental apparatus used to excite and detect Rydberg atoms in the magneto-optical trap. I begin with a brief description of the MOT, including the generation of the trapping laser from a Titanium:Sapphire cavity, the repumping laser, and the magnetic field. The MOT we generate contains 10^8 atoms at an average density of 10^{10} cm^{-3}. Next I will focus on the Rydberg excitation lasers, both diode-laser-based, at 780 nm and 480 nm. These lasers deliver 15 mW and 5 mW, respectively, to the MOT and have locking linewidths (as described in the text) of 200 kHz and 2 MHz respectively. The 480 nm laser is stabilized to an external reference cavity, the length of which can be varied in order to change the frequency of the 480 nm laser. By scanning the 480 nm laser frequency in this fashion across the $5P \rightarrow nS, D$ Rydberg transition, we perform spectroscopy on the Rydberg state.

I then turn to the 1015 nm de-excitation laser which is used to bring Rydberg atoms down to the $6P_{3/2}$ state. This diode laser is similarly stabilized to an external cavity, although the length of this cavity is stabilized to a frequency-shifted portion of the 780 nm trapping laser. By changing the magnitude of the frequency shift from the 780 nm beam, we can change the frequency of the 1015 nm laser and thus perform spectroscopy on the n$S, D \rightarrow 6P$ transition. Two photon counting modules are used to detect photons from the decay of the $6P$ state and a photodiode collects photons

from the fluorescence of the $5P \rightarrow 5S$ cycling transition in the MOT. Finally, I discuss the optics trains which deliver the 480 and 1015 nm lasers to the MOT. The lasers are each focused down to a 12 μm spot at the atoms. The position of the final focusing lens can be changed so that the lasers are unfocused at the atoms and cover the spatial extent of the MOT.

2.2 Magneto-Optical Trap

2.2.1 Ti:Sapph

We use 780 nm laser light to trap 10^8 ^{87}Rb atoms in a vacuum chamber at 10^{-10} torr. The main trapping laser is a Titanium:Sapphire (Ti:Sapph) laser pumped by an 8W Argon-ion laser. This Ti:Sapph laser is frequency stabilized by means an FM-spectroscopy-based Doppler-free spectroscopy lock, as described here [Newell, 2003]. The Doppler-free spectroscopy lock uses a vapor cell containing a small amount of room-temperature Rubidium gas. Figure 2.1 shows the structure of the ground state and first two excited states of ^{87}Rb, which will facilitate the discussion of the trapping of Rb that follows.

The light passing through the vapor cell is frequency modulated by an Electro-Optic Modulator (EOM) and some of it is absorbed by the Rubidium vapor in the cell when the frequency of the light coincides with a saturated absorption resonance [Newell, 2003]. We tune the Ti:Sapph laser to the $5S$-$5P_{3/2}$ hyperfine manifold in order to trap Rubidium atoms on the F=2, F'=3 hyperfine transition. We stabilize the Ti:Sapph laser to the crossover peak halfway between the F'=3, and F'=1 transitions, 212 MHz below the F'=3 transition. 500 mW of the 1W output of the Ti:Sapph cavity is diverted to an acousto-optic modulator (AOM). This beam is double-passed through the AOM and frequency shifted up by 197 MHz, to 15 MHz below the $5S, F$=2 to

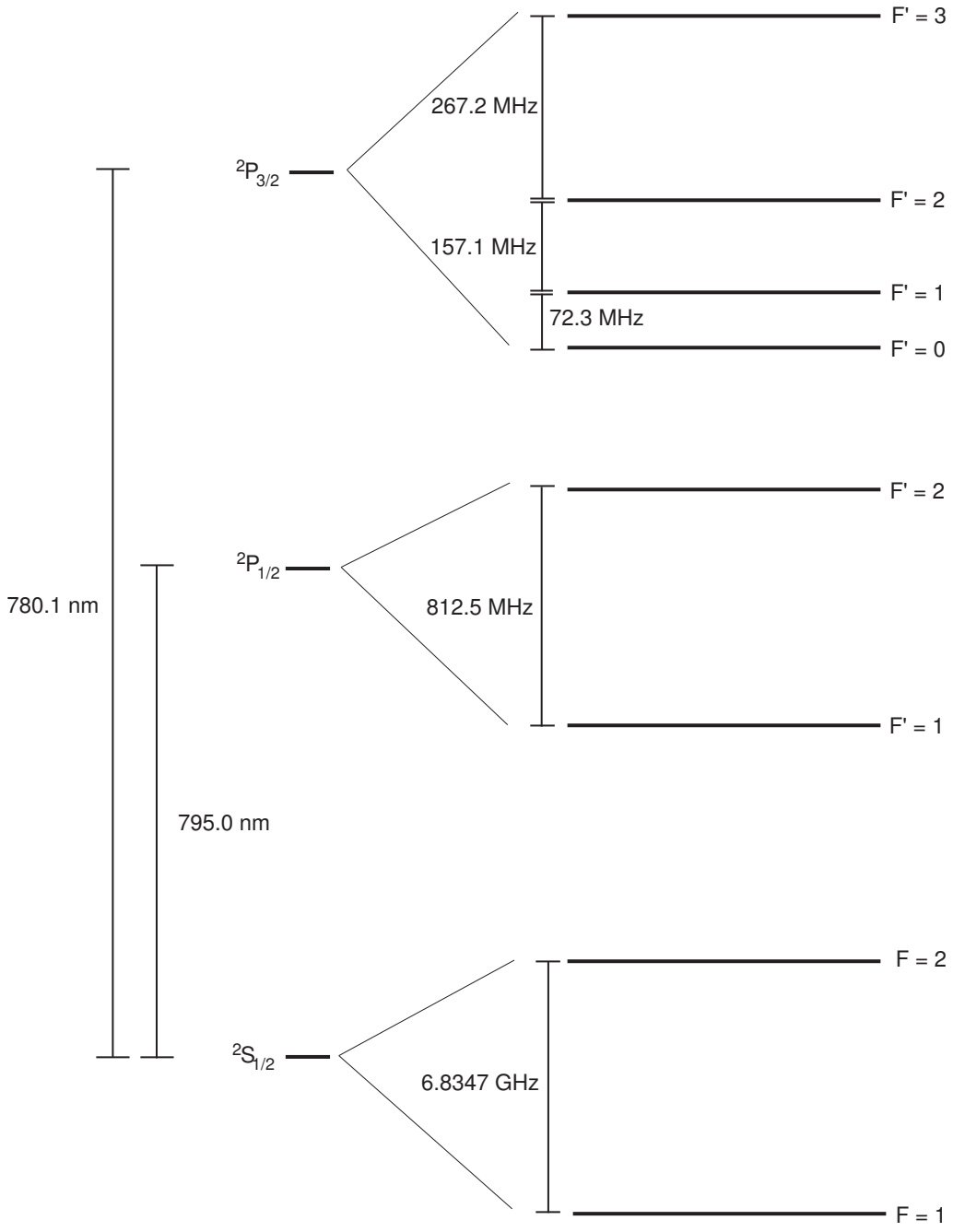

Fig. 2.1: Diagram of the ground state hyperfine structure of ^{87}Rb as well as the first two excited states and the transition wavelengths to each.

$5P_{3/2}, F$'=3 transition. This constitutes the trapping beam for the MOT. It is divided into four separate beams: one in the vertical direction which is retro-reflected, and three along the horizontal plane which are not. Figure 2.2 shows a vertical view of the vacuum chamber with the MOT lasers in the horizontal plane. The most intense of the three horizontal beams makes a 135° angle with the other two beams, and the intensities of all three beams are set so that the atoms experience an equal force in all directions in the plane. The beams are red detuned from resonance, so the greater an atom's momentum in the direction of one of these beams, the greater the Doppler shift of that beam relative to the atom. Such an atom will absorb more photons than an atom at rest in the lab frame, since the Doppler shift brings the laser light closer onto resonance with the atom. The end result is that the momentum of the atoms is reduced over time by many velocity-selective absorptions and re-emissions.

Thus the trapping beams reduce the velocity of the atoms, but it is also necessary to confine the atoms in the center of the beams with a magnetic field [Newell, 2003]. With this in mind, current is run through a pair of coils attached to the vacuum chamber in an anti-Helmholz configuration to produce a magnetic field in the vacuum chamber. The coils produce a magnetic field gradient of 20 Gauss/cm at the trap.

In this way, we load ^{87}Rb atoms from a background vapor into our trap. In steady-state, the trap contains 10^8 atoms as measured from fluorescence counts (see section 2.4) and has a roughly Gaussian spatial profile with a 0.7 mm 1/e radius in each direction. In some of our experiments it is necessary to switch off the trapping lasers or the magnetic field, which will cause a marked reduction in the number of trapped atoms. The trapping lasers can be toggled by turning on and off the RF signal to the AOM that produces the trapping frequency. The magnetic field can also be switched on and off, however, at a much slower frequency. Residual current in the coils takes 3 ms to damp out. Since we want the magnetic field damping time $\tau_B \ll \mathrm{T}_B$, the period

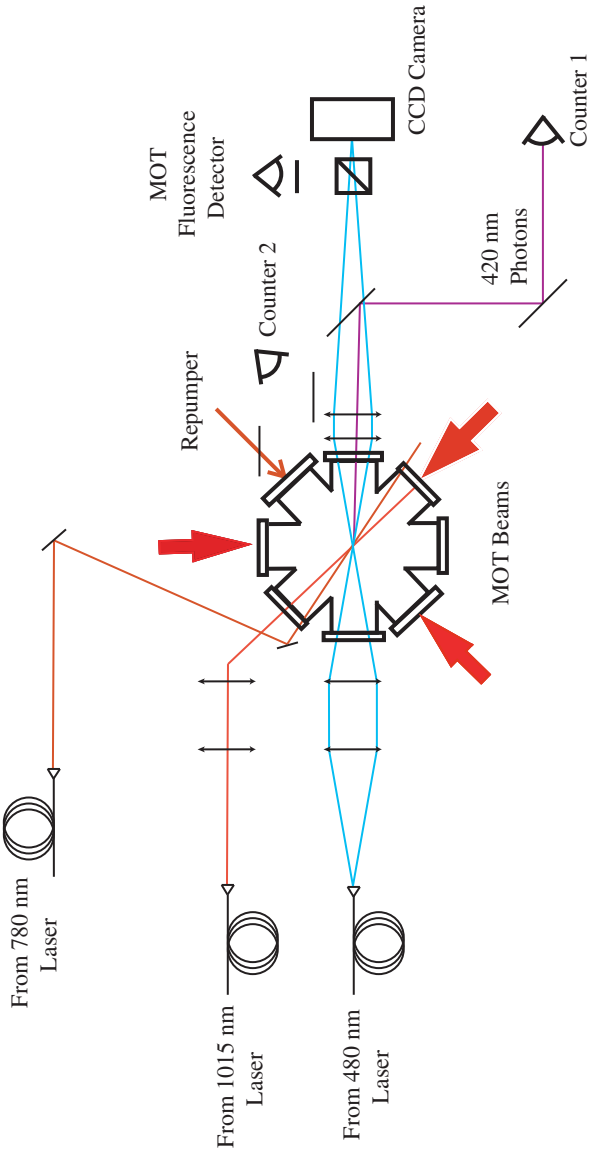

Fig. 2.2: A drawing of the vacuum chamber showing all lasers and relevant optics involved in the experiment. The five-beam MOT uses three trapping beams in the horizontal plane as well as one repumper beam. The 480 nm and 1015 nm lasers can both be focused to 12 μm spot sizes, although only the 480 nm laser is shown at a focus here. As discussed in the text, the CCD is used to align the 480 nm beam, the fluorescence detector records the decay of the trapping beam excitation, and the counters record photons from the decay of the $6P_{3/2}$ state to ground.

of the field switching, this means that for all practical purposes we cannot pulse the magnetic field at a rate faster than about 50 Hz (T_B = 20 ms).

2.2.2 Repumping Laser

After scattering $\sim 10^4$ photons along the F=2, F'=3 cycling transition, the atom will eventually decay to the $5S_{1/2}$, F=1 "dark state" which will not be trapped by the MOT. We put the atom back into the $F = 2$ "bright state" by tuning a laser to the $5S_{1/2}$, F=1, $5P_{3/2}$, F'=2 transition which half of the time decays into $F = 2$, allowing trapping and cooling to continue. For this purpose, we have a separate 780 nm diode laser that acts to repump atoms back into the bright state. The laser is locked via saturated absorption to the crossover peak between the F'=1 and F'=2 transitions, and is then shifted up 80 MHz by an AOM to be resonant with the F=2, F'=2 transition. 1.8 mW are delivered to the atoms, divided into a horizontal and vertical branch by a 50:50 beamsplitter.

2.3 Rydberg Lasers

2.3.1 780 nm Laser

We excite Rydberg atoms from the MOT via two-photon excitation detuned 470 MHz above the $5P_{3/2}$, F'=3 intermediate state. A diagram of the excitation scheme can be seen in Fig. 2.3. The first step of this transition is a 780 nm laser produced by an amplified diode laser system from Toptica. The Toptica laser outputs 300 mW at 780 nm and is frequency stabilized via saturated absorption to the $5S_{1/2}$, $F = 2$ to $5P_{3/2}$, $F' = 3$ transition. Here a frequency dither of less than 1 MHz - induced by a piezo which sinusoidally varies the length of the laser's external cavity - combined with a lock-in amplifier is used to produce the dispersion signal that locks the laser in

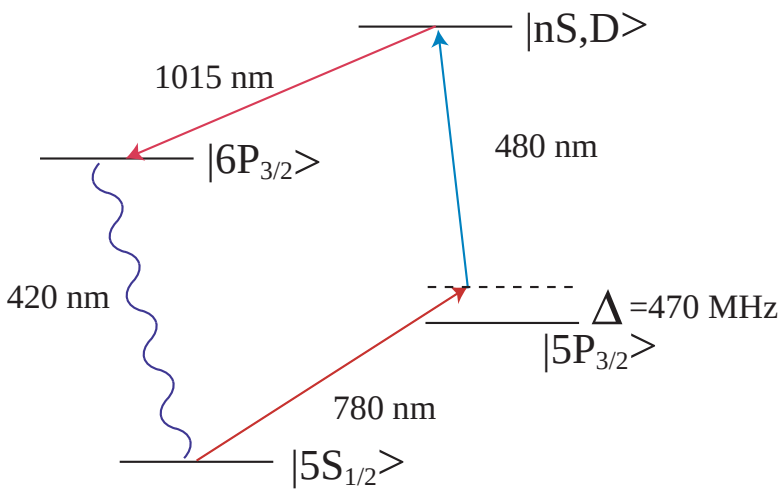

Fig. 2.3: An energy level diagram of the stages of the Rydberg excitation involved in the experiment. We perform a detuned two-photon excitation up to the Rydberg level and a 1015 nm laser-induced stimulated emission process down to the $6P_{3/2}$ state, which may decay via a 420 nm photon back to the ground state.

much the same way that the sidebands produced by the EOM are used to stabilize the Ti:Sapph laser.

The Toptica laser is frequency-shifted up by 470 MHz by a high frequency AOM with a first order efficiency of 17% . The resulting 20 mW of light is delivered to the atoms with an intensity profile that has a $1/e^2$ Gaussian radius (which I will henceforth refer to as the beamwaist) of 4 mm. The beamwaist is larger than the spatial extent of the MOT because of the high Rabi frequency associated with this laser beam. At this width and power, the $5S$-$5P_{3/2}$ Rabi coupling of the Toptica laser to the atoms is 12 MHz. The resonant frequency of the atoms is shifted due to the laser field by the AC Stark Shift, $\Omega^2/4\Delta$ (which is 300 kHz for this setup), where Ω is the Rabi frequency and Δ is the detuning from resonance. Although a more tightly focused beam would

result in a larger Rabi frequency, it would also produce a larger AC Stark shift. More to the point, a beam with a high Rabi frequency and a waist on the order of the length scale of the atomic sample will have an AC Stark shift which varies greatly across the atoms. This will cause the frequency linewidth of the transition to broaden as atoms across the sample will be on resonance for different frequencies of the excitation laser. This is undesirable for a number of reasons that will become more apparent in Chapter 4.

2.3.2 480 nm Laser

A frequency doubled 960 nm amplified diode laser completes the two-photon transition to the Rydberg level. Figure 2.4 shows the major components of the setup, which are as follows: A "master" 960 nm diode in a Littrow-configured external cavity is stabilized by means of an external, confocally spaced Fabry-Perot (FP) cavity with a 1 GHz free spectral range an a finesse of 200. The use of the Fabry-Perot cavity is necessitated by the lack of convenient optical transitions to use for saturated absorption, although recent work by Mohapatra, et al. [Mohapatra *et al.*, 2007] has shown that Electromagnetically-Induced Transparency (EIT) in room-temperature Rydberg atoms could provide a convenient frequency standard. Difficulties arise from the Fabry-Perot in the way of frequency drifts over time. These are due to changes in either the temperature of the cavity or the barometric pressure in the room. The former alters the length of the cavity to cause frequency drifts of a few MHz per mK and must be compensated for by means of a thermo-electric cooler (TEC) and temperature controller which act to stabilize the temperature of the cavity. The latter changes the index of refraction of air in the cavity by a few parts in 10^7, which in turn results in frequency shifts on the order of a few MHz. This problem is minimized by enclosing the FP cavity in a sealed acrylite box with a leak rate of less than 1 torr per hour, as measured by a

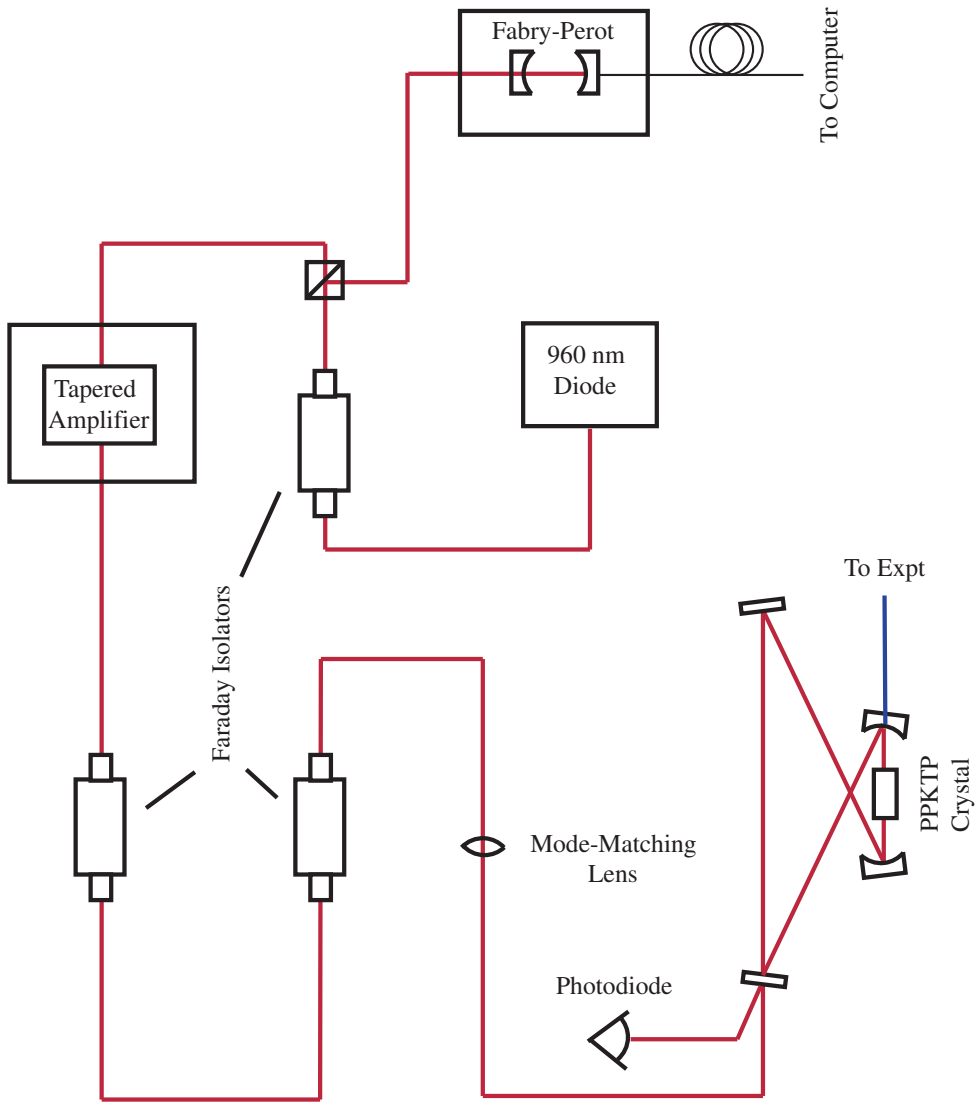

Fig. 2.4: Diagram of the major components of the 480 nm laser. The 960 nm master diode pumps a tapered amplifier and has a portion diverted for locking purposes. The amplifier output passes through two isolators before entering the doubling cavity in a bow-tie configuration.

capacitance manometer in the box. The frequency changes due to barometric pressure at a rate of about 1 MHz per torr at one atmosphere, so temperature fluctuations will tend to dominate the drift rate. I will return to the issue of frequency drifts in Chapter 4. As it stands, we have reduced the cavity drift to a level where the 960 nm frequency drifts on the order of 1 MHz per minute.

When the length of the FP cavity is a half-integer multiple of the wavelength of the incident laser light, the light matching the spatial mode of the Fabry-Perot is transmitted through the cavity and is detected by a photodiode. By monitoring the photodiode current while sweeping the frequency of the laser diode, we obtain a series of peaks whenever the wavelength is resonant with the cavity. Tuning the laser to the desired frequency range, we then stabilize the laser frequency to the side of one of these peaks, which acts as a convenient "error signal" analogous to the type obtained from a dither lock with a lock-in amplifier. A ring piezo attached to the FP cavity controls the cavity length. By altering the applied voltage from a computer, we may then sweep the frequency of the 960 nm diode, and thus of the 480 nm laser, in software.

The stabilized 960 nm laser diode has a short term linewidth of 1 MHz measured by beating the laser against itself with a self-homodyne technique [Ludvigsen *et al.*, 1998]. This laser is focused through a tapered amplifier purchased from Eagleyard Photonics. With 8 mW incident on the amplifier we obtain a 370 mW output. This light is passed through two Faraday Isolators for 70 dB of optical isolation from back-reflection, and then incident upon a resonant cavity in a bow-tie configuration. The resonant cavity frequency doubles the 960 nm light by means of a periodically-poled potassium titanyl-phosphate (PPKTP) crystal purchased from Raicol, all of which are shown in Fig. 2.4. The workings of the frequency doubled system are discussed in greater detail in Chapter 3, for now it is sufficient to note that 15 mW of 480 nm light exits the doubling cavity, around 5 mW of which are delivered to the atoms.

With this system, we are capable of performing excitation to Rydberg states as low as $28D$, up to $70D$ (as well as the nearby S-states, of course), corresponding to a wavelength range of 479.6 to 482.6 nm. The limiting factor in this is the PPKTP crystal temperature which goes from 100 C to 15 C at these extrema (see Chapter 3). At temperatures higher than this range the crystal's anti-reflection coating might be compromised, while at lower temperatures we risk the formation of condensation on the crystal which would scatter the laser light. Except where noted, the components for this laser were assembled in the lab for this experiment. Similar commercial systems are available, however at a much greater price.

2.3.3 1015 nm laser

Now that we are able to place atoms in the Rydberg state, it would be useful to have a way to bring them down into a state with a shorter lifetime and smaller interatomic forces (the reason for this will become more clear in Chapter 4). For this, we use a diode laser system from Sacher Laser with a 1015 nm center wavelength to de-excite the atoms from the Rydberg level down to the $6P_{3/2}$ state. The wavelengths used to accomplish this vary from 1012 to 1026 nm and can access Rydberg states from $70D$ through $27D$. At wavelengths larger than 1026 nm, the laser power drops off significantly, making de-excitation inconvenient for levels lower than $27D$, however this does cover the full range of our Rydberg excitation states. A diagram of this laser setup is shown in Fig. 2.5.

The Sacher laser has a typical power output of 230 mW from the diode which is passed through an optical isolator and divided into three beams. The most powerful is 150 mW which is put into a polarization-preserving single mode fiber and 70 mW of which is subsequently delivered to the experiment. The second stream of 1 mW is diverted by a pick-off slide into a fiber and passed into a wavemeter in order to facilitate

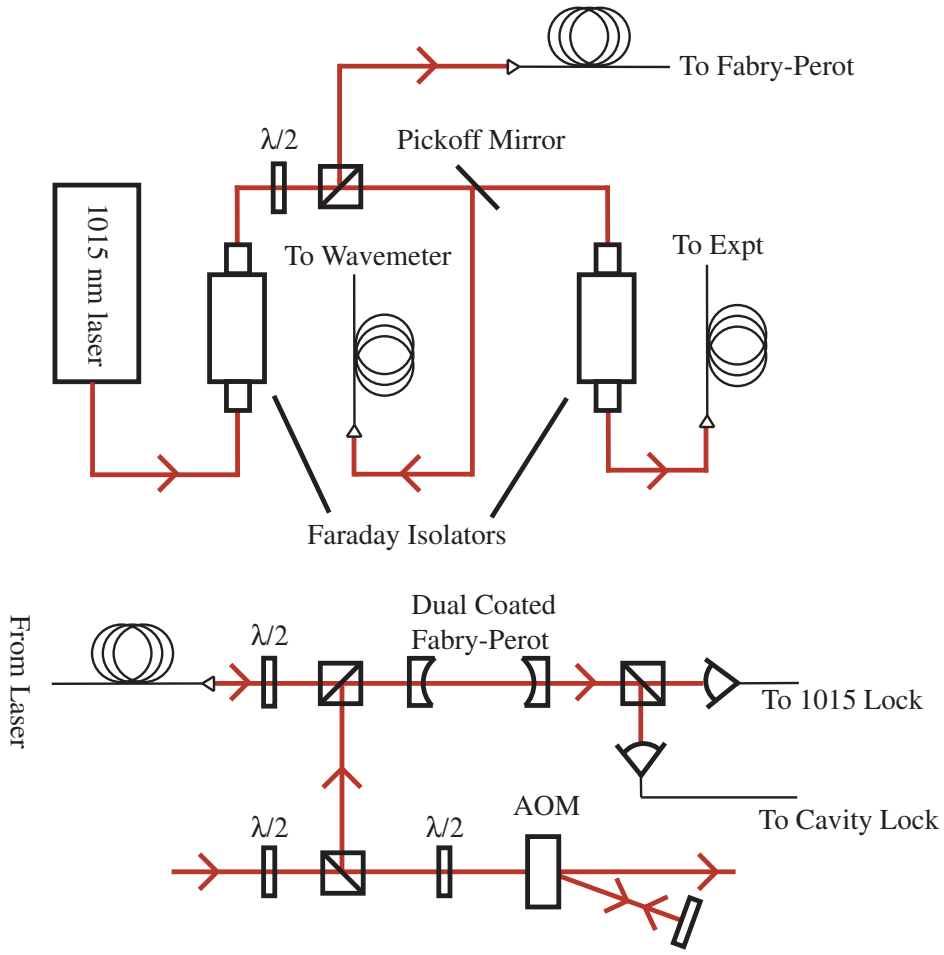

Fig. 2.5: Diagram of the major components of the 1015 nm laser. Light from the diode is diverted into three beams for locking, wavelength measurement, and the experiment. The laser is locked to a Fabry-Perot cavity which is in turn locked to the 780 nm laser.

tuning the laser to the desired wavelength. The final beam of 20 mW is passed through a fiber and into a home-built confocal Fabry-Perot cavity with a 300 MHz free spectral range (FSR) and mirrors that are coated to have over 99% reflectivity at both 780 nm and at a range from 1013 to 1027 nm.

We wish to lock the Sacher laser to the Fabry-Perot cavity in much the same way as we did with the 480 nm laser, but to perform experiments with both of these lasers we must keep at least one of them from drifting while sweeping the other laser. With this motivation, we put the Fabry-Perot cavity in a pressure-sealed aluminum tube with anti-reflection coated flats covering the ends for optical access. To keep the length of the cavity constant, we take the zero order beam from the double pass AOM setup of the trapping laser and direct it into the Fabry-Perot with a polarization orthogonal to the polarization of the Sacher laser (see fig. 2.5), combined on a polarizing beamsplitter cube. Likewise, the polarizing beamsplitter cube on the output of the cavity separates the beams once again and directs each onto a photodiode.

With the frequency-locked 780 nm beam passing through the FP, the length of the cavity is swept by means of a ring piezo attached to one of the mirrors, producing a signal identical to the one from ramping the 960 nm frequency in the 1 GHz FSR cavity. We then stabilize the resonance frequency of the cavity by dither locking the cavity to the 780 nm laser. Now that the cavity length no longer drifts, we may dither the frequency of the Sacher laser and use a lock-in amplifier to produce an error signal and lock the laser to the cavity. Unfortunately, the Sacher laser is not tunable if locked in this way. To correct this, we wish to be able to adjust the frequency of the 780 nm beam incident on the Fabry-Perot cavity over one free spectral range, in this case 300 MHz. The 100 mW, 780 nm beam is first diverted through a double-passed high-frequency AOM which shifts the frequency of the light between 340 to 490 MHz on each pass. This range is sufficient to cover the free spectral range of the cavity while still

producing a high enough first order conversion efficiency to deliver 1 mW of the light to the cavity for the lock. The frequency shift of the AOM is dynamically programmed by the same computer that controls the 480 nm laser so that either the 480 or 1015 nm laser frequency can be swept to perform spectroscopy on the Rydberg state.

2.4 Detection Devices

Now that we have a functioning MOT and a set of lasers to perform excitation and de-excitation through a Rydberg state of our choosing, we require methods for determining how many atoms are in the MOT, how many are in the Rydberg state, and how many atoms are de-excited from the Rydberg down to the $6P$ state. Detecting the number of atoms in the MOT is the most straight-forward: we may monitor the fluorescence of the $5P_{3/2}, F' = 3$ state as it decays down to the ground state. This 780 nm light is radiated nearly isotropically, a small portion of which is collected with a lens and directed onto a photodiode covered by a 780 nm bandpass filter to eliminate background light. The intensity of the light collected on the photodiode is proportional to the number of atoms in the MOT. We have previously determined the number of atoms in the MOT in terms of experimental parameters as [Newell, 2003]:

$$N_{MOT} = \frac{V}{A} \times \frac{\eta\tau}{(hc/\lambda)p_{ee}\Theta} \times \left[\frac{1}{0.56 \times 0.595 \times 0.5}\right]. \tag{2.1}$$

Here, V is the voltage measured by the photodiode from the fluorescence signal of the MOT (a full MOT is 0.6 V), A = 9.9×10^6 is the gain of the current-to-voltage converter, $\eta = 2$ W/A is the photodiode detection efficiency at a 780 nm wavelength, $\tau = 27$ ns is the lifetime of the $5P$ state, $p_{ee} = 0.122$ is the fraction of the MOT atoms in the excited state, $\Theta = 0.006$ is the fractional solid angle subtended by the photodiode, and the quantity in the [ ] brackets takes transmission losses from three filters into

account. This gives a value of 1.04×10^8 atoms in the MOT for these parameters. As we will see in Chapter 4, we may use the change in the MOT fluorescence to measure the loss rate from the MOT induced by the Rydberg excitation lasers and thus obtain a measure of the number of atoms in the Rydberg state.

The decay of the $6P_{3/2}$ state also gives us a source of information on the dynamics of the Rydberg state and the de-excitation induced by the 1015 nm laser (see Chapter 4). For the dipole blockade and single-photon source experiments that we would like to perform, it is necessary for us to use photon counting modules in conjunction with an IDE card which allows us to record the arrival times of the incident photons to the nearest 100 ns time interval. For this purpose we purchased two H7360-01 photon counting modules from Hamamatsu and a multi-channel scalar card from FAST ComTec. The modules were chosen to have relatively low dark count rates (30 counts per second and 110 counts per second for the two counters we use) and a maximum count rate of 6×10^6 counts per second before saturation effects alter the signal. The modules are designed to send out a 9 ns wide TTL pulse when a photon is detected, with a 9 ns "dead-time" immediately following the pulse in which no pulses are transmitted.

We measured the quantum efficiencies of the photon counters at 420 nm to be 5.5% and 5.3% for counter 1 and counter 2, respectively, as seen in Fig. 2.2. In order to do this, we obtained a source of 420 nm photons from a white light which we passed through a monochrometer calibrated and aligned to transmit 420 nm light. We covered the output slit of the monochrometer with a 5 nm spectral width 420 nm bandpass filter to remove any background light and then recorded the current produced from the incident 420 nm light on a photodiode with a known current per unit power at that wavelength. This allowed us to calculate the flux of 420 nm photons in the beam and by comparing this number to the count rate of the photon counters observing the same light we obtained the detector quantum efficiency.

The counting modules exhibit dark-count-induced afterpulsing. When a dark count is observed on one of the counting modules there is an increased chance of observing a second dark count on that module over the next 10 μs. Figure 2.6(a) shows this effect on counter 2; only dark counts are recorded in the figure. Obviously, this would be undesirable in any photon correlation measurement. So when we wish to measure, for instance, the second order correlation function $g^{(2)}$ [Loudon, 1983], we use a 50:50 beamsplitter cube to send equal 420 nm beams to both photon counters, in a setup similar to a Hanbury Brown and Twiss experiment [Hanbury Brown and Twiss, 1956]. We then trigger a sweep with the first counter while counting subsequent pulses with the second counter. For small count rates ($\sim$1 count per sweep), this removes the effects of afterpulsing from the data. A dark count measurement without afterpulsing done in this manner is seen in Fig. 2.6(b). Both graphs were recorded over five minutes; we would expect 1.8 total photons from dark counts during this period if dark counts were randomly occurring during this period. Thus, not only is the concentration of afterpulsing counts in the first 1 μs a concern, but in fact practically all of the counts seen in Fig. 2.6(a) are afterpulsing counts that will obscure the signal of a $g^{(2)}$ measurement.

It is common in Rydberg atom experiments to employ an ion counter such as a micro-channel plate (MCP) detector to ionize Rydberg atoms with an ionizing pulse from an electric field which increases in strength over time so that one may determine the populations of Rydberg atoms at different principal quantum numbers. Examples of this can be seen in the experiments here [Walz-Flannigan *et al.*, 2004] and [Singer *et al.*, 2005]. We have chosen not to implement this type of detector primarily because this would require blocking a port from optical access in order to pass the requisite electrical connections into the vacuum chamber. All ports are currently in use in our vacuum chamber, however we do have a new vacuum chamber with additional ports that could accommodate an MCP that may be used in the future. Instead, we are

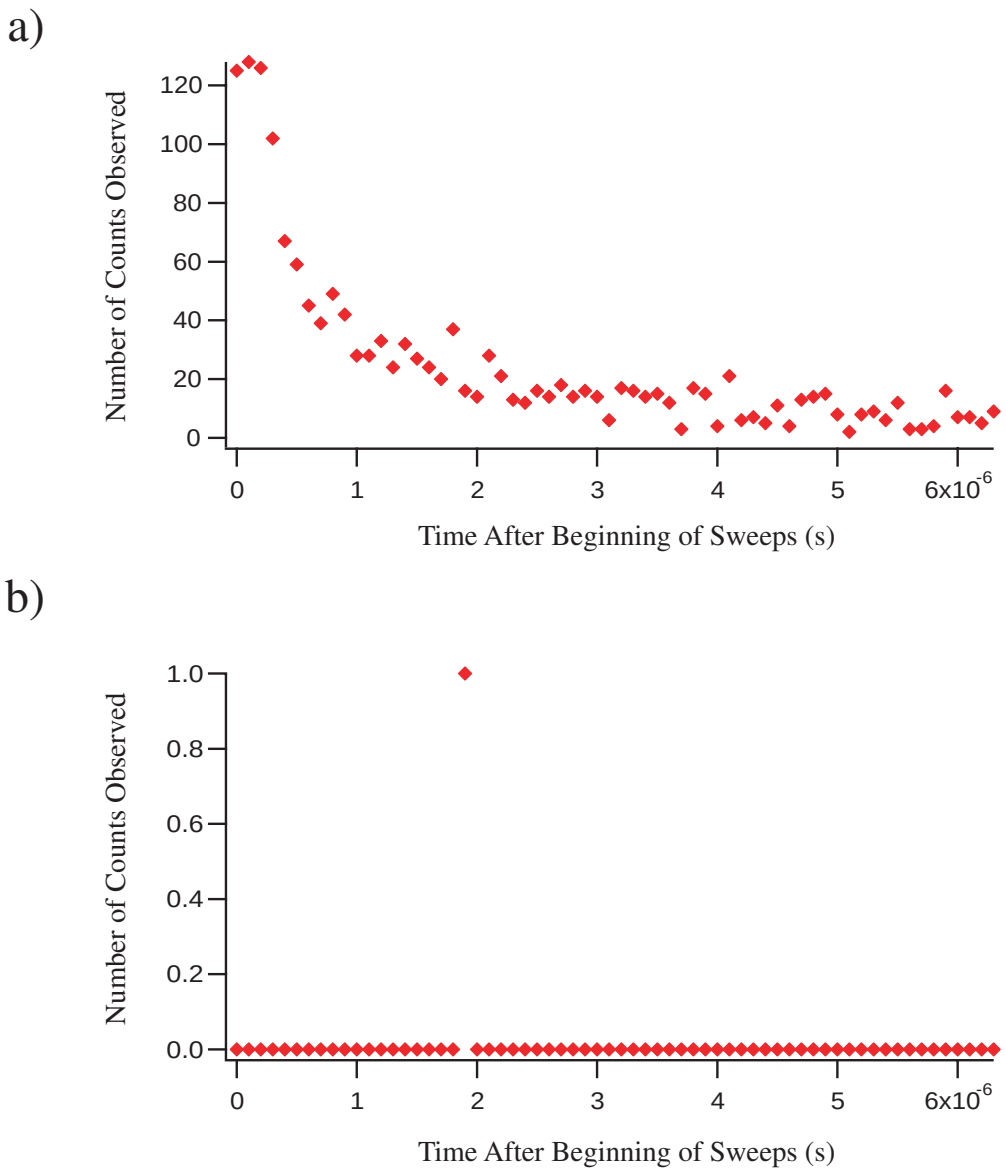

Fig. 2.6: Data showing the effects of afterpulsing on the counters when counting with (a) one counter and (b) two counters. This data was taken over the course of 5 minutes and resulted in 2408 triggered sweeps with 1830 counts in (a) and 1 count in (b). If counts occurred randomly, we would expect 1.8 total counts in each graph.

using the 1015 nm laser as a Rydberg state probe, which will be discussed in Chapter 5.

We also have a CCD camera from Hamamatsu with a 8.6 by 6.6 mm area and a 6.45 μm pixel size. The fluorescence from the MOT can be imaged onto the CCD chip, or by transmitting a resonant laser pulse through the cloud of atoms we can perform absorption imaging on the MOT. This technique was used extensively in past experiments but very seldomly in our Rydberg atom experiments. Since the camera is along the path of the 480 nm laser, we image the spot of the 480 nm beam on the MOT as a measurement of the beamwaist and a check of the alignment.

2.5 Optics Train

The experimental setup shown in Fig. 2.2 shows the optics train focusing each of the excitation lasers into the vacuum chamber as well as one of the alignments used for the counters. In particular, this alignment will be useful for the four-wave mixing experiments described in Chapter 7. The optics train to counter 1 is worth mentioning since it impacts several detection devices. A pair of bi-convex lenses, with 150 mm and 750 mm focal lengths, collimate the light emitted from the MOT and focus it at the CCD camera 750 mm away from the second lens. A reflective low pass filter is used to reflect the 420 nm photons from the decay of the $6P_{3/2}$ state towards counter 1 while transmitting the 780 nm fluorescence photons to the camera and photodiode. An iris is in the path of the 420 nm photons, as we will see in Chapter 7 this iris can be stopped down to reduce the solid angle subtended by the detector while still letting phase-matched photons from the four-wave mixing process through.

There is a 50:50 beamsplitter cube in front of counter 1 which allows us to place counter 2 in the path of the other half of this beam of photons to eliminate afterpulsing

when taking photon correlation measurements. Two 420 nm bandpass filters are in this train: one before the beamsplitter cube and another covering the aperture of the each of the counters.

After exiting the fiber, the 480 nm laser beam curvature is reduced by (but not collimated by) the objective lens at the output of the fiber. The beam is then collimated at a waist of about 9 mm by a 400 mm focal length lens with a 50 mm diameter. A second 400 mm lens focuses the 480 beam to a focused 12 μm waist at the atoms. We measure the waist size by imaging the spot with an objective lens onto a CCD camera. Also, we may adjust the location of the focus by moving the focusing 400 mm lens along the axis of propagation and observing the counts produced when the excitation lasers are on resonance. The focus will be at a local minimum for cascade counts (see Chapter 4), which we can determine to within $\pm$ 0.5 mm.

The 1015 nm laser is focused in a manner similar to the 480 nm laser, with a pair of 400 mm lenses that collimate and then focus the 1015 beam to a 12 μm spot at the atoms. As the beams intersect at a 45° angle, the intersection volume is 17 μm long in its longest dimension, provided that both beams are at their foci. Alternatively, we can move the final 400 mm lenses so that the 480 nm and 1015 nm beams focus before the atoms and then diverge to the size of the MOT cloud at the atoms, as seen in Fig. 2.7. This allows us to perform experiments at both high and low Rabi frequencies (or as I will refer to them, focused and unfocused beams) as we will see in Chapter 4.

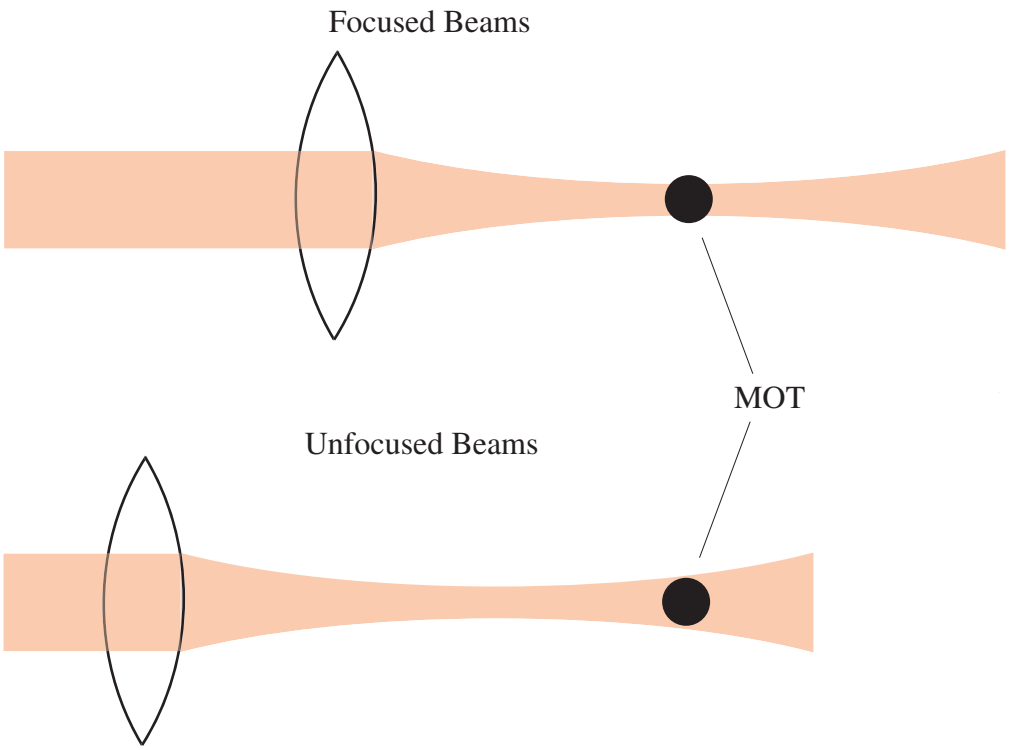

Fig. 2.7: The figure shows the position of the f = 400 mm focusing lens for both the focused beam and unfocused beam setups. For the unfocused setup, the beam is diverging at the atoms and covers the entire MOT.

3. FREQUENCY DOUBLING

3.1 Introduction

The design and construction of a frequency-doubled 480 nm laser is an involved process. This chapter will explain the procedure, beginning with a brief explanation of the physical origin of frequency doubling in nonlinear materials. Here I introduce the equations required to calculate the amount of frequency-doubled light that is produced when plane waves at the pump frequency pass through a nonlinear crystal. This will result in the phase-matching condition for the crystal, which must be met to achieve optimum conversion efficiency from fundamental to harmonic in the crystal. Next I discuss some corrections to these equations, beginning with quasi-phase-matching and periodic poling, which was used in the construction of our crystal in order to utilize the strong d_{33} nonlinear coefficient of Potassium Titanyl-Phosphate (KTP).

Phase-matching in the crystal is accomplished by matching the index of refraction at both pump and harmonic frequencies, and this in turn requires changing the crystal temperature. Thus I present the Sellmeier equations for KTP, which model the dependence of the refractive index on temperature and wavelength. I then calculate the required phase-matching temperature for the wavelengths used in the experiment and verify that this temperature is achievable in our setup. The final correction is the strong focusing of the pump beam that is required to maximize the intensity of the pump over the length of the crystal. This requires the use of Boyd-Kleinman theory to

calculate the optimum waist to maximize the conversion efficiency.

I also discuss considerations required when designing a resonant cavity for the crystal. In particular, the choice of the pump transmission percentage of the input mirror into the cavity is vital for maximizing the circulating intensity in the cavity. I calculate the optimum input coupler transmission percentage as well as the placement of the mirrors in the bow-tie cavity using ABCD matrices. I then discuss the proper alignment procedure for the cavity. Using a 29 μm focused 960 nm spot in the center of the crystal and a cavity of total length 37 cm, 12 mW of 480 nm light are produced for a conversion efficiency of 5.4%. This number is much lower than expected, thus I conclude the chapter by discussing possible causes and improvements.

3.2 Theory

The existence of frequency doubling in a crystal is a property arising from the nonlinearity of the response of the crystal to external fields. This, in turn, is due to asymmetries in the crystal lattice structure which make the crystal birefringent, that is, have different indices of refraction along its three axes. To look at the potential energy of a valence electron in one dimension of an asymmetric crystal, one finds terms of odd powers of the electron displacement that do not exist for symmetric crystals of the form:

$$V(x) = Ax^2 + Bx^3 + ..., \tag{3.1}$$

where A and B are coefficients whose values are determined by physical properties of the crystal. The fact that such crystals do not possess the normal symmetry of the electric field potential where V(-x) = V(x) means that the restoring force on the electron ($-\partial V/\partial x$) will contain both even and odd powers of the displacement x. Now

let us consider an oscillating electric field such as that produced by an optical frequency laser propagating through the crystal medium. When the electric field from the laser drives a negative displacement of the electron, the even and odd powers of x contained in the restoring force will have opposite sign, which will make this restoring force smaller than the force for a positive displacement. The induced polarization field in the crystal is directly related to the displacement of valence electrons in the crystal lattice, and the fourier transform of the polarization field will thus have frequency components at both the fundamental and second harmonic frequencies of the driving field. This simplistic discussion is meant to give some insight into the physics behind the generation of frequency doubled light in nonlinear materials. Further details of the process are largely out of the scope of this text but can be found in a standard textbook on nonlinear optics such as [Yariv, 1971], [Sutherland, 2003], or [Dmitriev, 1997].

3.2.1 Wave Equations

What does concern us here is calculating the amount of frequency doubled light produced by a non-linear crystal given the properties of the crystal and the intensity of the pump beam at the fundamental frequency. For this, it is necessary to look at the propagation of electromagnetic waves in the nonlinear crystal. Such a treatment can be found in a number of texts on nonlinear optics such as [Yariv, 1971]. For our purposes it is sufficient to begin with the power at the second harmonic frequency produced by a plane wave at the pump frequency passing through an optical crystal of length l. If $P_{2\omega}$ is the power at the harmonic frequency, P_{ω} the power at the fundamental frequency ω, d_{NL} the nonlinear coefficient of the crystal, w the beamwaist, and n the index of refraction at the pump frequency, the harmonic power produced is given by,

$$P_{2\omega} = P_{\omega}^2 \frac{2\omega^2 d_{NL}^2 l^2}{\pi \epsilon_0 c^3 w^2 n^3} sinc^2 \left(\frac{\Delta k l}{2} \right), \tag{3.2}$$

where $\Delta k \equiv k_{(2\omega)} - 2k_{(\omega)}$ and $sinc(x) \equiv \sin(x)/x$. From Eq. 3.2 we see that the power of the harmonic wave is proportional to the square of the power in the fundamental wave. This equation is often written in terms of a conversion efficiency E_{NL} as,

$$\frac{P_{2\omega}}{P_{\omega}} = E_{NL} P_{\omega}, \tag{3.3}$$

where E_{NL} contains all the other terms of Eq. 3.2. It is this equation that will allow us to calculate the amount of blue light that should be produced on each pass and thus aide in the design of our resonant cavity.

The sinc(x) function is maximized at x = 0. This means that we will maximize blue light production when $\Delta k = 0$, which is known as the phase-matching condition. We can see why this is by noting that $\Delta k = 0$ requires that $k_{2\omega} = 2k_{\omega}$. When put in terms of the refractive index this becomes $n_{2\omega} = n_{\omega}$, and so the phase-matching condition is in fact an index-matching condition. If the refractive indices differ for the fundamental and harmonic frequencies then the waves will propagate at different group velocities and become out of phase with one another, hence the label "phase-matching".

3.2.2 Quasi Phase Matching

The Potassium Titanyl Phosphate crystal (KTP, or $KTiOPO_4$) used in this experiment is utilized in a type II non-critical phase matching setup [Sutherland, 2003]. Other crystals commonly used for frequency doubling in this wavelength range include Lithium Niobate (LN, or $LiNbO_3$). An ordinary KTP crystal could not be used for frequency doubling in this manner, however, because dispersion effects prevent the efficient buildup of the second harmonic beam. Instead we must use a quasi phase-

matching scheme where our phase-matching condition is deliberately set to a non-zero value. If the phase-matching condition is non-zero, the harmonic wave will drift in and out of phase with the fundamental on a length scale known as the coherence length l_c,

$$l_c = \frac{2\pi}{\Delta k} = \frac{\lambda_0}{2(n_{2\omega} - n_\omega)}. \tag{3.4}$$

When the phase difference between the two waves becomes greater than $\pi/2$, the harmonic wave begins to transfer power back into the fundamental [Fejer *et al.*, 1992]. This can also be thought of in terms of the stored energy in the crystal doing positive work on the pump beam whenever the phase difference between the pump field and the induced polarization field in the crystal is between $\pi/2$ to $-\pi/2$. To prevent this from happening, the crystal is modified so as to flip the sign of the phase difference once it reaches $\pi/2$. The most common method of doing this is to have many crystal slabs each of one coherence length l_c stacked end to end. Each slab is rotated 180° about the propagation axis with respect to the slab preceding it, which due to the asymmetry of the crystal lattice acts to flip the sign of the components of the susceptibility tensor. This in turn shifts the phase of the polarization wave by π relative to the pump field. Thus power is continuously transferred from the fundamental to the harmonic beam. This is known as first order quasi phase matching (QPM) since there is always a non-zero phase mismatch present in the crystal. The order of the QPM is given by the number of coherence lengths in each slab length, thus third order QPM would have "slabs" of three coherence lengths. The phase-matching condition must then be modified by requiring that

$$\Delta k = k_{2\omega} - 2k_\omega - \frac{\pi m}{\Lambda}, \tag{3.5}$$

where Λ is the length of the poling grating (that is, the length of each "slab") and m is

the mode order of the grating. We use the first order mode for the PPKTP crystal for this experiment. The poling reduces the effective nonlinear coefficient of the crystal by a factor

$$d_{eff} = \frac{2d_{33}}{\pi}, \tag{3.6}$$

where the d_{33} coefficient is the scalar component of the nonlinear coefficient used in this experiment. For KTP, $d_{33} = 16.2$ pm/V which makes the effective coefficient $d_{eff} = 10.3$ pm/V [Sutherland, 2003].

3.2.3 Sellmeier Equations

Next we must calculate how the phase matching varies with temperature. In general for nonlinear crystals such as KTP, the index of refraction varies with temperature as well as wavelength, and in fact the rate of change of the index of refraction with temperature is itself wavelength dependent. To give an idea of the magnitude of the differences in the refractive index, the index for KTP at room temperature is 1.83 at 960 nm and is 1.91 at 480 nm. This frequency and temperature dependence is parametrized for nonlinear crystals by the Sellmeier equations. The one-pole Sellmeier equation describes the variation of the refractive index with wavelength as follows:

$$n_z^2 = a_z + \frac{b_z}{1 - c_z/\lambda^2} - d_z\lambda^2. \tag{3.7}$$

Here, we are looking at the component of the refractive index along the direction of propagation of the field (which we will refer to as the z-axis) in terms of four parameters that are dependent on the particular type of crystal being used. The numbers used for these KTP calculations are taken from measurements performed by Fan *et al.*, [Fan *et al.*, 1987] and are $a_z = 2.25411, b_z = 1.06543, c_z = 0.05486, d_z = 0.02140$.

Of course, the refractive index also changes with temperature, which is how our phase-matching requirement is fulfilled. The temperature derivative of the refractive index dn_z/dT is material specific, for KTP this has been measured by Kato [Kato, 1992] to be,

$$\frac{dn_z}{dT} = 10^{-5}\left[2.115 + \frac{0.3896}{\lambda^3} - \frac{1.3332}{\lambda^2} + \frac{2.2762}{\lambda}\right]. \tag{3.8}$$

By combining Eq. 3.7 with Eq. 3.8 we get an equation which fully describes the temperature and frequency dependence of the refractive index:

$$n_z'(\lambda, T) = \sqrt{n_z^2(\lambda)} + \Delta T \frac{dn_z}{dT}(\lambda), \tag{3.9}$$

where n_z^2 is the result from Eq. 3.7, $\frac{dn_z}{dT}$ is taken from Eq. 3.8 and $\Delta T = T - 293.15$ where T is the temperature of the crystal in Kelvin.

We can now use the refractive index calculations to calculate the Δk phase mismatch from Eq. 3.5 and thus map out the phase mismatch as a function of wavelength. Figure 3.1 shows the dependence of the phase mismatch on wavelength for three different temperature curves. Experimentally, it will be more convenient to sweep the crystal temperature and look for the highest blue power output rather than try to calculate the appropriate phase-matching temperature, however this figure is important in that it demonstrates that the phase-matching condition can be met for crystal temperatures ($10°\text{C} < \text{T} < 150°\text{C}$) used in the laboratory.

3.2.4 Boyd-Kleinman Focusing

The result in Eq. 3.2 applies for plane waves propagating through a crystal. However, it is clear from the equation that the power in the frequency doubled beam will depend upon the square of the intensity of the fundamental beam. Thus, it is desirable to

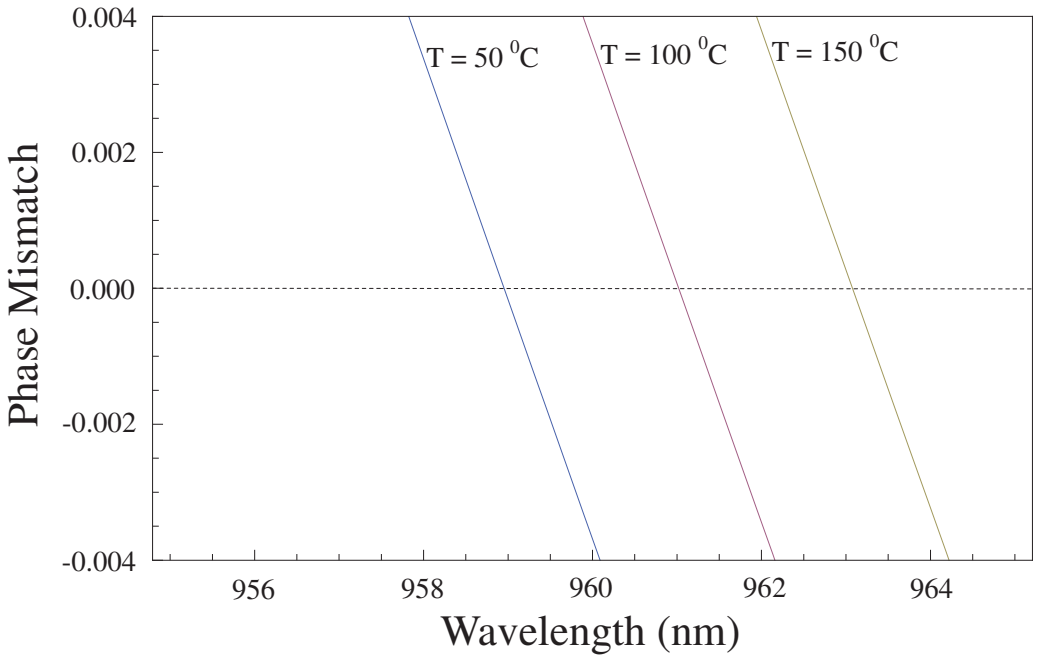

Fig. 3.1: Dependence of the phase-matching condition on wavelength for three temperatures. For Rydberg atom excitation, phase matching for wavelengths between 959.5 and 964 nm is required. The figure shows that this is possible for reasonable crystal temperatures.

make the intensity of the fundamental as large as possible in the crystal. On the other hand, the tighter the focus that is achieved, the faster that beam will diverge away from the focus. It should then be clear that a balance must be struck which maximizes the intensity of the fundamental across the entire length of the crystal. In a paper by Boyd and Kleinman [Boyd and Kleinman, 1968], they derived conditions for maximum frequency conversion in non-linear crystals. The Boyd-Kleinman analysis treats the case of a tightly focused beam where the photons have nonzero angles with respect to the propagation axis away from the focus. As a result, the $\mathrm{sinc}^2(\Delta kl/2)$ parameter is replaced by the Boyd-Kleinman integral $h(z)$, where

$$h(z) = \int_0^z dz' \frac{e^{i\Delta k z'}}{1 + i\frac{z'}{z_R}}. \tag{3.10}$$

In this equation, z_R is the Rayleigh range of the pump beam given by

$$z_R = \frac{\pi n_1 w^2}{\lambda}, \tag{3.11}$$

where n_1 is the index at the wavelength of the pump beam, and w is the beamwaist. In the plane wave approximation, $z_R \to \infty$ and Eq. 3.10 reduces to a sinc^2 function again. By integrating across the length of the crystal, we may determine what waist is needed at the center of the crystal in order to obtain the most efficient blue light production over the length of the crystal. From numerical analysis, we determine that the integral is maximized when $z_R = l/5.68$ where l is the crystal length of 3 cm, which implies that the conversion efficiency will be optimized when $w = 29\mu m$ at the center of the crystal. When evaluated for these parameters, the Boyd-Kleinman integral from Eq. 3.10 will have the value,

$$|\tilde{h}|^2 = \frac{1.068 z_R}{l}. \tag{3.12}$$

We are now equipped to calculate the single pass blue conversion efficiency in our

PPKTP crystal. As noted earlier, the effective nonlinear coefficient d_{eff} is 10.3 pm/V. The index of refraction is 1.87, and the power input into the cavity is 220 mW with a waist of 29 μm at the center of the 3 cm length crystal. Thus E_{NL} from Eq. 3.3 is 0.067 W^{-1}, and on a single pass we should produce 3.2 mW of 480 nm light, for a conversion efficiency $E_{NL}P_{\omega}$ of 1.5%. Experimentally, we measure 170 μW of 480 nm light produced in a single pass by a 960 nm input power of 142 mW for a measured E_{NL} of 0.0084 W^{-1}. Clearly to produce several mW of blue, a resonant cavity will be required. We must now discuss the design of a resonant cavity that will produce the Boyd-Kleinman waist in the center of the crystal so that we may utilize the intensity build up in a resonant cavity to increase the intensity of the pump light in the crystal and thus more efficiently produce the frequency-doubled blue light.

3.3 Resonant-Cavity Design

For our resonant cavity, we use a unidirectional bow-tie cavity to produce the desired Boyd-Kleinman waist in the center of the PPKTP crystal. This has the advantage that all of the blue light is coupled out of the cavity immediately after production and does not have to propagate through additional optical elements while losing power as it would in a bi-directional cavity. The calculations are made by using ABCD matrices to calculate the transfer of the waist through the optical elements of the system.

ABCD matrices with gaussian beams provide a convenient method for determining the waist and curvature of a beam after propagation through complicated optical systems. Assuming a gaussian beam with initial waist w_1 and an initial radius of curvature R_1, we may fully describe the gaussian beam with the parameter $\tilde{q}_1$ where,

$$\frac{1}{\tilde{q}_1} = \frac{1}{R_1} - \imath\frac{1}{z_1}, \tag{3.13}$$

where z_1 is the Rayleigh range of the beam at this waist. The coefficients of the matrix then describe the beam with parameter $\tilde{q}_2$ after propagating through some system of optics as follows:

$$\frac{\tilde{q}_2}{n_2} = \frac{A(\tilde{q}_1/n_1) + B}{C(\tilde{q}_1/n_1) + D}. \tag{3.14}$$

The matrix aspect of ABCD matrices comes about because the $\tilde{q}$ parameter can be seen as a vector with real and imaginary components and A, B, C, and D the components of the transfer matrix that transforms vector $\tilde{q}_1$ to $\tilde{q}_2$.

A diagram showing the propagation of laser light through the optical cavity is shown in Fig. 3.2. The figure shows that a mode-matching lens is used to set up a resonant mode inside the cavity. This entails forming a waist w_1 at the center of the two flat mirrors in the cavity. The first curved mirror is positioned so as to form a smaller waist w_2 at the center of the crystal, and the second curved mirror must then focus the beam such that it reaches the same waist w_1 at the center of the flat mirrors once again. For optimum conversion efficiency, the curved mirrors should be symmetric about the crystal so as to set up a real waist in the center of the crystal. Both curved mirrors for this setup have a 5 cm radius of curvature and the crystal is 3 cm in length.

For the cavity to support resonant modes, the $\tilde{q}$ parameter must be invariant upon a complete pass through the cavity. Values of the ABCD matrix that satisfy this correspond to $\tilde{q}$ parameters called self-consistent $\tilde{q}$ values or eigen-$\tilde{q}$ modes [Siegman, 1986]. From these we get the condition necessary for a resonant cavity mode, $(\mathrm{A+D})/2 \leq 1$, and can now calculate the ABCD parameters for this bow-tie cavity.

The cavity calculations will be very sensitive to the position of the curved mirrors. It is then convenient to define two lengths, a total cavity length L and the distance between the curved mirrors L_2 as shown in Fig. 3.2. If the crystal length is L_c, the

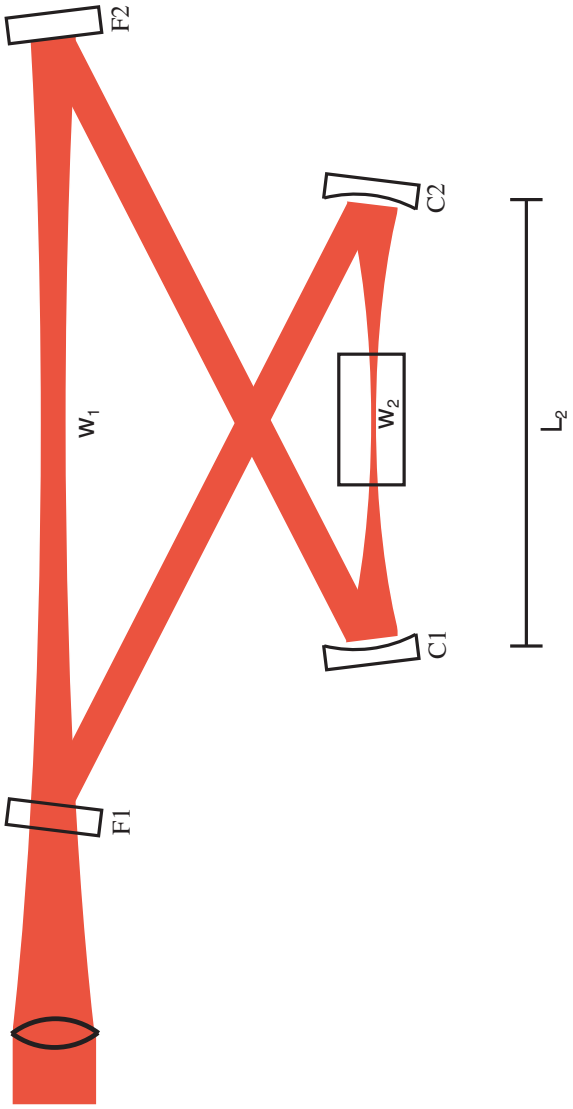

Fig. 3.2: The principal optical components of the frequency doubling cavity are shown. A mode-matching lens focuses the 960 nm beam to a 220 μm focus at w_1. Then the curved mirror C1 focuses the beam to a waist of 29 μm at the center of the crystal at w_2.

index of refraction of the crystal n_c, and the radius of curvature of the curved mirrors R then the round-trip ABCD matrix is related to these parameters as follows:

$$A = D = \frac{2(L - L_2)(L_2 - L_c') - 2R(L - L_c') + R^2}{R^2} \tag{3.15}$$

$$B = \frac{[L_2 - R - L_c'][(L - L_2)(L_2 - L_c') - R(L - L_c')]}{R^2} \tag{3.16}$$

$$C = \frac{4(L - R - L_2)}{n_c R^2} \tag{3.17}$$

where $L_c' = L_c \frac{n_c - 1}{n_c}$. We can now evaluate the stability parameter and determine the range of L_2's that will work for a given total length L. In addition, we may evaluate the $\tilde{q}$ parameter at the center of the crystal and determine what size waist will be produced there. Typically this is done numerically with a symbolic manipulation program such as Mathematica. Figure 3.3 shows such a measurement done for a total cavity length of 37 cm and a crystal refractive index of 1.87. Figure 3.3 shows that the range of accessible waists is a parabolic function of the curved mirror spacing L_2. Recall that the Boyd-Kleinman optimum waist we calculated was 29 μm, which is what the waist is at the top of the parabola in the figure, corresponding to a curved mirror spacing of $L_2 = 6.8$ cm. Waists at the inflection point of the parabola are the most stable to small changes in L_2 and are thus desirable for the experiment.

All that remains is to calculate the larger waist w_1 and calculate what mode-matching optics will be required to create that waist between the flat mirrors. This is once again done numerically and determined to be 220 μm for our cavity parameters. A note of caution, the effective radius of curvature of the curved mirrors is reduced in the horizontal plane by roughly the cosine of the angle that the beam makes with the surface normal at the center of the mirror. Thus the bow-tie cavity should be as flat as possible to avoid any beam asymmetry. Some of the asymmetry can be accounted for by adjusting the mode-matching optics such that the waist at w_1 is slightly larger

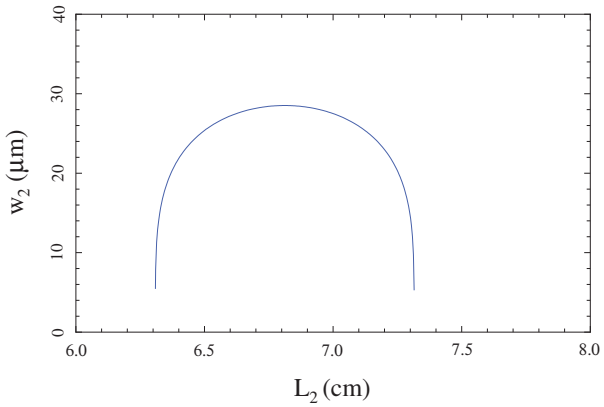

Fig. 3.3: Beamwaist of the 960 nm pump at the center of the doubling crystal as a function of curved mirror spacing L_2. The plot is evaluated for a total cavity length of 37 cm. The figure indicates that the curved mirrors should be separated by 6.8 cm to ensure the proper Boyd-Kleinman waist of 29 μm at the crystal center.

in the horizontal plane. Given the input waist of the 960 nm beam, we may calculate what lens is needed to match the mode of the ring cavity. If the input beam has a large, symmetric, gaussian waist of w_0, then the lens needed to create a waist w_1 at a focal length f away from the lens is,

$$f = \frac{\pi w_0 w_1}{\lambda}. \tag{3.18}$$

Now that we have a resonant cavity design to work with, we must still know what coatings to order for the mirrors. This is trivial for most mirrors as we want the mirrors to be highly reflective (R $>$ 99.9%) at 960 nm and to transmit all light at 480 nm. However, the input coupler is different in that its value must be chosen to optimize the circulating intensity of the cavity. As it happens, the physics of resonant optical cavities has a close analog in the physics of electronic circuits. Just as the impedance of a voltage signal input must be matched to that of the circuit's load to avoid reflections

which waste power, so too must the "impedance" of the optical cavity be matched by the input coupler so that all of the light incident on the input coupler is coupled into the cavity when the piezo controlling the cavity length sets the cavity to be resonant with the input wavelength. This is called the impedance-matching condition, and is met when the input coupler (or here, the first flat mirror in Fig. 3.2) transmits as much light as the cavity loses to absorption, scattering, and blue conversion in a single pass. This is made more complicated by the fact that the circulating intensity of 960 nm light in the cavity will be high enough that a few percent of it will be converted to 480 nm on each pass.

Polzik and Kimble [Polzik and Kimble, 1991] analyzed second harmonic generation using $KNbO_3$ in an external cavity and noted that the input coupler transmission percentage T_1 is related to the doubling efficiency $\epsilon \equiv P_2/P_1$ by

$$\sqrt{\epsilon} = \frac{4T_1\sqrt{E_{NL}P_1}}{\left[2-\sqrt{1-T_1}(2-L-\sqrt{\epsilon E_{NL}P_1})\right]^2}, \tag{3.19}$$

where L is the round-trip loss rate and E_{NL} is the single-pass efficiency from Eq. 3.3. The optimum value for T_1 in an impedance-matched cavity is then,

$$T_1^0 = \frac{L}{2} + \sqrt{\frac{L^2}{4} + E_{NL}P_1}. \tag{3.20}$$

For our optical cavity, the round trip loss rate in the absence of blue light production was measured to be 3%. At the time the cavity was designed, we did not anticipate more than around 50 mW for P_1 so the input coupler was chosen to be 5% based on this even though for 220 mW input as we have now it would be 8%. The efficiency calculated for the 5% input coupler from Eq. 3.19, with $P_1 = 220$ mW is 74%. If we were using an 8% input coupler with these same parameters, the calculated conversion efficiency would be 83%. However, as we will see, this is not currently the limiting

factor in the production of 480 nm light.

3.4 Alignment Procedure

Now that we have made the relevant calculations, it may be useful to provide a step-by-step guide to setting up and aligning the doubling cavity from scratch. Before beginning the alignment several things should have already been done. The input waist w_0 should have already been measured and the appropriate mode-matching lens put in place to focus the pump beam to the large cavity waist w_1 of 220 μm as calculated before. There should be two mirrors set up before the first flat mirror of the cavity to act as input couplers into the cavity. These mirrors should be located after the mode-matching lens to prevent steering through the lens. The mirrors should all be at the same height on their holders and there should be two aluminum alignment jigs nearby with holes drilled at the appropriate beam height. The larger hole is around 2 mm and is used for coarse adjustment while the smaller hole is about 400 μm and is used to fine tune the beam alignment.

Now that the equipment is ready, place the mirrors on the table such that the waist formed by the mode-matching lens is directly between the flat mirrors and the curved mirrors are a distance $L_2 = 6.8$ cm apart. Position the flat mirrors such that the total cavity length $L = 37$ cm. Make sure the beam passes from mirror to mirror without the crystal holder in the setup. The beam angle Θ as seen on Fig. 3.2 should be about 26° to minimize the asymmetry required in the beamwaists as noted earlier. Once the mirrors are fastened in place, the crystal holder should be positioned symmetrically between the two curved mirrors and the distances verified using a micrometer. Now the following steps should be taken (mirror labels are taken from Fig. 3.2):

1) Use the input couplers to make the beam pass through the centers of flat mirrors

F1 and F2, the couplers should be adjusted in a standard beam walk pattern. The beam should be able to pass through the large aperture alignment jig at any position in this path. The beam alignment jig should be used to check the beam height at each of these steps but will not be mentioned.

2) Using the screws on the back of F2, adjust the beam such that it hits the center of the curved mirror C1.

3) Using the screws on the back of C1, make the beam pass through the crystal and hit the center of C2.

4) If it does not already do so, adjust the screws on the crystal holder such that the beam enters and leaves the crystal at the the exact center of the crystal. Also make certain that the beam goes straight through the crystal and does not reflect off of the side of the crystal while passing through. If the alignment caused the beam to be off-center on C2, then repeat 3) and 4) until both conditions are met.

5) Adjust C2 until the beam hits the center of F1. This should be the same position that the beam passes through from the input coupler.

6) Place the large aperture alignment jig in the path of the beam in front of mirror F2. Adjust the screws on F1 such that the reflection off of F1 also passes through the jig. Provided that the cavity piezo on F2 is ramping over a large enough frequency range, flashes should now be observed when the alignment jig is removed.

7) If no flashes are present then look for multiple spots or perhaps a single very large spot on one of the flat mirrors. Walk mirrors F1 and C2 until the spots coalesce into a single spot and flashes are observed. Alternatively, look at the crystal holder and make sure the second pass of the beam goes through the crystal. Always walk F1 and C2 to preserve the alignment of the initial pass through the crystal.

8) Looking at the reflection dip signal on the oscilloscope, walk F1 and C2 to maximize the dip. Ideally the dip should be around 50% to 60% of the total signal.

9) With the reflection dip maximized, walk the input couplers to maximize the dip further. The input couplers should not need to be moved much.

10) Now that the cavity is aligned, adjust the crystal temperature and record the amount of blue light produced with a photodiode. Set the crystal temperature such that the blue light production is maximized, keeping in mind that the blue light production as a function of crystal temperature has many local maxima. Once the temperature is set to the global maximum for blue light production, measure the reflection dip and doubling efficiency.

11) Using mirrors C1 and C2, change the distance L_2 symmetrically about the crystal. This is done (for example) by moving each of the three screws on the back of both C1 and C2 in (or out) by one turn. It is important that all the screws are moved the same direction to keep the curved mirrors symmetrically positioned about the crystal. This will likely misalign the cavity to the point that no flashes are observed. Repeat steps 7) - 9) to maximize the reflection dip again. If that doesn't help then go back to step 3).

12) Record the blue light efficiency and reflection dip for the new L_2, then repeat step 11) to find the position of the curved mirrors that maximizes the doubling efficiency and reflection dip.

13) Now that the cavity mirrors are at their optimum position, the position of the mode-matching lens can be moved and the input couplers adjusted to fix the cavity alignment. The lens should not need to be moved more than a few cm if the beamwaist measurements were done properly.

Tab. 3.1: Summary of numbers relevant to the performance of the frequency-doubled laser and resonant cavity.

Parameter	Value
Crystal Length (L_c)	3 cm
Nonlinear Coefficient (d_{eff})	10.2 pm/V
Input Power (P_1)	220 mW
Single-Pass Efficiency(calculated) (E_{NL})	0.067 W^{-1}
Single-Pass Efficiency(measured) (E_{NL})	0.0084 W^{-1}
Cavity Finesse(calculated) (F)	73.9
Cavity Finesse(measured) (F)	40
Cavity Free Spectral Range (FSR)	800 MHz
Input Coupler Transmission @ 960 nm (T_1)	5%
Conversion Efficiency(calculated) (ϵ)	74%
Conversion Efficiency(measured) (ϵ)	5.4%

3.5 Cavity Performance

Table 3.1 contains a summary of numbers relevant to the doubling cavity. We can now summarize the details of the doubling cavity by calculating how much blue light we should be able to generate given our measurements thus far. With an input coupler transmission of 5% at 960 nm and a cavity length of 37 cm, the doubling cavity has a calculated finesse of 73.9 and a free spectral range of 800 MHz. The calculated finesse is the finesse that would be observed for a perfectly Gaussian TEM_{00} mode of the appropriate waist and curvature input into the cavity. Experimentally we measure the finesse to be about 40, which is not surprising given that we are using a diode laser with an M^2 value of about 1.5.

In Section 3.3 we calculated the conversion efficiency ϵ to be 74%. This implies that for a 960 nm pump power of 220 mW, we should produce 163 mW of blue light at 480 nm. This is an order of magnitude larger than the amount of blue we currently produce, which is 12 mW. Formerly, with 250 mW input, we were able to produce 71 mW of blue, for a conversion efficiency of 28% compared to the current 5.4 %. In addition, as the power of the pump is increased, the reflection dip ceases to be symmetric, instead displaying a Gaussian rise on one side of the dip, followed by a sharp drop on the other side of the dip. This makes a using a dither lock with the reflection dip to stabilize the cavity length to the laser impossible, so a lock to the side of the resonance must be used as noted in Chapter 2. Since this does not lock to the highest part of the reflection dip, we are in effect throwing away pump light that could otherwise be used to produce additional blue power.

These observations suggest that the performance of the crystal has degraded over time, particularly since we have employed a number of 960 nm diodes in the experiment to the same effect. The calculated vs. measured single-pass efficiency numbers are particularly troubling since this either indicates improper focusing or some form of damage to the crystal. The latter seems the most likely, since the focus of the 960 nm beam was carefully measured and aligned into the crystal as described in the previous section. It is not known exactly what has caused the loss of conversion efficiency or the reflection dip asymmetry, but there are a couple of possibilities. Thermal dephasing could occur whereby the intensity of the pump beam caused local heating in the crystal on a very short timescale that caused the phase-matching to be off for certain wavelengths. In addition, gray tracking is known to occur in PPKTP which could affect the overall doubling efficiency. Gray tracking is a damage threshold effect where a high circulating pump intensity affects the crystal in such a way that along the path of the pump beam there is a track where the crystal cannot produce as much doubled light as

before. This is usually an effect observed in pulsed applications with higher intensities and is thus unlikely in this experiment. Nevertheless, the 5 mW of blue light currently delivered to the atoms has been sufficient for our purposes until this point. It is clear, however, that improvements could be made to increase the 480 nm output power

4. TWO-PHOTON RYDBERG EXPERIMENTS

4.1 Introduction

Now I turn our focus to some basic Rydberg atom experiments designed to investigate the properties of these atoms. First among these concerns is the linewidth of the ground-to-Rydberg state transition, since, in order to achieve the largest blockade volume possible, we must have very narrow linewidths. The linewidths we measured are significantly broader than expected, 8-10 MHz for the energy levels studied in this thesis. Some, though not all, of this broadening is due to the 2 MHz linewidth of the 480 nm laser, thus this laser required some additional investigation. The external cavity used to stabilize the 480 nm laser is subject to thermal and pressure drifts, thus we examine the stability of the 480 nm lock over time.

Still not satisfied with the linewidths obtained from our Rydberg spectroscopy measurements, we developed a novel technique which we refer to as intensity correlation spectroscopy that allows us to measure the Rydberg transition linewidths at timescales shorter than 100 μs. This is done by ramping the 780 nm excitation laser very quickly across the two-photon $5S \rightarrow nS, D$ Rydberg resonance and observing correlated photon counts while the lasers are on resonance, as will be explained in the text. The linewidths measured with this intensity correlation spectroscopy are again 8 MHz, which agrees with our other measurements and eliminates thermal and pressure drift in the laser cavity as possible explanations of the broadening.

After this, we turn our attention to coherent excitation of Rydberg atoms. In a blockade experiment, one would like to coherently transfer the atoms to the Rydberg state and prevent any dephasing process such as decay from an intermediate state. We thus use the process known as stimulated Raman adiabatic passage to excite the atoms into the Rydberg state and then de-excite them back to the ground state. We looked for a reduction in the trap loss rate upon application of the de-excitation pulses, but we observed an increase in the trap loss rate instead, which implies that the excitation/de-excitation process was not coherent. This experiment was unsuccessful for a number of reasons, as would later be appreciated in Ref. [Johnson *et al.*, 2008] which demonstrated the dephasing of Rabi oscillations with more than one atom involved in the excitation. Finally, we look into the possibility of increasing the strength of the atom-atom interactions, and thus the blockade radius, by mixing the pure-D Rydberg level with an F-state via resonant microwaves. We see a 200 MHz Autler-Townes splitting of the Rydberg level with only 0 dBm of microwave power aimed at the vacuum chamber, suggesting that such state-mixing is feasible.

4.2 Rydberg Atom Characteristics

In this work, most of the excitations performed will be to the $28D$, $43D$, $58D$, or $30S$ states. These levels are chosen to cover a variety of atomic radii and atom-atom interaction strengths. In choosing Rydberg levels, we must balance increased interaction strengths at high n-levels with smaller oscillator strengths to low-lying atomic levels that result in smaller signal levels. In particular, the choice of the $43D$ state is a common one in Rydberg atom experiments using Rubidium (see, for example [Li *et al.*, 2005]) because the energy of the $43D + 43D \rightarrow 41F + 45P$ collisional process differs by only 6 MHz from the energy required to excite two atoms along the $5P \rightarrow$

$43D$ transition, creating much stronger interactions among Rydberg atoms excited to this state than would result from van der Waals interactions alone.

The S-state is also interesting since plasma formation takes place much more slowly among these atoms [Li *et al.*, 2004]. This is due to smaller interatomic forces as compared to the forces between D-state Rydberg atoms of the same principal quantum number. This difference between S- and D-states can be understood by realizing that the S-states are only dipole coupled to (and thus interact with) the P-states, whereas the D-states are dipole coupled not only to the P-states but also the F-states. The additional states with which the D-state Rydberg atoms interact means a stronger total interaction and thus a faster progression to plasma formation. The difficulty with using S-states is that the oscillator strengths are typically 1/10 as large as the D-states of the same n-level, making excitation to high levels difficult. When exciting to Rydberg D-states, we have a choice between exciting the atoms to the J=5/2 or 3/2 fine structure level. For all experiments discussed here, we excite to the $J = 5/2$ fine structure level because the dipole matrix element for the $5P_{3/2} \rightarrow nD_{5/2}$ transition is 9 times larger than for the $5P_{3/2} \rightarrow nD_{3/2}$ transition. For our purposes, the Rydberg hyperfine levels are degenerate due to their $\sim$ 10 kHz spacing for n=30, which is smaller than our laser linewidths as we will see.

4.3 Two-Photon Excitation and Linewidth Measurements

If the linewidth of the Rydberg transition is too broad it makes achieving blockade difficult. Consider a case where the Rydberg excitation state for an atom in the ground state is shifted 5 MHz by interactions with a nearby Rydberg atom. If the linewidth of the transition is equal to the natural linewidth of the $58D$ state of 10 kHz then a second Rydberg atom cannot be excited at this location. However, if the linewidth of

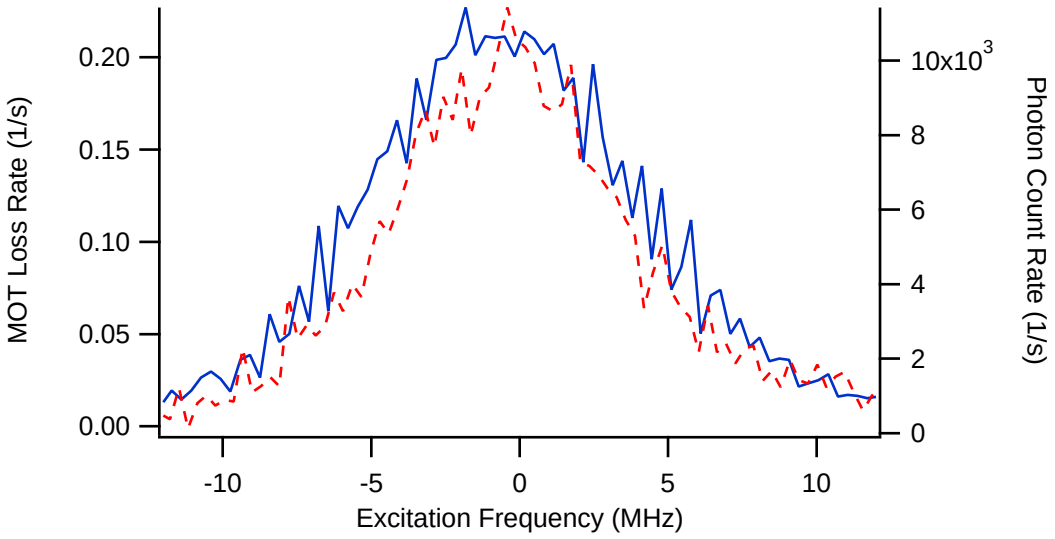

Fig. 4.1: Sweep of Rydberg excitation lasers across the two-photon $5S \rightarrow 28D$ transition. The solid line displays the loss rate from the MOT while the dashed line shows the count rate from the decay of Rydberg atoms through the $6P \rightarrow 5S$ transition. The scan shows that the Rydberg transition linewidth is 8 MHz as measured by both loss rates and count rates.

the transition is 10 MHz then the excitation laser tuned to the Rydberg resonance will still be able to excite a second atom to the Rydberg state, albeit more weakly than without the shift.

4.3.1 Broad Transitions

With this in mind, Fig. 4.1 shows the result of sweeping the 480 nm laser frequency across the resonance of the $28D_{5/2}$. A detailed examination of this figure will help to explain the excitation process. The two-photon excitation of atoms from the $5S_{1/2}$ state in the MOT to the Rydberg state leads to a loss of atoms from the MOT, and thus a reduction of the MOT fluorescence. In the absence of excitation beams, the number of atoms in the MOT comes to an equilibrium when the loading rate (L) from the

background vapor is balanced by light-induced and atom-atom collisions in the MOT which cause trap loss (γ_0). Under this equilibrium condition, the rates are balanced like so:

$$\frac{dN}{dt} = 0 = L - \gamma_0 N. \tag{4.1}$$

The loss rate caused by the excitation lasers (which we refer to as γ_1) should also be N dependent, since having more atoms in the ground state will lead to the excitation lasers producing more Rydberg atoms, and a greater loss rate of these atoms from the trap will result. This induced loss rate will obviously depend on the excitation frequency of the lasers as follows:

$$\frac{dN}{dt} = L - (\gamma_0 + \gamma_1(\nu))N. \tag{4.2}$$

Taking the steady state value of the number of MOT atoms from Eq. 4.2 and solving for γ_1 we find,

$$\gamma_1(\nu) = \gamma_0 \left(\frac{N_0}{N(\nu)} - 1 \right), \tag{4.3}$$

where N_0 is L/γ_0, or the steady state number of atoms in the MOT with no Rydberg excitation. Now we have an equation for the MOT loss rate induced by the excitation lasers in terms of the number of atoms at a particular excitation frequency ν. We will use this loss rate in this and in the next few chapters to determine what happens to atoms in the Rydberg state.

The loss rate γ_1 is displayed on the left vertical axis of Fig. 4.1 as a dashed line. As can be seen, the peak loss rate from the MOT is 0.2 s^{-1}. The excitation lasers are defocused in this setup (as described in Chapter 2), and have Rabi frequencies of 1.1 MHz and 12 MHz for the 480 and 780 nm beams, respectively. Since the detuning from

the intermediate state is 470 MHz, the two-photon Rabi frequency becomes $\Omega_2 = 29.7$ kHz. However, Fig. 4.1 shows that the $1/e^2$ transition linewidth (fitting to a Gaussian intensity profile) is 8 MHz, which means that this broad linewidth will tend to lower the effective excitation rate.

To see why this is, we must use a density matrix treatment of a two-level atom with excited state $|e\rangle$ and ground state $|g\rangle$, as discussed here [Stenholm, 1984]. The excited state decay rate Γ comes into the coherence terms of the optical Bloch equations as,

$$\imath\dot{\sigma}_{eg} = -(\Delta + \frac{\imath\Gamma}{2})\sigma_{eg} + \Omega(\rho_g - \rho_e), \tag{4.4}$$

where Ω is the Rabi frequency for the $|g\rangle \rightarrow |e\rangle$ transition and Δ is the detuning of the laser field from resonance with the transition. In the weak excitation limit ($\Omega \ll \Gamma$) and assuming resonant excitation, the excited state population ρ_e becomes,

$$\rho_e = \frac{\tau_e N_g \Omega^2}{\Gamma}. \tag{4.5}$$

In this equation, τ_e is the lifetime of the excited state and N_g is the number of ground state atoms. For our experiment, this equation implies an effective excitation rate of Ω_2^2/Γ, where Γ is the observed excitation linewidth calculated as noted above. For the data in Figure 4.1, the effective excitation rate is 110 s^{-1}.

We also observe photon counts from the decay of the Rydberg state. These count rates will be discussed in more detail in Chapter 5, for now suffice it to say that a fraction of the atoms that decay from the Rydberg state will make the $6P \rightarrow 5S$ transition. The $28D$ state lifetime of 24.2 μs is much faster than the scanning speed of the excitation lasers, thus the Gaussian width of the count rate as a function of Rydberg excitation laser frequency should be equivalent to the transition linewidth. Figure 4.1 confirms this since the width taken from the count rate data is 8 MHz, which agrees with the width as measured by the loss rate data.

We will return to the implications of these loss rates in Chapter 5. For now, the width of the Rydberg transitions is our chief concern. The linewidths for all levels studied are routinely 8 to 10 MHz. This is much broader than the natural linewidth of around 6 kHz for the $28D$ state or the even the $\sim$ 200 kHz Doppler broadened width [Svanberg, 2001] assuming a mean temperature of 100 μK. The largest contribution from the lasers to this width is the 480 nm laser where the 1 MHz short-term self-homodyne linewidth (see Chapter 2) of the 960 nm diode results in a 2 MHz linewidth at 480 nm. By comparison, the short-term 780 nm laser linewidth measured in the same manner is 200 kHz. Thus even the quadrature sum of both the 780 nm and 480 nm laser linewidths is about a factor of 4 less than the observed transition linewidth. It is possible that the 480 nm laser could drift during these scans since the scans take a around two minutes to accomplish. The scan speed is chosen such that the time taken to cover the Rydberg resonance is much longer than the loading rate of the MOT. Thus, we wish to investigate the drift rate of the 480 nm laser lock.

4.3.2 480 nm Stability

As discussed in Chapter 2, the 960 nm laser diode is locked to a temperature-stabilized Fabry-Perot reference cavity with a free-spectral range of 1 GHz and a finesse of 200. The locking linewidth of the 960 nm laser has been measured to be an average of 1 MHz with spikes of no more than 2 MHz by observing the amplitude jitter of the Fabry-Perot signal on an oscilloscope. However, temperature and pressure drifts in the FP cavity could still cause broad linewidths to be observed. To ascertain what effect these drifts have, we use the MOT itself as a frequency reference. We tune the 480 nm laser to the edge of a Rydberg transition, such that we eliminate about 1/3 of the MOT fluorescence signal. We may then use the computer control to feedback to the blue frequency such that the MOT fluorescence remains at this level. Since the

Rydberg transition for the MOT atoms does not drift, any frequency change required to keep the blue laser tuned to the Rydberg resonance is a result of a change in the length of the reference Fabry-Perot cavity. We now have a way of recording the drift of the reference cavity length over time.

Figure 4.2(a) shows the frequency drift of the 480 nm laser with and without the pressure seal of the acrylite box containing the Fabry-Perot. As the figure shows, without the seal, the laser drifts by as much as 5 MHz in a minute, whereas with the seal the drift rate is reduced to $\sim$ 1 MHz per minute, and is most likely caused by temperature fluctuations in the cavity. Thus it should be clear that the 480 nm laser cannot be responsible for our observed transition widths. However, there is some concern that unaccounted for mechanical vibrations in the optical table holding the diode lasers might be causing these widths. To test this, we devised a novel method of observing the short term linewidths of these transitions.

4.3.3 Intensity-Correlation Spectroscopy

If we could sweep our lasers over the resonance much faster than the vibrational time ($\sim$ 10 ms) we would be sensitive only to the short-term laser linewidth. Unfortunately, the MOT loading time is much longer than these fluctuations, and so we cannot use MOT fluorescence as an excitation metric at these speeds. Similarly, the count rates measured from the decay of the Rydberg state are too small to obtain a signal large enough to be usable with a single pass over the resonance. Count rates of $\sim 10^4$ s^{-1} as seen in Fig. 4.1 imply that if we sweep across the resonance on a 100 μs timescale we are likely to get no more than a single count as a result of the sweep. This makes it impossible to determine when the lasers are on resonance, much less how wide the resonance is. However, since the dark count rate for the scan in Fig. 4.1 is 30 s^{-1}, we are 300 times more likely to observe a count from Rydberg atom production and

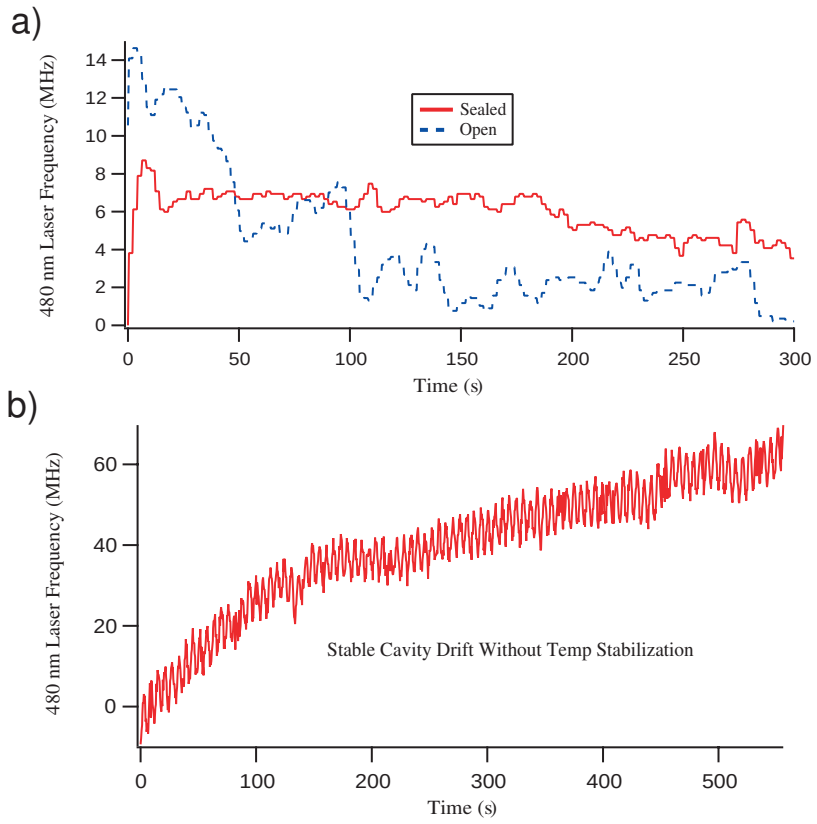

Fig. 4.2: Graphs showing fluctuations of the blue laser while it is stabilized to the side of the Rydberg transition. The frequency drift is due to a change in the length of the Fabry-Perot cavity. Figure (a) displays the frequency drift with the acrylite box sealed and with the valve open, allowing pressure changes in the room to cause the frequency to drift. The 6 MHz shift at the start of the sealed box data is caused by the laser coming into resonance with the side of the Rydberg transition. Figure (b) shows the drift caused by turning off the temperature control. The ringing observed in (b) is due to the high gain of the feedback loop which stabilizes the laser frequency to the side of the Rydberg transition. With both pressure and temperature controlled, the laser drifts no more than 1 MHz per minute.

subsequent decay than we are from background when excitation lasers are directly on resonance. If the excitation lasers are swept rapidly back and forth across the Rydberg transition, any counts that result are most likely a result of Rydberg atom production. This suggests that by recording the delay time between successive photon counts while the excitation lasers are swept that we may probe the width of the Rydberg transition. As we will see, the histogram of the photon delay times will be an auto-correlation function of the Gaussian intensity profile of the Rydberg state transition.

For this purpose, we ramp the 780 nm laser with a triangle ramp at a frequency between 30 kHz and 10 Hz. The ramp and the corresponding histogram of the photon delay times can be seen in Fig. 4.3. The coincidence counts seen in Fig. 4.3(b) are recorded as follows: the arrival of a count triggers a sweep on the pulse counting card. The card then records the time taken until the next photon is observed, at which point the sweep ends. As counts are more likely with the laser on resonance rather than off, a sweep is generally triggered when the 780 nm laser is on resonance with the two-photon Rydberg excitation frequency. Once the sweep begins, the fact that the excitation beam is on resonance with the Rydberg transition means that we will see many tightly bunched photon counts on the coincidence delay time histogram, which is why we start off with a peak as seen the figure. The figure demonstrates that generally counts will only be observed when the excitation lasers are sweeping over the resonance, which explains the other six peaks observed in the figure. Due to the triangle ramp, the "odd numbered" peaks (peaks 3, 5, and 7 counting from the left in the figure) are produced with the ramp going in the same direction as it had been for the first peak, whereas for the "even numbered" peaks (2, 4, and 6) the ramp is sweeping the opposite direction than the initial peak.

As is shown in Fig. 4.3(b), the odd peaks have a larger amplitude and narrower width than the even peaks. As the laser frequency drifts, the position of the resonance

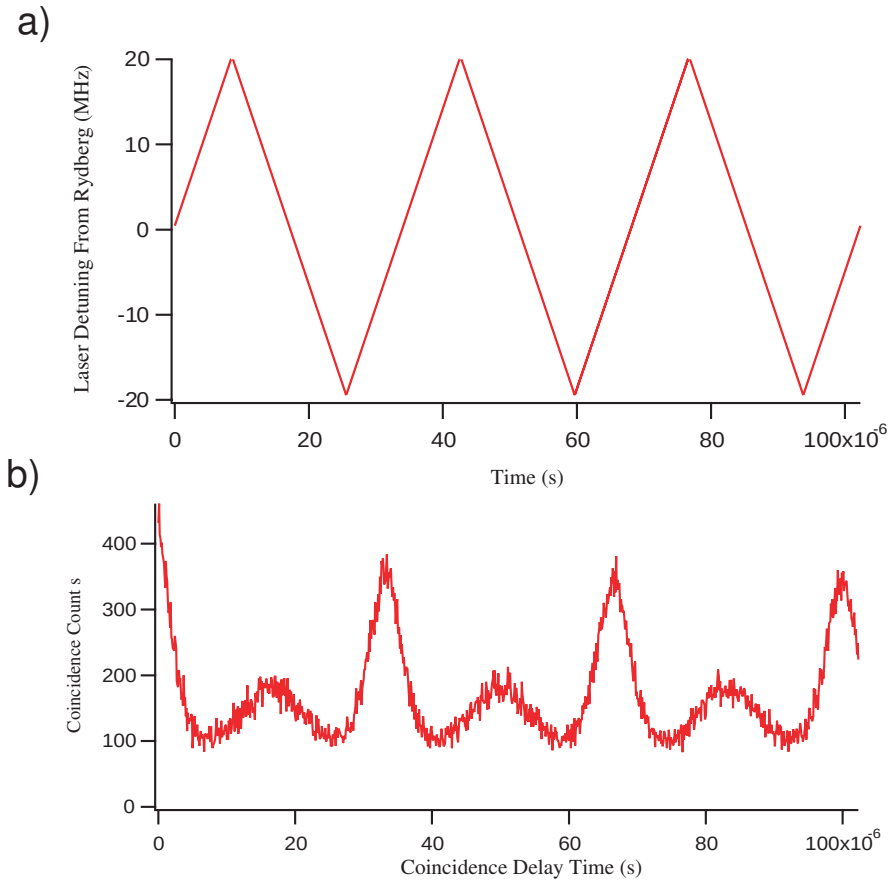

Fig. 4.3: Figure (a) displays the ramp applied to the current of the 780 nm excitation laser and the detuning of the laser from the Rydberg transition. The frequency of the ramp is 30 kHz. Figure (b) is a record of the correlated photon counts observed during the scan. The "odd numbered" peaks are sharper and less spread out than the "even numbered" peaks because the ramp is moving in the same direction for these, making them insensitive to drift in the laser frequency. Note that while the ramp is pictured with the frequency increasing at the start of the sweep, the ramp could just as easily be decreasing initially for a given correlated photon pair.

on the ramp will also drift. This drift occurs such that the odd numbered peaks move in the same direction, or in a common mode, relative to the initial peak. Thus they have the same temporal displacement (set by the ramp period) from the initial peak in the graph and are not spread out. Likewise, the even numbered peaks move in the opposite direction, or in a difference mode, relative to the initial peak and thus get closer to and farther away from the initial peak as the laser drifts. This causes the even numbered peaks to become spread out and broader relative to the odd peaks. This also means that since the drift does not spread out the odd peaks, these peaks are insensitive to drifts and fluctuations on timescales longer than the ramping period. We may then measure the width of the odd peaks at a range of different ramping frequencies to get an idea of the timescales of the thermal and mechanical fluctuations present in the experiment. The derivation of the dependence of the width on the transition linewidth is presented in Appendix A. The result is that the odd peaks have a Gaussian profile with a $1/e^2$ width which is $\sqrt{2}$ larger than the transition linewidth.

Figure 4.4 displays the result of a number of linewidth scans taken with the ICS method at different ramping frequencies. In the figure, the Rydberg linewidths are as large as 20 MHz for the slowest ramping frequencies and reduce to 8 MHz at a 10 kHz ramping frequency. The 10 Hz ramping frequency linewidths are much larger than that observed by the two-photon excitation scan shown in Fig. 4.1 because the 780 nm laser is locked to a saturated absorption transition for the data taken in the figure, whereas in the ICS setup the 780 nm laser is allowed to drift as the frequency is swept back and forth. Figure 4.4 was taken using the $28D$ state, however the ICS linewidths for the other excitation states are still no more than the 8 MHz seen here. The linewidth appears to be coming to an equilibrium at the highest ramping frequencies, unfortunately the ramping frequency cannot be increased any further since the effective lifetime of the Rydberg state is around 100 μs. Ramping faster than the Rydberg lifetime means

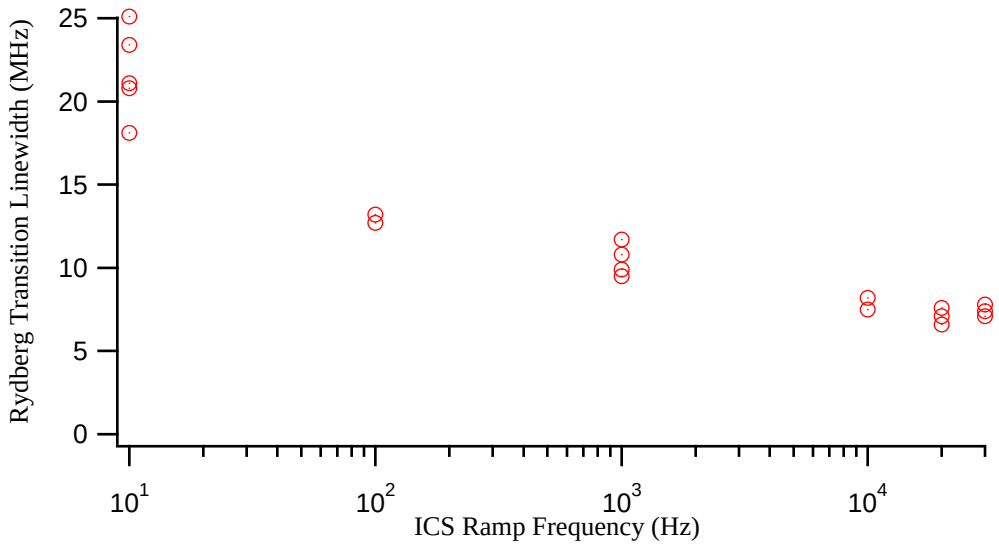

Fig. 4.4: A summary of ICS linewidth scans for the 43D state. The width of the transition is measured to be over 20 MHz at small ramping frequencies because laser frequency drift acts to spread out the linewidth on this timescale. At higher frequencies, the linewidth reduces to 8 MHz.

that the atoms do not have time to decay before the laser is on resonance again. This acts to reduce the contrast between the peaks and the background, and it turns out that ramping much faster than 10 kHz reduces the signal to noise ratio too much to get a reliable signal.

4.3.4 Other Possibilities

So it is clear that even at short timescales the transition linewidths are much larger than we anticipate, but there is still the question of 'why'? Unfortunately, we know very little about what causes these transitions to be so broad. On the other hand, we do know a great deal about matters that are not a source of broadening. A key point here is that the linewidths are about the same width regardless of the n-level to which we excite. This means that explanations with an n-dependent effect, such as stray electric

or magnetic fields, cannot be the cause. Atomic collisions or plasma formation are likewise eliminated, and regardless these would not be a factor at the lowest densities at which we perform our excitations, as we will see in Chapter 5. It is still conceivable that some vibration in the lab that is picked up by our lasers may be causing this broadening, but we have looked at the short term linewidth and the locking linewidth of each laser and found no evidence of this. In the literature and from private communication, it is clear that other groups see similar linewidths ([Singer *et al.*, 2004], [Teo *et al.*, 2003], [Amthor *et al.*, 2007]), though there are exceptions [Grabowski *et al.*, 2005].

4.4 STIRAP

As a test of our control of the system, we would like to be able to coherently drive atoms into the Rydberg level and then back down into the ground state. This will require that we focus our excitation beams so that we perform the entire excitation cycle faster than the lifetime of the Rydberg state. This is because spontaneous decay acts to dephase the transition cycle resulting in equal populations in the excited and ground states. However, there are numerous problems with focusing the excitation beams, not the least of which being that focused beams will lead to larger Rydberg atom densities and thus stronger atom-atom interactions. These interactions have been shown to result in plasma formation in less than 1 μs [Li *et al.*, 2004] for D-state excitations. This time is slightly longer for S-states, but regardless it is necessary for the excitation rate to exceed this timescale, which is difficult given that the width of the Rydberg transitions reduces our effective excitation rate.

The focused beams lead to other problems as well, namely the differential AC Stark shifts mentioned in Chapter 2 as well as differential excitation rates over the atomic sample. The quoted excitation rates in these experiments are calculated for peak in-

tensity, thus over the spatial extent of the Gaussian beam the excitation rate will vary from the peak rate to zero. We then have a problem of demonstrating coherent excitation and de-excitation from the Rydberg state. A Rabi-flopping experiment where population oscillations between excited and ground states are observed when the excitation beam is applied will not work because the differential excitation rates make the atoms oscillate at different frequencies. These frequencies will wash out the fringes since the frequencies drift in and out of phase with each other.

4.4.1 Theory

Stimulated Raman Adiabatic Passage (STIRAP) deals with the problem of differing oscillation frequencies in a two photon excitation by bringing atoms around the Bloch sphere at different speeds, but having them all reach the excited state at around the same time. This works by using a counterintuitive sequence of pulses which serve to change the basis state of the three levels involved. The new basis states are such that as long as the excitation rates change adiabatically the atoms will stay in the same "dressed" state while making a transition from the ground to the Rydberg level in the original basis state configuration. A good review article of the STIRAP process can be found here [Bergmann *et al.*, 1998], I will provide here a summary of arguments presented in more detail in the article. Consider two Rabi frequencies: Ω_r represents the 780 nm laser excitation, and Ω_b represents the 480 nm laser excitation. Following the discussion in [Bergmann *et al.*, 1998], we may define a time-varying mixing angle Θ between the ground $|g\rangle$, intermediate $|p\rangle$, and excited $|r\rangle$ states as follows,

$$\tan\Theta(t) = \frac{\Omega_r(t)}{\Omega_b(t)}. \tag{4.6}$$

In the dressed state picture of the atomic transition, the three atomic states can be

represented as a superposition of the three "undressed" states with new wavefunctions $|a^+\rangle$, $|a^0\rangle$, and $|a^-\rangle$ according to:

$$|a^+\rangle = \sin\Theta\sin\Phi\,|g\rangle + \cos\Phi\,|p\rangle + \cos\Theta\sin\Phi\,|r\rangle \quad (4.7)$$

$$|a^0\rangle = \cos\Theta\,|g\rangle - \sin\Theta\,|r\rangle \quad (4.8)$$

$$|a^-\rangle = \sin\Theta\cos\Phi\,|g\rangle - \sin\Phi\,|p\rangle + \cos\Theta\cos\Phi\,|r\rangle \quad (4.9)$$

The other angle, Φ, is a function of the two Rabi frequencies and the intermediate state detuning, but has no impact upon the final result. So as we can see from Eq. 4.9 the atoms begin in state $|a^0\rangle$, which is equivalent to state $|g\rangle$ with $\Theta = 0$ (as the blue begins to turn on). Substituting $\Theta = 0$ into Eqs. 4.8-4.9 shows that the other states in the dressed state picture are orthogonal linear combinations of $|p\rangle$ and $|r\rangle$. The 480 nm laser comes to full power first, and as the 480 nm laser turns off the 780 nm laser begins to turn on, making the mixing angle go from 0 to $\pi/2$. Substituting $\Theta = \pi/2$ into Eq. 4.9, one can see that although the dressed state stays in the $|a^0\rangle$ state, this state now corresponds to the undressed state $|r\rangle$. The other two dressed states are now linear combinations of $|g\rangle$ and $|p\rangle$, so the transition has occurred without ever populating the intermediate state.

The only condition for this to occur is that the excitation has to be adiabatic, which is satisfied when $\Omega_{eff}\Delta t > 10$, where Ω_{eff} is the quadrature sum of the Rabi frequencies and Δt is the time for the excitation. If a faster excitation rate is used, the atoms will tend to transition into one of the other state vectors $|a^+\rangle$ and $|a^-\rangle$, each of which has a component of the intermediate state in it. To smoothly turn on and off the beams, we added an AOM to the 480 nm laser setup. The voltage-controlled oscillators (VCO) supplying RF power to the AOM's on the 480 and 780 nm beams were also equipped with analog switches so that we could turn the excitation lasers on

and off in an adiabatic fashion. Most importantly, for this system it does not matter what the Rabi frequency of the lasers on the atoms is, so long as there is enough Rabi frequency to get the atoms into the excited state by the end of the excitation time.

4.4.2 Setup and Results

To confirm that coherent excitation via STIRAP has occurred, one must in general show that over 50% of the atoms in the excitation beams were excited to the Rydberg level. Georg Raithel's group at Michigan has observed coherent excitation using the STIRAP technique of up to 70% Rydberg excitation, using an MCP to record the number of Rydberg atoms produced [Cubel *et al.*, 2005]. They did not, however, observe subsequent de-excitation from the Rydberg level. As we do not have a convenient method for determining instantaneous Rydberg state populations, we instead followed our excitation pulse sequence with a similar counter-intuitive pulse sequence (to wit, Ω_r followed by Ω_b)to drive Rydberg atoms back into the ground state. This is similar to the application of two successive π-pulses in NMR spectroscopy. Since the excitation of Rydberg atoms increases the observed MOT trap loss, we then searched for such increase in trap loss when the excitation pulse sequence occurred followed by a relative decrease in trap loss when the de-excitation sequence was applied. Figure 4.5 shows the actual pulses that were applied to the atoms.

The intermediate state detuning for this experiment was zero, so the 780 nm laser and 480 nm laser frequencies were tuned directly to the $5S \rightarrow 5P$ and $5P \rightarrow 43D$ transitions respectively. The MOT lasers were switched off briefly during the STIRAP process. The Rabi frequency of the 780 nm laser was 30 MHz (or a $4.77\times10^6 \mathrm{s}^{-1}$) and the total excitation time 3 μs (as shown in Fig. 4.5), so the adiabaticity condition for the excitation is $\Omega_{eff}\Delta t = 14$ which is barely met for this interaction. I only include the 780 nm Rabi frequency in this calculation since the 480 nm Rabi frequency is smaller

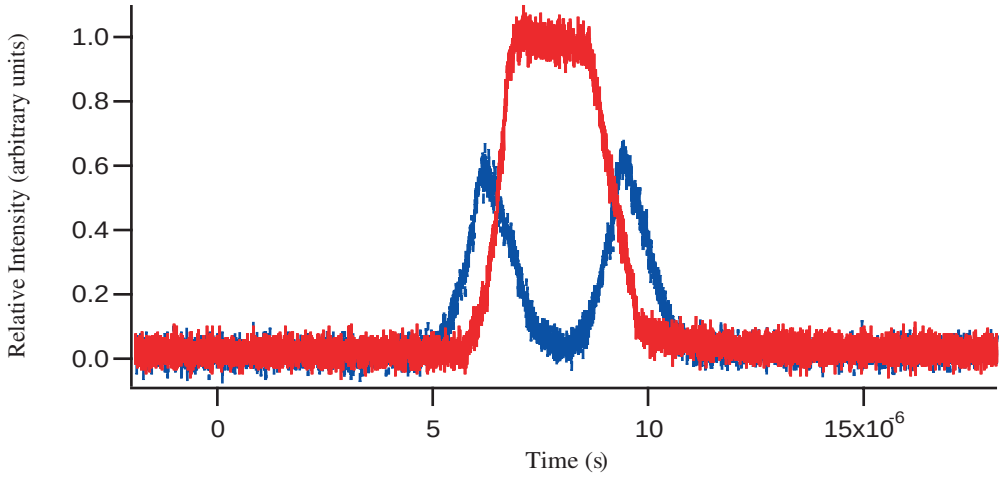

Fig. 4.5: Figure displays the pulses used in the STIRAP experiment. A pair of excitation pulses followed by a pair of de-excitation pulses are applied. For the excitation sequence, the 480 nm light (dashed line) turns on first, then is switched off adiabatically while the 780 nm pulse (solid pulse) turns on. The pulses are temporal Gaussians in Rabi frequency.

for one and this excitation rate must take into account the width of the Rydberg transition for another. Thus the quadrature sum of the effective Rabi frequency Ω_{eff} is dominated by Ω_r.

As the figure shows, the excitation pulses are 2 μs wide and are approximately temporal Gaussian functions in terms of Rabi frequency. The pulses appear more sharply peaked than a Gaussian function would be because intensity is proportional to the square of the Rabi frequency. The figure shows a set of excitation pulses followed by a set of de-excitation pulses. We performed experiments with a range of different delays between the peaks of the 480 nm and 780 nm pulses, but these made little difference in the experimental results which always showed that application of the excitation and de-excitation pulses as shown in Fig. 4.5 resulted in more MOT trap loss than the application of the excitation pulses alone. We also varied the total excitation time from 2 μs to as much as 10 μs by increasing the pulse widths to $4\mu s$ but with similar results.

In summary, STIRAP excitation and de-excitation was never successfully observed with our setup in this manner. As we now know, atom-atom interactions are strong enough in Rydberg states that coherent excitations are dephased not only by these interactions but also by interactions with free electrons and by superradiance to nearby Rydberg levels as we will see in Chapter 6. The effective two-photon excitation rate is larger for this process than for the linewidth scans owing to the lack of an intermediate state detuning and the focused beams; thus we expect these densities to be exceeded, and there is no great surprise in retrospect that the STIRAP process revealed no coherent excitation.

4.4.3 Lock-in Detection

There is still the possibility, however, that Rydberg excitation detuned slightly from the Rydberg state could excite pairs of atoms along a repulsive potential which would inhibit collisional processes. Collisions will tend to dephase the STIRAP process, so excitation performed at such a detuning should exhibit a smaller loss rate when the excitation and de-excitation pulses are applied as compared to the resonant case. The difficulty with such a measurement is that any detuning from the Rydberg state will necessarily reduce the observed loss rate since fewer atoms will be excited to the Rydberg level. In addition, since the blue laser frequency drifts at the rate of ~ 1 MHz per minute, we need to determine whether or not the STIRAP process is effective at the desired Rydberg state detuning before the laser drifts away from the desired Rydberg state detuning. To deal with this loss in detection sensitivity, we opted to use a lock-in amplifier to monitor the MOT loss rate for small changes while sweeping the excitation laser frequency across the Rydberg transition.

This worked by alternating between the two-pulse excitation sequence and the four-pulse excitation and de-excitation sequence (in other words alternating between one π-pulse and two π-pulses) by a TTL signal from the lock-in amplifier. The pulses had a repetition rate of 5 kHz to increase their effect on the MOT while still allowing all Rydberg atoms produced to decay before the arrival of the next pulse sequence. The switch from one to two π-pulses occurred with a frequency of 0.25 Hz to allow the MOT to reload slightly between excitation and de-excitation processes. To clarify, every 200 μs the MOT was hit with the $3\mu s$ long excitation pulse sequence. This continued for 2 s, at which time the excitation pulses were followed immediately by the de-excitation pulse sequence as seen in Fig. 4.5. The MOT was hit by the excitation plus de-excitation pulse sequence every 200 μs for the next 2 seconds at which point the switch

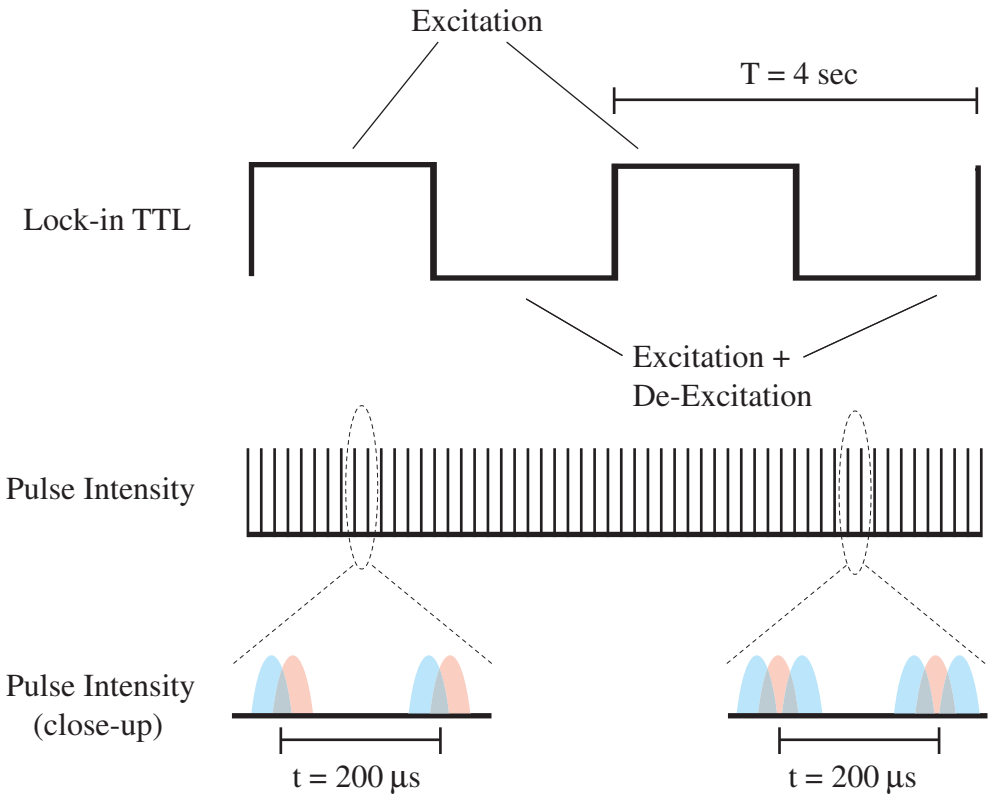

Fig. 4.6: Pulse sequence for the lock-in detection of STIRAP.

back to excitation pulses occurs. This pulse sequence is displayed in Fig. 4.6. If the de-excitation pulses bring Rydberg atoms back into the ground state then the MOT loss rate should decrease relative to the π-pulse sequence. This should cause a sign change in the lock-in detector error signal when the phase is appropriately calibrated.

The result of such a scan is shown for the $43D$ state in Fig. 4.7. The figure demonstrates that when the two π-pulse sequence is applied, the loss rate from the MOT increases, regardless of the Rydberg state detuning. This implies that the process is not coherent, and that the second π-pulse brings more atoms up to the Rydberg state (assumedly during the brief period when both the 780 and 480 nm lasers are on) than it

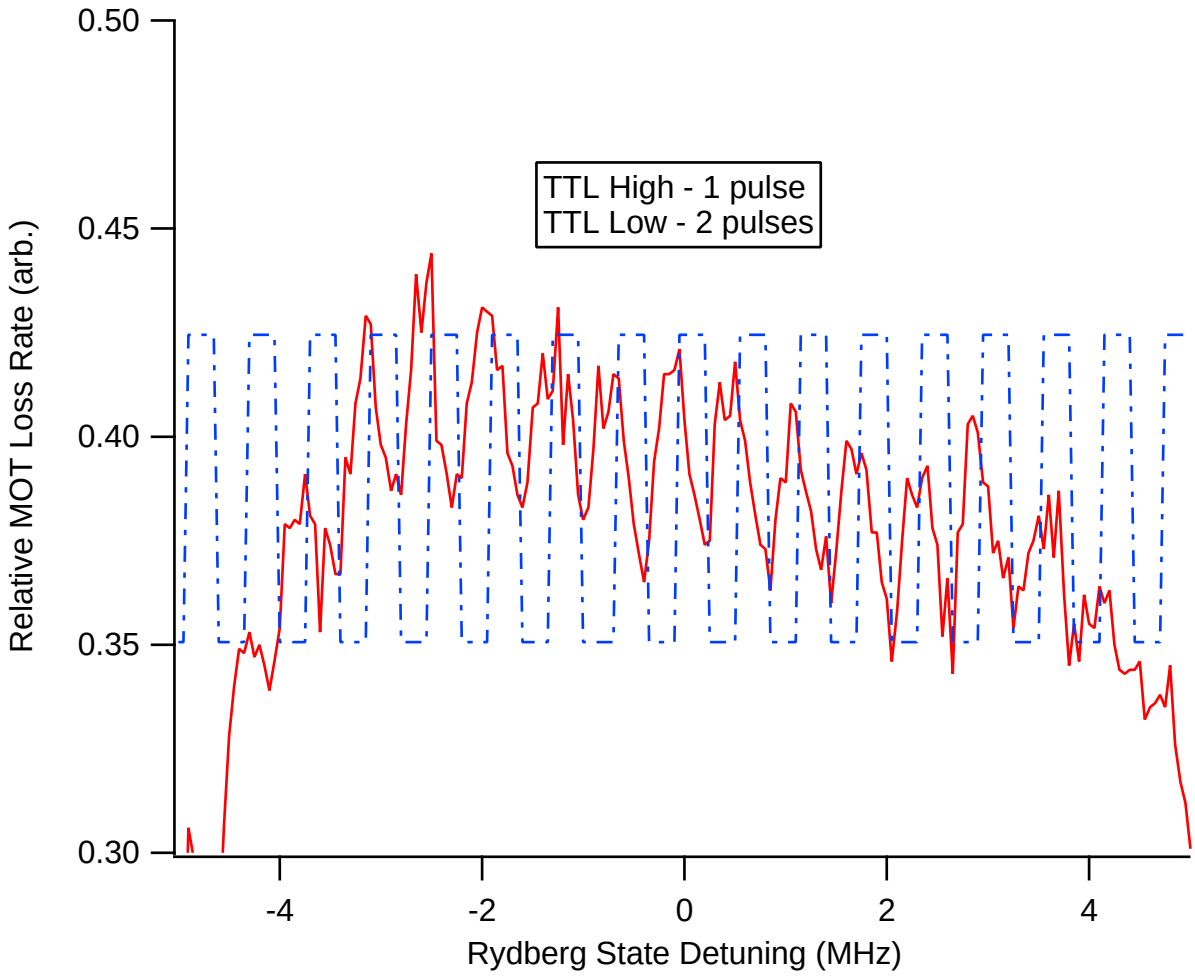

Fig. 4.7: Figure displays the lock-in error signal (solid line) along with the TTL signal (dashed line) switching between the excitation pulses and the de-excitation pulses. When the TTL signal (which is modified to fit on the graph) is "high", only the excitation pulses are applied. When the TTL signal is "low", the excitation pulses are immediately followed by a set of de-excitation pulses as shown in figure 4.5. An increase in the error signal indicates an increase in the MOT loss rate, and the figure demonstrates that the de-excitation pulses increase rather than decrease the MOT loss rate regardless of Rydberg state detuning.

de-excites from the Rydberg state to ground. This is a difficult measurement to make at any rate, a computer model of the excitation process implied that at best around 60% of the atoms in the excitation beams would be excited up to the Rydberg level.

4.5 Microwave Excitation

Now that we have looked in detail at the Rydberg excitation process, we wish to look at the issue of Rydberg-Rydberg interactions. In order to achieve the dipole blockade necessary for any single-photon-source scheme, we must make the blockade radius as large as possible. The blockade radius as noted here refers to the distance from a Rydberg atom within which a second atom cannot be excited to the Rydberg level because of an energy shift imparted by the Rydberg atom. This radius must be at least as large as the excitation volume which is defined by the intersection of beams with at best a 12 μm beamwaist. As we will see, dressing the Rydberg state with resonant microwaves offers a simple way to enhance the interaction strength of the atoms.

4.5.1 van der Waals and Dipole Interactions

Ordinarily, atoms with a pure D-state or S-state character interact via van der Waals forces which scale as $\sim \mathrm{C}_6/\mathrm{R}^6$. If we can make states with wavefunctions in opposite parity states interact, we may instead cause the atoms to experience dipole-dipole interactions. These interactions have the form

$$V_{dd} = \frac{\mathbf{d}_1 \cdot \mathbf{d}_2 - 3(\hat{R} \cdot \mathbf{d}_1)(\hat{R} \cdot \mathbf{d}_2)}{R^3} \tag{4.10}$$

and are much stronger than van der Waals interactions, owing to the R^{-3} scaling. In this equation, $\hat{R}$ is the unit vector in the direction of the interatomic separation

vector $\mathbf{R}$, and $\mathbf{d}_1$ and $\mathbf{d}_2$ are the dipole moments of the two atoms. Another issue is that for any given Rydberg level there exist linear combinations of magnetic sublevels with zero interaction potential between them [Walker and Saffman, 2008]. For both of these reasons, it becomes advantageous and in fact necessary to couple the atoms with a pure D-state character together with F- or P-states that will produce dipole-dipole interactions among the atoms.

4.5.2 Setup

There are various ways in which to dipole couple atomic states with microwaves. The simplest is a directly resonant microwave beam coupling the Rydberg excitation state to a nearby F or P state. An example of such a setup can be seen here [Afrousheh *et al.*, 2006]. A problem with such a setup is that AC Stark shifts will act on the magnetic sublevels of the Rydberg state in differing amounts, breaking the degeneracy and potentially broadening the transition. A different method would be to dress the Rydberg state with two off resonant microwave beams, one tuned above the resonance and one tuned an equal amount below it. This ensures that the AC Stark shifts from the two beams cancel each other while still mixing the D state with a state of opposite parity. Another method involves using the AC Stark shift of the microwaves to shift the molecular $41F + 45P$ into resonance with the $43D + 43D$ [Bohlouli-Zanjani *et al.*, 2007].

For these experiments, we used the directly resonant method since it was the easiest to implement. We coupled microwaves at 10.65 GHz into the vacuum chamber by means of a microwave generator connected to a transmitter and horn to direct the microwave beam. The horn was pointed in the direction of the vacuum chamber, but no careful alignment of the microwave beam was made. The atoms are very sensitive to microwaves and have oscillator strengths on the order of unity. Thus fine tuning

of the system is not necessary. The Rydberg excitation state for this experiment was the $60D$ state and was chosen because of the need for a high enough Rydberg state to match the narrow (5-12 GHz) frequency range of our microwave source. This Rydberg state was coupled to the $59F$ state, which is the nearest state in energy to the $60D$. The power out of the microwave generator varied from -40 dBm to 0 dBm though it is likely that several orders of magnitude in intensity are lost before the microwaves reach the atoms.

4.5.3 Autler-Townes Splitting

With the microwaves tuned directly to the $60D \rightarrow 59F$ transition, the Rydberg excitation lasers are swept across the two-photon $5S \rightarrow 60D$ transition. Figure 4.8 shows several of these sweeps for various microwave power levels as shown. For the highest microwave power (0 dBm), the result is a 200 MHz Autler-Townes splitting of the Rydberg excitation peak into a $|D\rangle + |F\rangle$ peak and a $|D\rangle - |F\rangle$ peak. This implies that the Rabi frequency of the microwaves on the atoms is 200 MHz as well. By taking into account the oscillator strength of the transition, we calculate that the intensity of the microwaves at the atoms is around $3{\times}10^{-6}$ W/cm^2, smaller than the one would expect if all of the microwaves from the generator diffracted out from the horn into the vacuum chamber. Part of this is due to losses in the cable transmitting the microwaves, and part is due to grounding from the vacuum chamber itself. Since the vacuum chamber port is only 5.1 cm in diameter, this means that microwaves on the order of this wavelength (corresponding to a frequency of 5.8 GHz) and longer will be heavily attenuated. Still, the main point to be taken from these experiments is that it is very easy to couple these Rydberg levels to opposite parity Rydberg states with very modest microwave intensities.

For our ongoing experiments, we have obtained a new microwave generator which

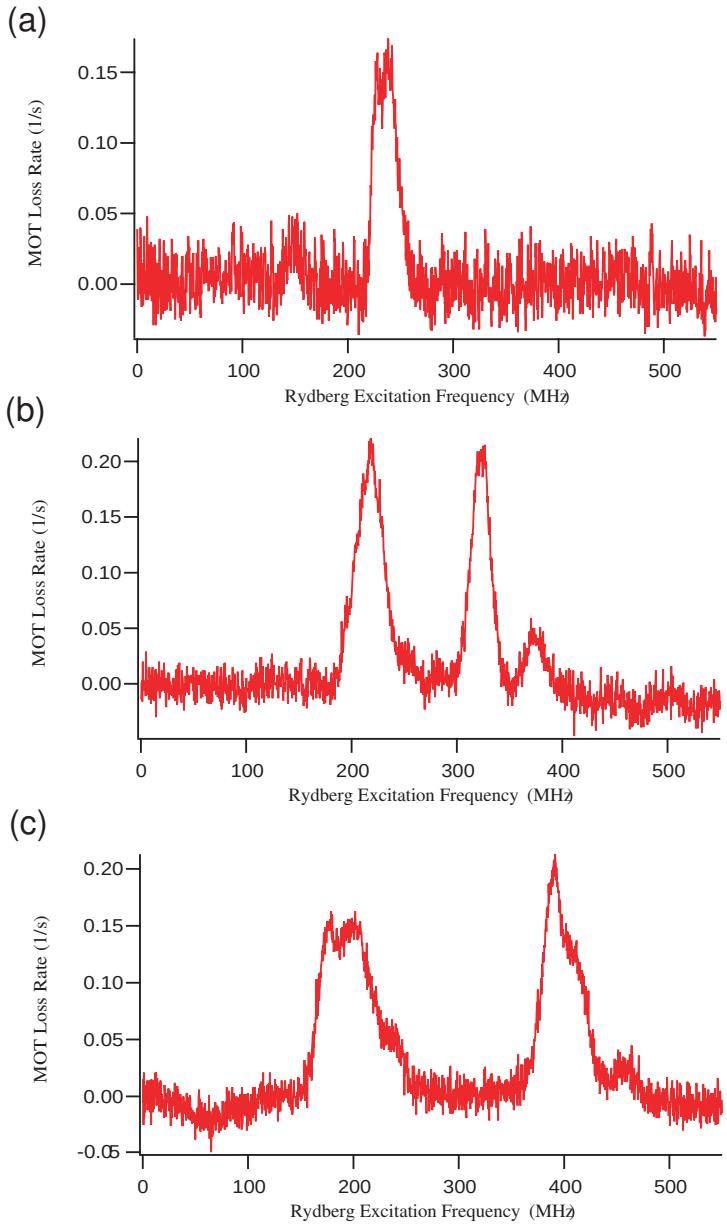

Fig. 4.8: The figure shows sweeps of the Rydberg excitation laser frequency across the 60D resonance with (a) the microwaves turned off, (b) -6 dBm of microwave power, and (c) 0 dBm of microwave power at 10.65 GHz emitted from the microwave transmitter. An Autler-Townes splitting of 200 MHz can be observed with the microwave power at 0 dBm.

allows us to utilize microwave frequencies as high as 40 GHz. We then excite atoms to the $43D$ Rydberg level and couple the atoms, with a slight detuning, to the $42F$ state using microwaves at 29.657 GHz. Though no data from this experiment is available at the time of this writing, initial observations suggest that the detuning from the $43D \rightarrow 42F$ transition causes one of the Autler-Townes peaks to be slightly larger than the other. In addition, it appears as though the smaller peak has a linewidth less than 8 MHz. A possible explanation of this observation would be that the small detuning of $\sim$100 MHz from the resonant case causes one of the Autler-Townes peaks to have more of an F-state component than the larger Autler-Townes peak. This effect, if correct, is strange and further experimentation will be needed to determine why this might occur. Nevertheless, a narrow linewidth transition that exhibits dipole-dipole interactions with neighboring atoms would be very useful in obtaining a strong blockade region.

5. RYDBERG GAS DYNAMICS

5.1 Introduction

Now we turn our attention to the fate of the Rydberg atoms excited produced by our excitation lasers. Experiments by other groups (e.g. [Walz-Flannigan *et al.*, 2004] and [Li *et al.*, 2004]) have shown that when Rydberg atom densities approach 1×10^8 cm^{-3}, atom-atom interactions are strong enough that the atoms transfer to Rydberg levels other than the excitation Rydberg state in hundreds of nanoseconds in the case of D-state Rydberg atoms and a few microseconds for S-state Rydberg atoms. In addition, Rydberg atoms at these densities are quickly ionized and produce a plasma of free electrons which in turn ionize other Rydberg atoms. In the experiments discussed in this chapter, we wish to observe the effects of Rydberg atom excitation at densities less than the 10^8 cm^{-3} in the aforementioned studies in order to operate in a regime where Penning ionization and plasma formation have a negligible effect.

We have two methods for measuring Rydberg atom populations: trap loss from the MOT and photon decay from the $6P_{3/2}$ state. These diagnostics allow us to monitor the dynamics of the Rydberg state, and have never been used in this manner by any other research group. One of the motivations for performing these experiments at lower densities is then to utilize these new diagnostic tools within a regime where the results may be more easily interpreted than at high Rydberg atom densities with numerous collisional processes affecting our measurements. As we will see, data from both of these

sources imply that many atoms are transferred out of the excitation Rydberg state, but that inelastic collisions are not a factor in this transfer process. We then employ a "state-probe" laser, another novel method, to bring the atoms down from the excitation Rydberg state before they are transferred out of the state by some other process. By varying the intensity of the state-probe laser, we determine the rate of the transfer process. We compare the transfer rates at different principal quantum numbers and conclude that collisions and blackbody transfer cannot explain the observed transfer rate. Finally, we develop a three level model for Rydberg state interactions which allows us to quantify Rydberg state transfer rate.

5.2 Trap Loss Studies

As shown in Chapter 4, Fig. 4.1 shows the results of sweeping the two-photon excitation frequency through a typical Rydberg resonance. Loss rates induced by the excitation lasers are around 0.2/s, a rate much smaller than the 110/s Rydberg excitation rate. We may infer from this that the probability of inelastic collisions among Rydberg atoms occurring with sufficient energy transfer for the atoms to leave the trap is less than 1/500. For the other states studied, we find 1/50 for 43D and 58D, and 1/1000 for the 30S state.

Trap loss probabilities are significantly higher for 43D and 58D as compared to 28D; a logical hypothesis to explain this result would be that inelastic collisions are responsible for the trap loss. To this end, we compared the trap loss rates from 41D and 43D, and found little difference. As noted in Chapter 4, the energy difference between the 43D + 43D and 41P + 45F potentials is 6 MHz and since the van der Waals interaction strength between 43D state atoms is inversely proportional to this "energy defect", the interaction strengths at this Rydberg level are anomalously large. However,

the analogous energy defect between the 41D + 41D and 39P + 43F potentials is 196 MHz. The much larger energy defect as compared to the 43D state implies that the interaction strength between 41D atoms would be a factor of 32 smaller, and we would thereby expect to observe very different results between these two states were collisions responsible for trap loss. Thus we again find no evidence that resonant energy transfer collisions cause significant trap loss.

The following estimate supports these conclusions. The inelastic collision rate should be a capture rate between Rydberg atoms multiplied by a probability of energy transfer among the atoms. We estimate the capture rate as $\eta v \sigma$, where $\sigma = \pi R_0^2$, $C_6 R_0^{-6} = kT$, and ηv is the Rydberg atom flux. We then deduce a capture rate of

$$\eta v \sigma = \eta v \pi \left(C_6/kT\right)^{1/3} \sim 200/s \tag{5.1}$$

for an $n = 43$ density of $\eta = 10^7/\mathrm{cm}^3$. This rate, already small, is further reduced by the energy transfer probability. For states like 43D, where the van der Waals interactions are repulsive at long range, there are no thermally accessible curve crossings and we expect the rate to be suppressed by at least a Boltzmann factor $e^{-\Delta E/kT}$, which even for 43D with small ΔE is a factor of $\sim 10^{-2}$.

Since the atoms are only rarely leaving the trap due to Rydberg-Rydberg collision or ionization, they must primarily return to the ground state by emission of one or more photons. In the next section we introduce a direct probe of the Rydberg state population that will give more information about the details of this process.

5.3 Cascade Fluorescence

As a complementary diagnostic to trap loss observations, we use a photon counting module and a narrowband interference filter to detect the 420 nm decay photons from the $6P_{3/2}$ state to the $5S_{1/2}$ ground state. These photons are only observed coming from

the MOT cloud under conditions of Rydberg excitation. The fluorescent branching ratio to the $6P_{3/2}$ from a high nS or nD Rydberg state is calculated to be about $b_{6P} = 0.15$, varying only slightly with principal quantum number. In order to make sense of these count rates we must determine how many counts per second we would expect given an equilibrium population of Rydberg atoms N_r. The decay rate $A_{n'l',nl}$ from a Rydberg state $|nl\rangle$ to a lower lying state $|n'l'\rangle$ varies with the average oscillator strength $\overline{f}$ as follows [Gallagher, 1994]:

$$A_{n'l',nl} = \frac{-2e^2\omega^2_{n'l',nl}}{mc^3}\overline{f}_{n'l',nl}. \tag{5.2}$$

Here, the average oscillator strength is also frequency dependent and goes as,

$$\overline{f}_{n'l',nl} = \frac{2}{3}\omega_{n'l',nl}\frac{l_>}{2l+1}|\langle n'l'|\, r\, |nl\rangle|^2, \tag{5.3}$$

where $l_>$ is the greater of l and l'. Plugging Eq. 5.3 into 5.2 gives an ω^{-3} dependence of the oscillator strength on the frequency of the radiated photon. Transitions to energy levels of the lowest principal quantum numbers will have the highest frequencies, and because of this ω^{-3} dependence, these transitions are favored despite the smaller value of the matrix element $|\langle n'l'|\, r\, |nl\rangle|^2$ associated with them. This matrix element, or rather the reduced matrix element associated with it, must in general be calculated numerically, and is simply equal to the radial integral $(\int P_{n'l'} r P_{nl} dr)^2$.

We calculate the fluorescent branching ratio by comparing the decay rate to the individual states $A_{n'l',nl}$ to the total fluorescent decay rate A_{nl} out of state $|nl\rangle$ to all lower-lying levels. The total rate will be $A_{nl} = 1/\tau_{nl}$ where τ_{nl} is the lifetime of the state $|nl\rangle$. The lifetime of state $|nl\rangle$ is given by,

$$\tau_{nl} = \tau_0(n - \delta_{lj})^\alpha, \tag{5.4}$$

where n is the principal quantum number, δ_{lj} is the quantum defect of the state $|nlj\rangle$ as calculated by [Li *et al.*, 2003] and [Han *et al.*, 2006], and τ_0 and α are parameters dependent upon atomic species and angular momentum state, as detailed in [Gallagher, 1994]. The branching ratio $b_{n'l'}$ for the radiative transition $|nl\rangle \rightarrow |n'l'\rangle$ is then,

$$b_{n'l'} = \frac{A_{n'l',nl}}{A_{nl}}. \tag{5.5}$$

Now we would like to look more closely at the radiative decay of these Rydberg atoms to lower-lying states, using the 28D state as an example. We calculate that $b_{6P} = 16\%$ of the atoms that spontaneously decay out of the $28D_{5/2}$ state go to the $6P_{3/2}$ state, with $b_{5P} = 64\%$ going to the $5P_{3/2}$ state. A much smaller fraction of the atoms will decay to a higher P or F state (e.g. 6% to the $7P_{3/2}$), but these atoms must then make *two* transitions to the $6P_{3/2}$ state. The probability of multiple photon cascade into the $6P_{3/2}$ state is small because the long-wavelength photons required are disfavored. P and F Rydberg states predominantly cascade into 5S, 6S, and 4D levels, all of which lie energetically below the 6P state. Even for states slightly above the 6P, such as the 5D, the predominant decay channel is to states below the 6P. Thus the cascade fluorescence is likely a reliable probe of the S or D Rydberg state populations, and is relatively insensitive to P or F Rydberg states.

The result is that only atoms that decay directly to the $6P$ state contribute appreciably to the observed count rate on the photon counters. It is also worth noting that we are sensitive to the decay of the $6P_{1/2}$ to ground state at 421.67 nm, however, since we excite to the J=5/2 Rydberg level the decay to this state is forbidden by dipole selection rules. Photons from all other radiative transitions are blocked by the bandpass filters in the path of the photon counting modules.

We now wish to calculate the rate of expected photon counts per second for a given number of Rydberg atoms and compare this rate with our observed cascade signal. The $28D$ Rydberg state decays at a rate of $A_r = 4.1{\times}10^4$ s^{-1}, however blackbody radiation emitted from the room-temperature walls of the vacuum chamber will also transfer atoms out of the Rydberg state at a rate of [Gallagher, 1994],

$$A_{BB} = \frac{4\alpha^3 kT}{3n^2}, \tag{5.6}$$

where $\alpha = 1/137$ is the fine structure constant, T is the temperature of the blackbody emitter, and n is the principal quantum number of the Rydberg level. This blackbody transfer rate is comparable to the rate of radiative decay ($A_{BB} = 2.6{\times}10^4$ s^{-1} for the $28D$ state), and so we must factor in to our calculation the fraction of the total calculated transfer rate due to radiative decay as $A_r/(A_r + A_{BB})$. These states populated by blackbody transfer are assumed, by the argument above, not to result in detected cascade photons. Accounting for the finite collection solid angle $\Theta/4\pi = 3 \times 10^{-3}$, $\eta = 3.4$ % detection efficiency of the photomultiplier tube, and a calculated $6\mathrm{P}_{3/2}$–$5\mathrm{S}_{1/2}$ emission branching ratio $b_{5S} = 0.31$ we expect to observe a cascade count rate

$$c_6 = R_2 N_g b_{6P} b_{5S} \eta \frac{\Theta}{4\pi} \frac{A_r}{A_r + A_{BB}} = 18,000/\mathrm{s} \tag{5.7}$$

at the peak of the 28D excitation resonance. For the data seen in Fig. 4.1 we observe 10000/s, only 55% of the expected count rate. This suggests that roughly 1/2 of the Rydberg atoms are being transferred out of the excitation state by some other process. The ratio of expected to detected cascade counts for the other excitation states (30S, 43D, and 58D) are (0.5, 0.6, 0.6). Again, by the arguments from the previous section, the explanation for this cannot be inelastic Rydberg-Rydberg collisions, which would either produce an extremely large trap loss rate in contradiction to observations, or would necessarily vary greatly with principal quantum number.

5.4 Stimulated Emission Probe

For dipole blockade applications, one is particularly interested in the evolution of the blockaded Rydberg state. Furthermore, in the particular applications of dipole blockade to single-atom and single-photon sources[Saffman and Walker, 2002], stimulated emission is used to couple the blockaded Rydberg level to an intermediate atomic level. As we will see in Chapter 7, it is the decay of this intermediate atomic level that will provide the single-photon source. Thus it is natural for us to pursue the development of a stimulated emission probe of Rydberg dynamics. The intensity dependence of the signals produced by the stimulated emission probe allows further information to be obtained about the population dynamics. Such a probe is non-destructive in the sense that it does not give atoms enough energy to escape the MOT, and has inherently high spectral resolution as compared to field ionization with an MCP. While being less general and less sensitive than field ionization, it does have the potential to be applied to a number of different states, subject to dipole selection rules.

As shown in Fig. 2.3, we apply a tunable diode laser in the range of 1013 to 1027 nm to perform stimulated emission probing of the Rydberg states produced by the two-photon excitation. This "state probe" de-excites atoms from the Rydberg states to the $6P_{3/2}$ state, which subsequently decays via a 420 nm photon to the 5S ground state with a branching ratio of 31%. The $6P_{3/2}$ state is either detected in the same manner as the cascade light mentioned above, or by a reduction in trap loss (explained below). As with the excitation lasers, the spatial size of the state-probe laser is comparable to the MOT cloud size. We deliver nearly 100 mW of light to the atoms, corresponding to stimulated emission rates from 5×10^5 to 5×10^6/s depending upon the Rydberg level involved. The natural decay rate of the $6P_{3/2}$ level of 9.2×10^6/s is fast enough that population cannot accumulate there.

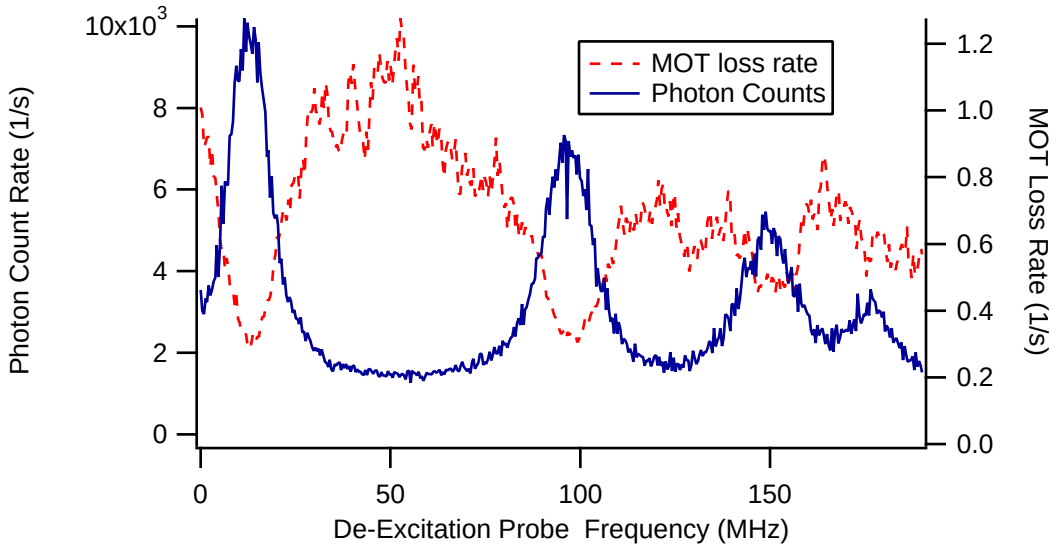

Fig. 5.1: Observed trap loss (dashed line) and photon count rate (solid line) as a function of stimulated emission probe frequency across the 28D-6P$_{3/2}$ manifold. The background cascade count rate is around 1000/s. The decreased trap loss rates which are coincident with 6P-hyperfine-manifold resonances imply that the atoms spend a reduced time in the Rydberg state when the probe beam is on resonance with the 6P state.

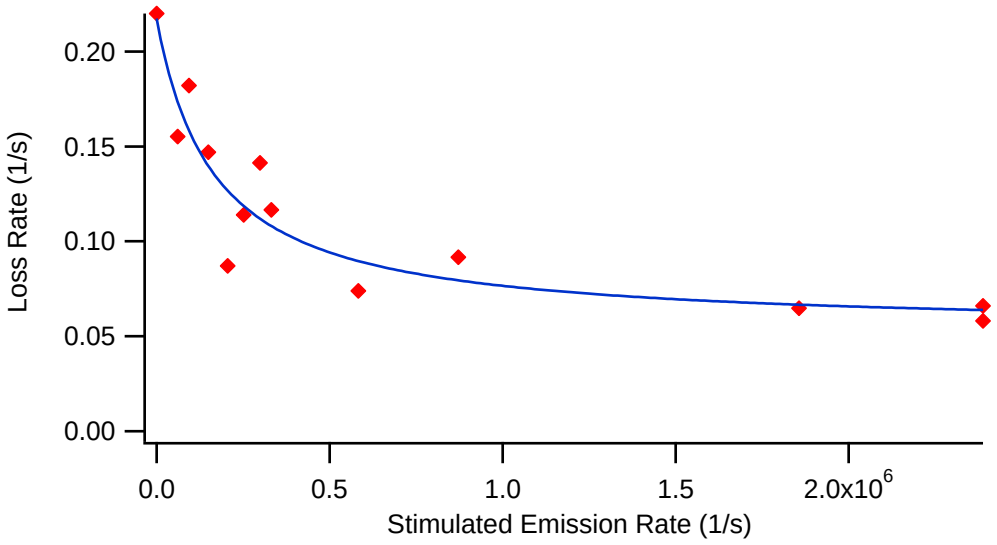

Fig. 5.2: Loss rate dependence on stimulated emission probe intensity for the 28D state, showing short residence times for the Rydberg state produced by two-photon excitation. High probe intensities cause a reduction in the trap loss rate. The line is a fit to Eq. 5.12 as explained in Section 5.5. For this data $\gamma = 1.3 \pm 0.7 \times 10^5/s$.

When the stimulated emission probe is on resonance, atoms are returned to the ground state more quickly than they would otherwise spontaneously radiate from the long-lived Rydberg levels. This reduces the loss rate from the trap as the Rydberg atoms do not stay excited long enough for loss mechanisms such as blackbody ionization and inelastic collisions to remove many of them from the trap. Keeping the excitation beams on resonance with the two-photon excitation, we can scan the frequency of the stimulated emission probe to observe the $6P_{3/2}$ hyperfine manifold. Such a scan is shown in Fig. 5.1. When tuned on resonance with the $6P_{3/2}$ F=3 hyperfine state, the MOT loss rate is reduced from 0.8/s to 0.2/s, with the amount of reduction depending on probe intensity.

Now we wish to examine the dependence of the trap loss rate on this probe intensity. An example of this for the $28D_{5/2}$ Rydberg state is shown in Fig. 5.2. The figure

clearly demonstrates that by using a sufficiently high state-probe intensity the atoms can be returned to the ground state before ionization or inelastic collisions can occur, thus reducing the loss rate of the MOT. The surprising feature of the data is that much higher intensities are needed than would be expected if the dominant population transfer from the Rydberg level were spontaneous decay or blackbody transfer (rates of 4×10^4/s and 2×10^4/s, respectively). In fact, the population transfer rate from the Rydberg state in Fig. 5.2 is about 1.3×10^5/s, implying a Rydberg lifetime of 7 μs.

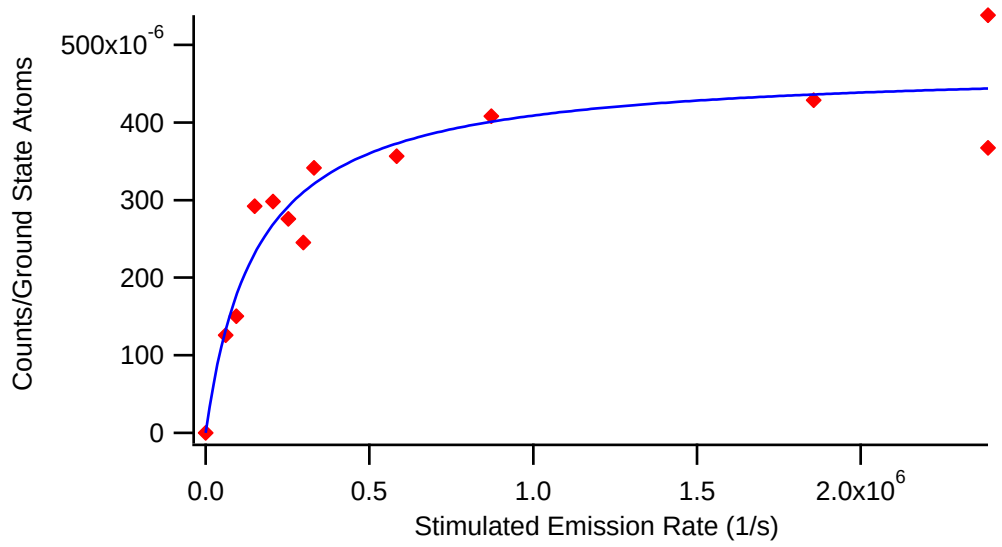

Fig. 5.3: Dependence of $6P_{3/2}$ decay counts on stimulated emission probe intensity for the 28D state. The line is a fit to Eq. 5.13 as explained in Section 5.5. For this data $\gamma = 1.2 \pm 0.4 \times 10^5/s$, which is in close agreement with the result in Fig. 5.2 and serves as a check on the consistency of the model.

Alternatively, we can measure the state probe laser effects by detecting the number of $6P_{3/2}$ decay photons from stimulated emission from the Rydberg state. The count rate data, scaled by the number of ground state MOT atoms, is shown in Fig. 5.3 for the 28D state. The cascade and background signal have been subtracted for this data, thus there are no counts when the stimulated emission rate is zero. As with the

trap-loss-reduction data of Fig. 5.2, the counts saturate at a stimulated emission rate of around 2×10^5/s, as measured by the 1/e rate, which implies that the other rates out of the excitation state must be on this order.

From the trap loss or state probe data, the residence time of the Rydberg state varies from about 10 μs at $n = 28$ to about 50 μs at $n = 58$. Thus the population is being transferred out of the initial Rydberg state faster than can be accounted for by spontaneous decay and blackbody transfer (decay times of 25 μs and 50 μs at $n = 28$, respectively). The transfer times increase with n, just the opposite dependence as would be expected for energy transfer collisions between Rydberg states. These would be expected to decrease with n due to rapid increase in van der Waals interaction strengths. This counter trend thus implies that Rydberg-Rydberg collisions are not the process responsible for the fast transfer out of the initial Rydberg state.

Interestingly, the 30S state has the highest transfer rate to other Rydberg states. This again implies that atom-atom interactions do not dominate the process, as the strengths of van der Waals interactions tend to be larger for D states than for S states, as noted in Chapter 4.

We have checked that the transfer rates increase with increasing excitation rate; Fig. 5.4 demonstrates this for the $28D$ state transfer rate. This confirms that some transfer process besides blackbody radiation is occurring since the excitation rate will increase the equilibrium population of Rydberg atoms and there should be no dependence of the blackbody transfer rate on Rydberg atom population.

As can be seen from Fig. 5.2, there is a non-zero loss rate at high probe intensities where the stimulated emission laser should fully deplete the original excitation state. There are several possible explanations for this. If there were a loss mechanism that was being enhanced by the state-probe laser, this would produce such a behavior. However, processes such as photoionization caused by the state-probe laser or light-induced 6P-5S

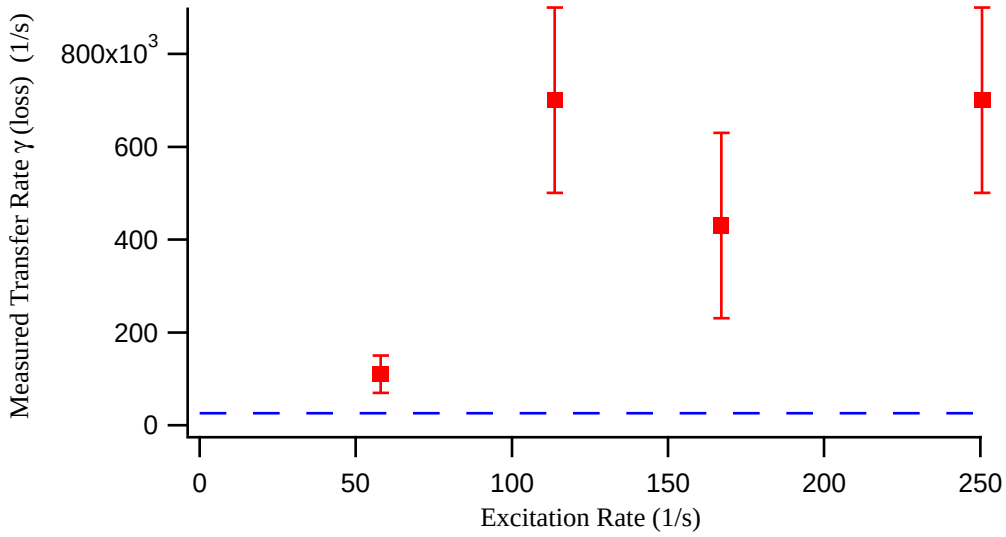

Fig. 5.4: Dependence of the measured Rydberg state transfer rate, γ(loss), on the excitation rate for the $28D$ state. The increase of the transfer rate with increasing excitation rate suggests that blackbody transfer is not the cause of the state transfer out of the excitation Rydberg state. The dotted line represents the rate of transfer due to blackbody radiation (2.6×10^4 s^{-1}), which should be the transfer rate in the limit of small Rydberg populations.

collisions can be estimated to be far too weak to account for this effect.

Another possibility has to do with Zeeman precession in the nd states causing population to accumulate in inaccessible magnetic sublevels. The magnetic field gradient used to confine the MOT atoms sets up a magnetic field of 1 G at the edges of the MOT, enough that precession between magnetic sublevels of the Rydberg atoms at the edges of the MOT occurs at a rate of several MHz, which is on the order of the stimulated emission rate. This rate of precession can be estimated by considering the strength of the Zeeman shift on the atoms of 2.8 MHz/Gauss. The rate of precession ω_B for a particular atom is then proportional to the magnetic field strength at the position of the atom multiplied by the Zeeman energy level shift. This means that for atoms on

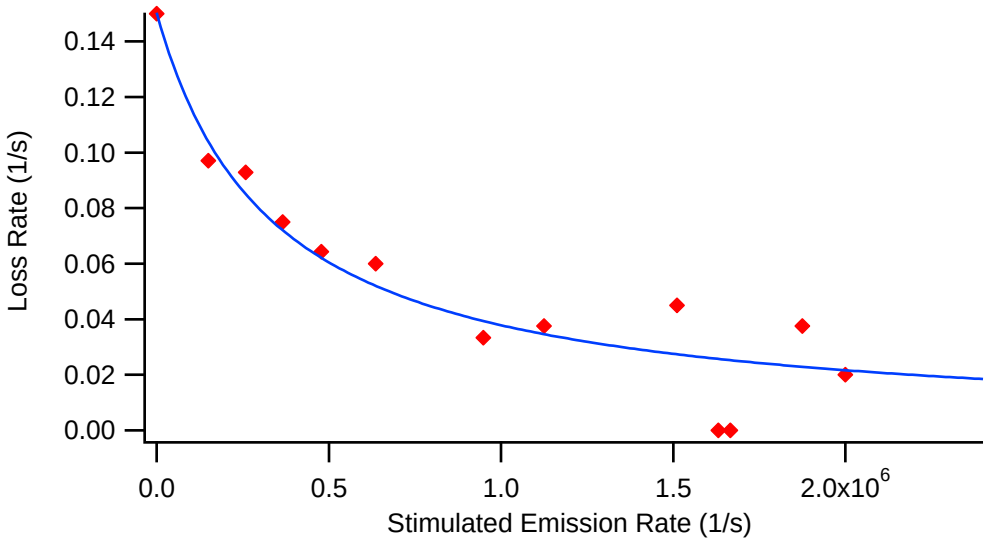

Fig. 5.5: Loss rate dependence on stimulated emission probe intensity for the 28D state, with the MOT magnetic field switched off during excitation. The line is a fit to Eq. 5.12 as explained in Section 5.5. The data imply that the loss rate goes to zero at high probe intensities under these conditions.

the edge of the MOT, $\omega_b \sim 1$ G $\times 2\pi \times (2.8 \times 10^6$ MHz/G$) = 1.8 \times 10^7$ s^{-1}. The result of this precession is that a fraction of the atoms - up to 1/3 - move to a state that is inaccessible to the state-probe laser because of the dipole selection rules determined by the polarization of the state-probe laser. Linearly polarized state-probe light, for example, cannot transfer $m_J = \pm 5/2$ Zeeman levels from an $nD_{5/2}$ Rydberg state to the $6P_{3/2}$ state. This is because the $6P_{3/2}$ state contains only $m_J = \pm 3/2, \pm 1/2$ states and dipole selection rules require that $\Delta m_J = 0$ for transitions induced by linearly polarized light. Thus population that accumulates in these levels cannot be de-excited by the state-probe laser.

This effect was verified by repeating the experiment with the MOT magnetic field being switched off for 10 ms intervals and only switching on the Rydberg excitation lasers during the times the field was off. This data, shown in Fig. 5.5 for $n = 28$ shows that Rydberg populations at high state probe intensities are markedly reduced as compared to when the magnetic field is on. The reduced signal-to-noise for this experiment made it possible to do this only for $n = 28$.

5.5 Model of Rydberg Population Dynamics

In the previous sections, we have described the basic processes that are evidently at work under the conditions of our experiment, and their experimental signatures. To further analyze the results, we present here a simplified model of the Rydberg dynamics and use it to extract the values of a few simple parameters from the data. Confirming the interpretation in the previous section, we find that some process that does not cause trap loss nevertheless transfers population out of the excitation Rydberg state on a time scale short compared to spontaneous or blackbody lifetimes. The lengthening of this time scale with increasing principal quantum number leads us to believe that it

is not inelastic collisions between Rydberg atoms.

The processes included in the model are illustrated in Fig. 5.6. We describe the system with a three state model: A ground state $|g\rangle$ with N_g atoms, the excitation Rydberg state $|r\rangle$ with N_r atoms, and an additional effective Rydberg state $|s\rangle$ that accounts for other states that are populated from state $|r\rangle$.

The dynamics of the excitation state $|r\rangle$ depend on laser excitation and de-excitation, spontaneous and blackbody radiation, and transfer to the other Rydberg states $|s\rangle$. Population enters $|r\rangle$ by excitation from the ground state at a rate $R_2 N_g$ where R_2 is the effective excitation rate calculated as described in Chapter 4. Spontaneous decay to low-lying levels occurs at a rate $A_r N_r$. Blackbody radiation and other potential processes that transfer atoms to other Rydberg states occur at a rate γN_r. There is also the possibility of trap loss (through ionization, for example) at a rate Γ_r directly from state $|r\rangle$. Finally, de-excitation from the state-probe laser occurs at a rate $R_3 N_r$. Thus

$$\frac{dN_r}{dt} = R_2 N_g - A_r N_r - R_3 N_r - \gamma N_r - \Gamma_r N_r \tag{5.8}$$

is the rate equation for the excitation state population.

The other Rydberg states are produced by collisional or radiative transfer from state $|r\rangle$ at the rate γN_r and have an effective radiative lifetime A_s. If an atom in one of these Rydberg states represented by the state $|s\rangle$ is transferred to a different Rydberg state (also represented by $|s\rangle$), for the purposes of the model this atom will have remained in state $|s\rangle$. We also assume that these states can cause trap loss at a rate Γ_s due to blackbody ionization and other collisional processes. Thus they obey

$$\frac{dN_s}{dt} = \gamma N_r - \Gamma_s N_s - A_s N_s \tag{5.9}$$

We are assuming that transfer from $|s\rangle$ back to $|r\rangle$ is unlikely.

In addition to the radiative de-excitation and excitation processes with the Rydberg

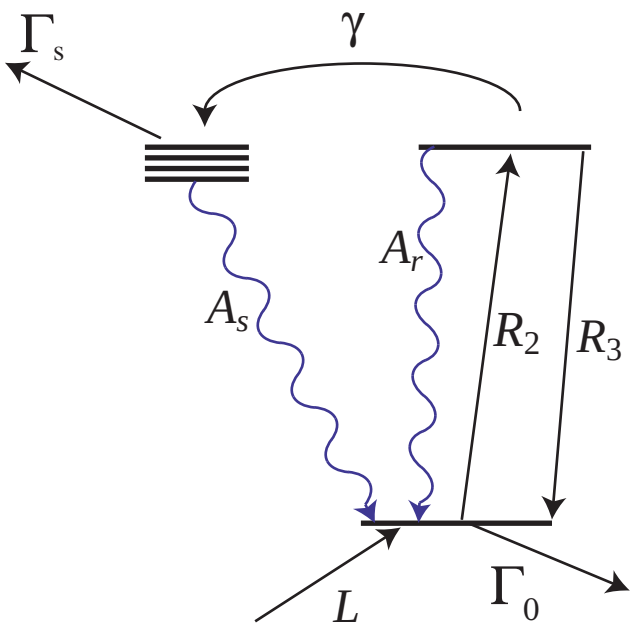

Fig. 5.6: Diagram of the simplified model of Rydberg population dynamics.

levels, the ground state population N_g is affected by MOT loading (L) and loss (Γ_0) processes (as discussed in Chapter 4) that we assume are not materially changed when the Rydberg excitation lasers are on. The resulting rate equation for the ground state population is

$$\frac{dN_g}{dt} = L - \Gamma_0 N_g - R_2 N_g + (A_r + R_3) N_r + A_s N_s. \tag{5.10}$$

We now wish to determine the loss rate Γ from this model in order to compare with our experimental observations. Since the Rydberg populations adiabatically follow the slowly-varying ground-state population, we may plug in the steady-state solutions to Eqs. 5.8 and 5.9 to get

$$\frac{dN_g}{dt} = L - \Gamma_0 N_g - \Gamma N_g. \tag{5.11}$$

The loss-rate from the trap is increased by an amount

$$\Gamma \approx \frac{R_2 \gamma}{A_r + R_3 + \gamma} \left[\frac{\Gamma_s}{A_s} + \frac{\Gamma_r}{\gamma} \right], \tag{5.12}$$

where the $\approx$ sign is due to the assumption that all of the atoms that decay from the $|s\rangle$ state will eventually return to the trap. Since our observed trap loss rates are much smaller than our excitation rates, this is a decent approximation. The loss rate here is a product of two factors. The first essentially measures the excitation rate of Rydberg atoms, modified by the de-excitation due to the state-probe laser. The second factor is the probability that the excited Rydberg atoms experience trap loss as opposed to radiatively decaying back to the ground state.

The model similarly predicts the count rate of 420 nm photons produced by the state-probe laser:

$$\frac{I_3}{N_g} = \frac{R_3 R_2 \Theta \eta b_{6P} b_{5S}/4\pi}{A_r + R_3 + \gamma} \tag{5.13}$$

Thus the state-probe-induced 420 nm count rate can also be used to determine the transfer rate γ, with the data and fit for 28D shown in Fig. 5.3.

The results of fitting our experimental data to this model are summarized in Table 5.1. We list there the deduced values of the primary unknowns γ and Γ_s, as well as the assumed values for the input parameters A_r and A_s. The calculation of A_r is straight-forward, however we must assume something about the distribution of atoms in our other Rydberg states $|s\rangle$ to produce a value for A_s. As we will discuss in the next chapter, one of these states $|s\rangle$ will be the dominant decay channel for the Rydberg atoms in state $|r\rangle$ and it is this state for which we calculate the radiative decay rate A_s. Thus for 28D this state is 27P, and for 30S this is 29P. We note that both trap loss and 420 nm count rates can be used to extract γ, an important internal consistency check. In fact, the two methods for determining γ agree quite well, which bolsters the credibility of the model. The primary results then are these:

- The atoms transfer out of the excitation Rydberg state at a rate γ that is substantially faster than spontaneous decay or blackbody transfer rates.

- The mechanism for population transfer, to an excellent approximation, does not cause trap loss.

- The population transfer rate decreases slowly with increasing principal quantum number, as opposed to the expected rapid increase if near-resonant energy transfer collisions were the relevant mechanism.

- The probability of trap loss is very small; most Rydberg excitations result in radiative repopulation of the ground state without trap loss.

These conclusions from fitting the experimental data to the model are consistent with the simplified analyses presented in Sections 5.2–5.4. In the next chapter we will discuss their implications.

Tab. 5.1: A summary of transfer rate data using both count rate and loss rate methods. As a basis for comparison, the blackbody transfer rate A_{BB}, spontaneous emission rate A_r, the estimated mean spontaneous emission rate A_s from other Rydberg states, and the inferred trap loss rate Γ_s are also included. All rates are in units of s^{-1}.

State	γ(counts)	γ(loss)	A_{BB}	A_r	A_s	Γ_s
28D	1.2×10^5	1.3×10^5	2.6×10^4	4.1×10^4	3.1×10^4	265
43D	7.4×10^4	7.2×10^4	1.1×10^4	1.1×10^4	2.0×10^4	602
58D	2.6×10^4	2.0×10^4	6.1×10^3	4.8×10^3	7.4×10^3	433
30S	3.9×10^5	5.0×10^5	2.3×10^4	4.4×10^4	3.3×10^4	83

6. SUPERRADIANCE

6.1 Introduction

In this chapter, we propose that superradiant decay from the excitation Rydberg state is responsible for the observed transfer rates recorded in the previous chapter. We develop a simple model for superradiance based on the work of Gross and Haroche [Gross and Haroche, 1982] which allows us to modify our state equations from the previous chapter to include superradiant effects. In addition, we calculate a cooperativity parameter which describes the fraction of atoms in the sample that will participate in the collective emission from the excitation state. The calculated transfer rates that our model predicts are within a factor of 3 of the measured state transfer rates from the previous chapter, strongly suggesting that superradiance is the main factor in these transfer rates. In addition, we find that only the superradiant mechanism correctly predicts the n- and l-level dependence of the measured Rydberg transfer rates. Finally, we proffer blackbody ionization as the cause of the observed trap loss and demonstrate that the measured trap loss rates agree well with the blackbody ionization rates for the Rydberg levels involved in our experiment.

6.2 Superradiant Population Transfer

We have argued in the previous chapter that the transfer mechanism responsible for population transfer out of the excitation state in a few microseconds cannot be due to

near-resonant energy transfer collisions between excited Rydberg atoms. L-changing collisions between Rydberg atoms and free electrons are another possible mechanism. Such collisions are unlikely to be energetic enough for the recoil to eject atoms from the trap and so would agree with much of the observed behavior. However, at our low excitation rates it is unlikely that electrons are present in sufficient quantities to cause the observed state transfer. With blackbody ionization rates of 400/s (see Section 6.3) acting on a population of 10^4 Rydberg atoms, free electrons are produced at a rate of 4×10^6/s. Free electrons are typically fast-moving and dissipate at a rate of $\sim10^4$/s [Killian *et al.*, 1999], giving an average free electron population of ∼400, which would not have a large impact on the 10^4 atoms in the excitation state. We estimate that there is insufficient ionization to cause an electron trap [Killian *et al.*, 1999]. In addition, the rate of l-changing collisions should increase with principal quantum number, in contrast with our observations.

Having argued against collisional phenomena being responsible for Rydberg energy transfer, we need a radiative mechanism to explain our results. Recently, Wang *et al.* [Wang *et al.*, 2007] observed superradiance in the measured lifetimes of Rydberg states. That superradiance could play an important role in Rydberg population dynamics can be understood by the following arguments. For principal quantum numbers > 20, the size of the MOT is less than the wavelength for radiative emission from the excitation state to nearby dipole-allowed states. If there are N atoms initially in a particular Rydberg state, the collective dipole moment is enhanced by a factor of N (assuming the atom cloud is much smaller than the wavelength of the emitted light). The emission rate is enhanced by a factor of N^2, or by a factor of N on a per-atom basis. Since N is on the order of 10^4 for our experiment, the superradiant decay rate will be on the

order of

$$\frac{2}{3}\frac{\omega^3 N d^2}{\hbar c^3} \sim \frac{4N}{3n^5}\alpha^3\frac{Ry}{\hbar} \tag{6.1}$$

which is 3×10^5/s for 10^4 $n = 50$ Rydberg atoms. The low emission frequency is compensated for by the large number of cooperatively radiating atoms. The strong n^{-5} dependence of superradiance suggested by Eq. 6.1 should be compared to the n^{-3} dependence of spontaneous decay rates. Furthermore, as described below, spatial coherence effects further alter the n-dependence of Eq. 6.1 so that the relative importance of superradiance and spontaneous decay remain fairly constant for the levels studied in this experiment.

Wang *et al.*, [Wang *et al.*, 2007] developed a sophisticated theory of superradiance with application to cold Rydberg gases. Here we present a simplified model of superradiance to use as a interpretive guide. We base this model on Dicke's original work [Dicke, 1954] as elucidated by Gross and Haroche [Gross and Haroche, 1982] and Rehler and Eberly [Rehler and Eberly, 1971].

In considering the superradiant decay of an initial state $|e\rangle$ to a lower energy state $|l\rangle$, the Dicke approach introduces an effective collective spin state of the 2N-level system as $|JM\rangle$, with $N_e = J + M$ atoms in state $|e\rangle$ and $N_l = J - M$ atoms in state $|l\rangle$. The radiation rate is determined by calculating the expectation value of a lowering operator to the $|JM\rangle$ state, as in equation (2.13) in Gross and Haroche's paper. The radiation rate is found to be $\Gamma_{el}(J(J+1) - M(M-1)) = \Gamma_{el}N_e(N_l+1)$ by application. To extend the two-level case to our multi-level case, we assume that we can model superradiance with a set of rate equations

$$\frac{dN_e}{dt} = -\sum_{l<e}\Gamma_{el}N_e(N_l+1) + \sum_{l'>e}\Gamma_{l'e}N_{l'}(N_e+1) \tag{6.2}$$

where again the transition is from $|e\rangle \rightarrow |l\rangle$. This model reproduces the key features of superradiance: a large initial inversion radiates at Γ_{el} (per atom) at first, then as the

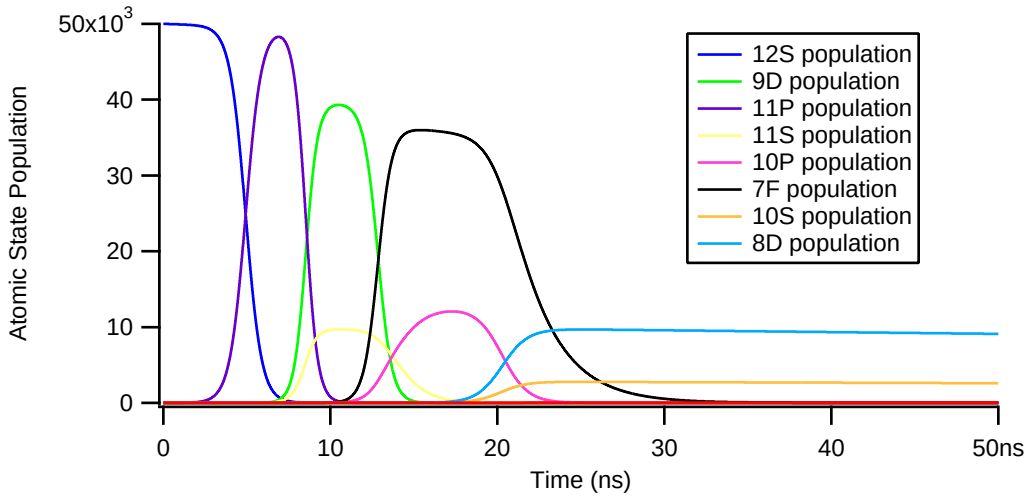

Fig. 6.1: Model simulation of the experiment by Gounand *et al.*, [Gounand *et al.*, 1979]. In the experiment, Rb atoms were excited to the $12S$ Rydberg level and superradiant cascade to lower levels was observed. Our model predicts superradiant population transfer on timescales similar to Fig. 2 in the reference.

inversion is reduced the rate accelerates to a maximum of $N\Gamma_{el}/4$, occurring over a time $(\ln N)/(\Gamma_{el}N) \ll 1/\Gamma_{el}$ [Rehler and Eberly, 1971]. As an additional check on the model, we have simulated the experiment of Ref. [Gounand *et al.*, 1979] (which was performed at high temperatures and much smaller n) and our model reproduces the dominant features of the data shown there, as seen in Fig. 6.1. The Gounand *et al.*, experiment involved excitation of Rb atoms to the $12S$ state. Although the model predictions are slightly amiss regarding the relative magnitude of the atomic populations seen in Fig. 2 of the reference, it does correctly predict superradiant population transfer from $12S \rightarrow 11P$ after 5 ns and subsequent transfer from $11P \rightarrow 9D$ 10 ns after excitation to the $12S$ state. Since the superradiant transfer rate is the important issue here, it is encouraging that the model so closely matches this experiment.

The emission rates Γ_{el} are the rates for spontaneous emission multiplied by a coop-

erativity parameter C_{el}:

$$\Gamma_{el} = C_{el}\frac{2e^2\omega_{el}^3}{mc^3}\frac{(2J_l+1)}{(2J_e+1)}f_{el} \tag{6.3}$$

where the f_{el} are the calculated absorption oscillator strengths. For a system of atoms whose spatial extent is on the order of the wavelength of the transition, superradiance will occur at a reduced rate. The wavelength of the transition to the nearest lower lying Rydberg state varies from 0.17 cm for 30S-29P to 2.8 cm for the 58D-59P transition. For low n, this is quite close to the 1 mm spatial extent of the MOT, and lower levels will have even shorter transition wavelengths. Obviously, some factor is needed to account for the degree to which the atoms emit cooperatively. Following Ref. [Rehler and Eberly, 1971], the cooperativity parameter for a uniform density system of N atoms in a volume V radiating in direction $\hat{k}$ is (in the $N \gg 1$ limit)

$$C_{el} = \frac{1}{V^2}\int d^3x \int d^3x'\, e^{i(\vec{k}-\vec{k}_1)\cdot(\vec{x}-\vec{x}')} \tag{6.4}$$

$$= \frac{9(\sin(k_{el}R) - k_{el}R\cos(k_{el}R))^2}{(k_{el}R)^6}, \tag{6.5}$$

for a spherical uniform density cloud, where kR is the product of the wavenumber and the radius of the atomic sample. The cooperativity parameter is 1 for $R \ll \lambda$ and decreases to 0 for $R \gg \lambda$. In practice, the cooperativity parameter becomes small around $n = 20$ for a 1 mm MOT, which would imply that the effects of superradiance are not significant for Rydberg atoms with a smaller principal quantum number than 20. Figure 6.2 shows how the cooperativity parameter C_{el} varies with the transition wavelength for atoms in the MOT.

To account for superradiance, we replace the level $|s\rangle$ of the model of Section 5.5 with a set of levels near in energy to $|r\rangle$ that are coupled to each other and to $|r\rangle$ by superradiance (Eq. 6.2) and blackbody radiation. We find steady-state solutions of the resulting non-linear equations and from them deduce the effective Rydberg-Rydberg transfer rate from Eq. 6.2 with $e = r$. In solving these equations we wish to include

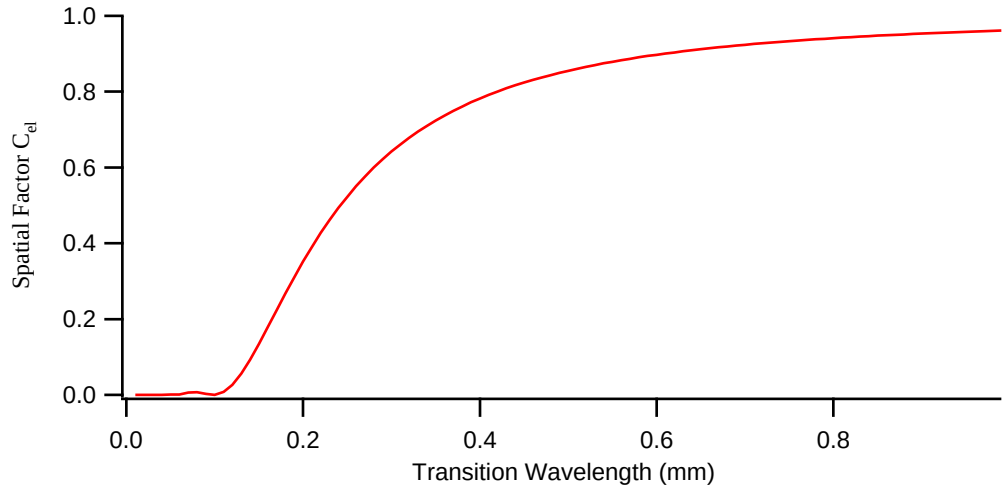

Fig. 6.2: Variation of the cooperativity parameter with wavelength. The parameter is effectively zero for wavelengths much smaller than the MOT size, and unity for wavelengths much greater.

all energy levels relevant to the decay of the excitation Rydberg state. However, there are a great many energy levels below the excitation state, so we must use a smaller set of states to avoid cumbersome calculations. Instead of including all energy levels then, we start by including the excitation state and the lower lying states that are closest in energy to the excitation state. We may then solve the equations to find the calculated transfer rate with this set of states and then repeat the process with additional lower-lying states included. We continue adding lower-lying states until the addition of energy levels does not affect the calculated transfer rate out of the excitation Rydberg state. For this calculation, eight energy levels were sufficient to calculate the transfer rate out of the excitation state, the inclusion of additional lower-lying states did not affect the calculation.

To note another assumption of importance, we must consider the effects of blackbody state transfer in the superradiance model. Blackbody radiation at centimeter wavelengths will have essentially a constant number of photons per unit frequency, so

the blackbody transfer rate between individual states will depend only upon the average oscillator strength between the states. The oscillator strength falls rapidly with increasing transition energy, so the most important states for blackbody transfer are the four states nearest to the excitation Rydberg D-state. These states are the P- and F-states just above and just below the D-state in energy (for S-state excitation, there would be only two relevant states, the nearby P-states). Following the same process as before, we begin by calculating the blackbody transfer rate to each of the nearby states. For the D-states, the rate to the four nearby states accounts for some 80% of the total blackbody transfer rate A_{BB} as calculated in Chapter 5, and the inclusion of additional states for blackbody transfer does not affect the calculated superradiant transfer rate out of the excitation Rydberg state. Thus, as a simplifying approximation, we divide the total blackbody transfer rate A_{BB} by 5, and have an equal portion (20%) of the blackbody rate going to each of the four nearby states.

Table 6.1 compares the observed Rydberg transfer rates and those predicted by our simulation. These rates do not drop off as quickly as would be expected from Equation 6.1. This is a result of the spatial factor approaching unity for the higher n-levels, balancing out the decrease in natural emission rate. Additionally as a result of this increasing spatial factor, our simulation indicates that the atoms are transferred predominantly to f-states for the 43d and 58d levels. This transfer to f-states could explain the higher total loss rate from the trap for these levels. We emphasize that there are no adjustable parameters in our simplified superradiance model, and yet it naturally predicts the order of magnitude of the Rydberg-Rydberg transfer rates. A more sophisticated model would be expected to explain the variation seen.

An example of the effect of this spatial factor on transitions to P- and F-states would be instructive. The energy difference between the D-state Rydberg excitation level with the (n-2)F state is larger than that between the same Rydberg excitation

level and the (n+1)P state, and the transition wavelength is thus shorter. Given that the transition wavelength for the $28D \rightarrow 29P$ transition is 0.27 mm, approaching the size of the MOT, this means that we expect a smaller spatial factor for the $28D \rightarrow 26F$ transition ($\lambda = 0.12$ mm). As a means of comparison, the calculated spatial factor for the $28D \rightarrow 29P$ transition is $C_{el} = 0.577$ and that for the $28D \rightarrow 26F$ is 0.02. The result is that for this Rydberg n-level, the $29P$ state is the preferred decay path of the Rydberg atoms excited to the $28D$ in the model. On the other hand, for the $58D$ state, the $58D \rightarrow 59P$ has a wavelength of $\lambda = 2.77$ mm and thus a spatial factor of 0.994 while the $58D \rightarrow 56F$ transition has a wavelength of 1.21 mm and a spatial factor of 0.971. The similar spatial factors mean that the strong ω^{-3} dependence of the radiative transition rates will lead this F-state to be the dominant decay channel. It is also worth noting that in Dicke's model each decay makes a decay along the same channel more likely. So just as with competing frequency modes in a laser cavity, the channel with the largest branching ratio will have the greatest population accumulation.

The model then suggests that we should have a significant equilibrium population of Rydberg atoms at several energy levels when the excitation lasers are tuned to resonance with the two-photon transition to the Rydberg state. To test this experimentally, we tuned the state-probe laser to the $27D \rightarrow 6P$ transition with the excitation lasers tuned to the $28D$ Rydberg level. If there were a population of over ~ 100 atoms in the $27D$ state (as the model suggests) we should detect an increase in the count rate recorded on the photon counter when the state-probe laser is swept across the $27D \rightarrow 6P$ transition. Unfortunately, no such increase was detected. To see why this might be, consider that the superradiant transition rate is maximized when the population of both the $|e\rangle$ and $|l\rangle$ states are equal. Since the state-probe induced de-excitation rate is much larger than the superradiant transition rate, we will very quickly de-populate the $27D$ state. This will reduce the superradiant transition rate to

the $27D$ state which in turn will reduce the equilibrium population in the state. Thus the state-probe laser is less sensitive to equilibrium Rydberg state populations than one might expect when those populations are produced by superradiant decay from a higher level Rydberg state.

Tab. 6.1: A comparison of Rydberg-Rydberg transfer rates deduced by comparing measurements deduced from the model of Section 5.5 with those predicted by the superradiance model. As noted in the text, the model accounts for radiative lifetimes as well as blackbody-induced l-changing transitions. All units are s^{-1}.

State	γ(calculated)	γ(expt)
28D	1.7×10^5	1.3×10^5
43D	2.4×10^5	7.4×10^4
58D	1.2×10^5	2.0×10^4
30S	2.2×10^5	5.0×10^5

6.3 BlackBody Ionization

So far we have not discussed the actual mechanism for trap loss. The deduced trap loss rates are quite modest, typically 400/s on a per Rydberg atom basis. This is close to what would be expected from blackbody ionization. Blackbody ionization rates were recently calculated in Ref. [Beterov *et al.* (2007)] for the various Rydberg levels. Assuming Rydberg n-level distributions from our superradiance model, we find expected photoionization rates from blackbody radiation to be as shown in Table 6.2. For the D states, there is reasonable agreement between our deduced experimental rates and the predicted values, suggesting that blackbody ionization probably composes a large portion of the total loss from the trap. For the s-state, the predicted trap loss is

greater than observed by about a factor of 3, for which we have no explanation.

Tab. 6.2: Comparison of inferred Rydberg trap loss rates with blackbody ionization rates. Γ_{BBI} is the rate of blackbody ionization for each of these states calculated from Ref. [Beterov *et al.* (2007)]. All rates are in units of s^{-1}.

State	$\Gamma_{s\,calc}$	Γ_{BBI}
28D	212	322
43D	470	720
58D	329	457
30S	77	265

6.4 Discussion

Before the experiment of Wang *et al.*[Wang *et al.*, 2007] the effects of superradiance were not appreciated for the population dynamics of high density ultracold Rydberg atoms. Superradiance can happen on very rapid time scales, especially under strong Rydberg excitation as achieved in a number of previous experiments. In fact, superradiance can easily occur on sub-microsecond time scales. A key consequence of superradiance is that it populates Rydberg states lying energetically below the state being excited by the laser. Indeed, in the experiments of Ref. [Walz-Flannigan *et al.*, 2004] and Ref. [Li *et al.*, 2004], population clearly moves to lower lying Rydberg levels on a fast time scale, consistent with the hypothesis of superradiant transfer.

An additional consequence of fast superradiant population transfer is that it provides a mechanism for rapid population of states of neighboring orbital angular momentum l from the excitation state. Pairs of atoms with $\delta l = \pm 1$ interact at long range via the R^{-3} resonant dipole-dipole interaction, not the usual R^{-6} van der Waals inter-

action. The much stronger collision interactions between these atoms may explain the very rapid time scales for plasma formation in a number of experiments where resonant dipole-dipole interactions were not purposely produced using external fields.

7. FOUR-WAVE MIXING

7.1 Introduction

Four-wave mixing occurs when three oscillating, phase-coherent electric fields are applied to an atomic sample so that the atoms in the sample have dipole moments with phases which cause them to add constructively in a particular direction and destructively in all others. The result is that the atoms radiate a fourth field in this so-called "phase-matched" direction which must not only conserve energy for the four-photon process, but also momentum. If these fields are collinear this process is known as degenerate four-wave mixing, or if, as in this experiment, the fields are in some other configuration, the process is termed non-degenerate. The advantage of non-degenerate four-wave mixing in theory, is that it allows us to couple a small number of photons into a fiber or another experiment where very few background counts are present that would require filtering. In conjunction with a Rydberg-atom dipole blockade, this would allow us to have exactly one atom at a time undergo the four-wave process and thus be an excellent candidate for an on-demand single-photon source.

This chapter will begin with discussion of the setup of the four-wave mixing process and some pertinent details in background subtraction. Following this will be our observation of four-wave mixing using Rydberg states as an intermediate step in the process. I will discuss the alignment of the phase-matched geometry and range of angles of the excitation beams for which we observe phase matching, which is $\delta\Theta = 1.6$ mrad for the

$28D$ state in our geometry. We also measured the spatial extent of the phase-matched beam and found it to be diffraction limited. Following this, I present our model of four-wave mixing which begins with calculating the dipole moments of the atoms in the atomic sample. Using density matrices to model the atomic populations in the four levels, we calculate that the fraction of 420 nm light emitted in the phase-matched direction should increase with increasing number of MOT atoms. This is then verified by the experiment.

We then look at the relative phase matching of the hyperfine levels of the $6P_{3/2}$ state and compare these to the model predictions, which agree well with the experiment. Finally, we demonstrate that by tuning the excitation lasers away from the Rydberg state transition that we may decrease the Rydberg state population and thus increase the fraction of light in the phase-matched direction. Under optimum conditions, we observe 50% of the light emitted in the phase-matched direction.

7.2 Experimental Details

An energy level diagram of the four-wave excitation process is seen in Fig. 7.1a. The directions of the three laser beams for the four-wave geometry are chosen to satisfy phase-matching conditions, as shown in Fig. 7.1b. The figure also display the k-vector labels for the various beams, often in the course of this chapter a laser will be referred to by k-vector rather than wavelength (thus I may write "$\mathbf{k}_1$" rather than "780 nm laser" as before). In principle, a wide variety of possible geometries can be chosen, but this particular one was chosen to give a large angle between $\mathbf{k}_2$ and $\mathbf{k}_3$, allowing for a small spatial overlap volume if desired. (A 90° angle is feasible, giving the smallest possible overlap volume, but is incompatible with our vacuum chamber.) Having a small spatial overlap will be vital to obtaining a full dipole blockade, as it results in a

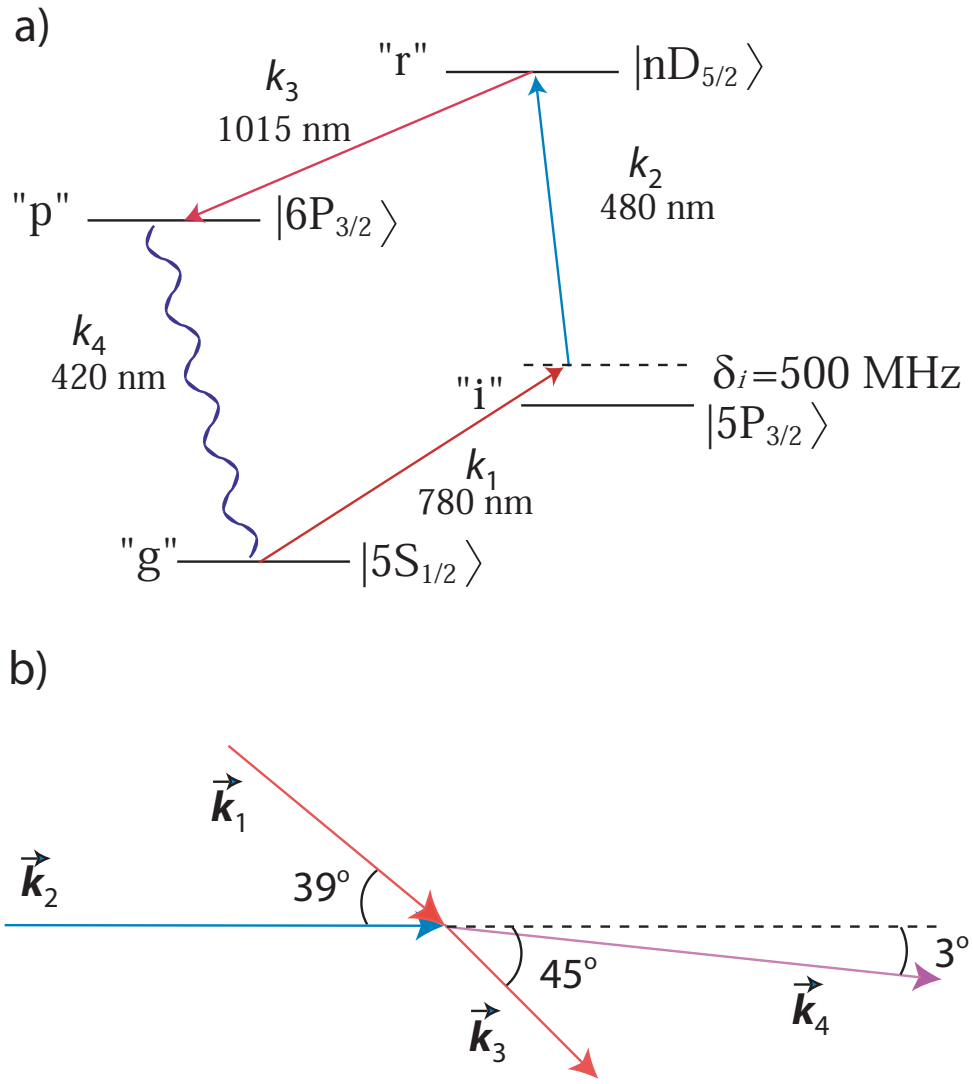

Fig. 7.1: a) Energy levels for four-wave mixing. The k_1 and k_2 photons produce two-photon excitation to an nD Rydberg level. The k_3 laser couples the Rydberg level to the $6P$ state. Atoms in the 6P radiate coherently to the ground state to complete the four-wave-mixing process. b) Phase-matching geometry.

smaller volume over which a large energy-level shift is required.

This geometry results in a phase-matched direction for the exiting 420 nm photons ($\mathbf{k}_4$) which is 3° from $\mathbf{k_2}$. The direction of $\mathbf{k}_4$ is very insensitive to the direction of $\mathbf{k}_1$. One photon counter is placed along an arbitrary or "off-axis" direction, while the other is placed along the anticipated phase-matched or "on-axis" direction. This placement is shown in Fig. 2.2 in Chapter 2. The waists of the three beams for these experiments were $(w_1, w_2, w_3) = (4.0,\ 0.58,\ 0.83)$ mm, comparable to the MOT cloud size of 0.74 mm, so that most of the MOT atoms participate in the four-wave mixing process.

Before proceeding I must mention our data analysis procedure. Any figure in this chapter that displays the dependence of a phase-matched count rate on k_2 must have the raw count rate from the photon counters modified by subtracting the dark count rate as well as the count rate from Rydberg cascade fluorescence as described in Chapter 5. Dark count subtraction is straightforward, however the subtraction of cascade fluorescence requires additional effort. In order to subtract the counts from cascade fluorescence, we first sweep k_2 across the $5P \rightarrow nD$ Rydberg transition with k_3 blocked and record the cascade fluorescence signal on our photon counters. We then fit the count rate from cascade fluorescence to a Lorentzian profile. As long as the intensities of k_1 and k_2 do not change, the cascade fluorescence signal will have the same dependence on k_2 for all frequency sweeps and can be removed from subsequent measurements with k_3 unblocked. This is a small correction, but an important one nonetheless. Also, all phase-matched data presented here were obtained with the MOT trapping lasers switched off. This is because the additional 780 nm laser light from the trapping laser was observed to dephase the four-wave process, thus reducing the phase-matched count rate by a factor of 2.

7.3 Observation of Non-degenerate Four-Wave Mixing

We now turn to the alignment of the four-wave geometry. Phase-matched emission was initially observed for Rydberg principal quantum number $n = 28$ by moving k_1 far off the phase-matched direction and confirming nearly equal k_4 detection rates in the on- and off-axis directions. This is the case since the non-phase-matched light is radiated isotropically, thus any difference in the count rates between the counters here should be a result of differences in detection efficiency. Next, as $\mathbf{k}_1$ was rotated into the phase-matched direction a factor of 10 jump in the count rate on the on-axis detector was observed, with no change in the off-axis count rate. The width of acceptance for phase-matching was found to be $\delta\theta_1 = 1.6$ mrad, slightly larger than the expected 1.2 mrad, which can be calculated from the model that will be presented in the next section. Figure 7.2 displays the dependence of the phase-matched count rate on the rotation of $\mathbf{k}_1$. An iris placed in front of the phase matched detector reduced the solid angle of the on-axis detector by a factor of 11 while changing the count rate by only 9%. By reducing the iris aperture in this manner, we ensure that almost all of the counts that are detected on the on-axis counter are a result of the phase-matched process.

When using a Rydberg excitation level other than the $28D$, the frequency of k_2 and k_3 are changed and thus the angles of the beams must be changed to preserve phase matching. In fact, a change of only a few n-levels at fixed laser beam angles is enough to move the phase-matching condition outside the angular bandwidth. After changing the frequency of k_2 and k_3 to use the $58D_{5/2}$ rather than the $28D_{5/2}$, $\mathbf{k_1}$ was rotated until phase matching was again attained; the rotation angle was found to be 4.4 ± 0.3 mrad. From the k-vectors involved, we calculated the necessary rotation of $\mathbf{k}_1$ to regain phase matching to be 4.1 mrad, this value falls within the experimental uncertainty of our measurement.

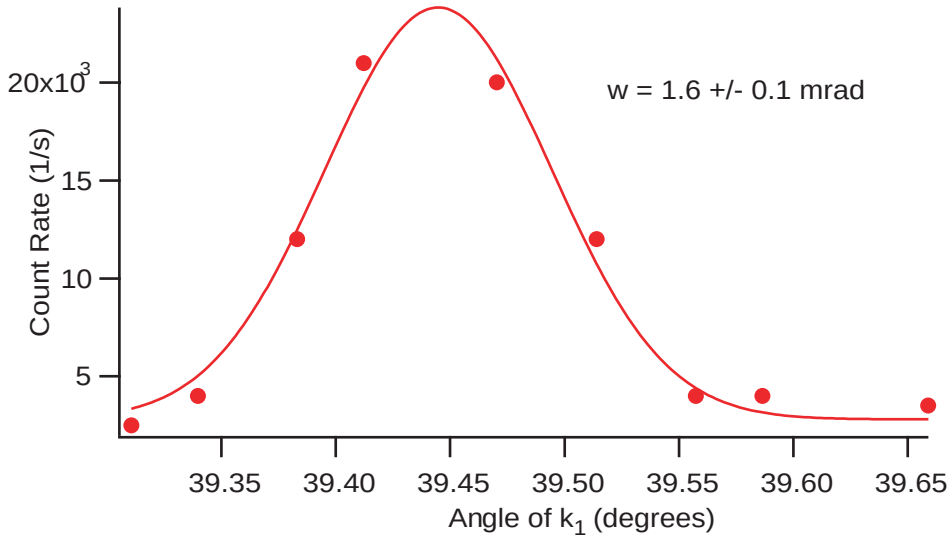

Fig. 7.2: The on-axis, or phase-matched, count rate is recorded while $\mathbf{k_1}$ is rotated through zero phase mismatch relative to the other two beams, $\mathbf{k_2}$ and $\mathbf{k_3}$.

Since k_4 is produced from three lasers with a Gaussian intensity profile, we might also expect $\mathbf{k}_4$ to have such a profile. Furthermore, if this is the case, the beam ought to propagate and diffract just as any Gaussian beam would propagate. With this in mind, we moved a razor blade across the phase-matched output beam and recorded count rate as a function of position. The waist of the phase-matched light was found to be 0.39 mm, slightly (15%) smaller than the expected diffraction limit for a Gaussian beam with a real waist of $\sim 400\mu$m at the MOT.

7.4 Model of Four-Wave Mixing

Before discussing more results from the experiment, it would be useful to have a model of four-wave mixing in order to predict the number of photons emitted by the atoms in the on-axis and off-axis directions. Neglecting propagation effects, in the absence

of blockade we can consider the four-wave mixing process to result from the spatial phasing of the atomic dipole moments as a result of the three driving fields:

$$\langle \mathbf{d}_i \rangle = \langle \mathbf{d}_0(\mathbf{r}_i) \rangle e^{i(\mathbf{k_1}+\mathbf{k_2}-\mathbf{k_3})\cdot\mathbf{r_i}}, \tag{7.1}$$

where $\mathbf{d}_i$ is the dipole moment of the ith atom and d_0 its magnitude as a function of atomic position $\mathbf{r}_i$. The fields from the atomic antennae constructively interfere in the far field to produce an electric field a large distance R away of

$$E(\phi) = \frac{n\langle d_0 \rangle k_4^2 e^{ik_4 R}}{R} \left(\frac{\pi w^2}{2}\right)^{3/2} e^{-\frac{\pi^2 w^2}{\lambda^2}\phi^2}. \tag{7.2}$$

We have assumed that the dipole moment is oriented perpendicular to the plane of the lasers, and that the effective spatial distribution of the dipoles is Gaussian with standard deviation $w/2$ and peak density n. The angle ϕ is measured with respect to the phase-matched direction.

The ratio of on-axis to off-axis powers is obtained by integrating the intensity deduced from Eq. 7.2 over the angular distribution, and comparing to the spontaneously radiated power P_o from the $6P$ state:

$$\frac{P_{pm}}{P_o} = \frac{N_e^2 2c\langle d_0 \rangle^2 k_4^2/w^2}{N_e \hbar c k_4 \Gamma_p \rho_p} \propto \frac{N_e |\sigma_{gp}|^2}{w^2 \rho_p}, \tag{7.3}$$

where $N_e = n(\pi w^2/2)^{3/2}$ is the effective number of participating atoms, ρ_p is the fraction of atoms in the $6P$ state, and σ_{gp} is the $6P$-$5S$ optical coherence density matrix element.

From Eq. 7.3 we expect the phase-matched fraction to be dependent on the number of atoms, since the phase-matched power is a nonlinear process. To verify this, the percentage of light in the phase-matched direction was measured as a function of the number of atoms in the MOT, with the results shown in Fig. 7.3. The expected nonlinear response of the four-wave mixing can be seen as a linear increase in the

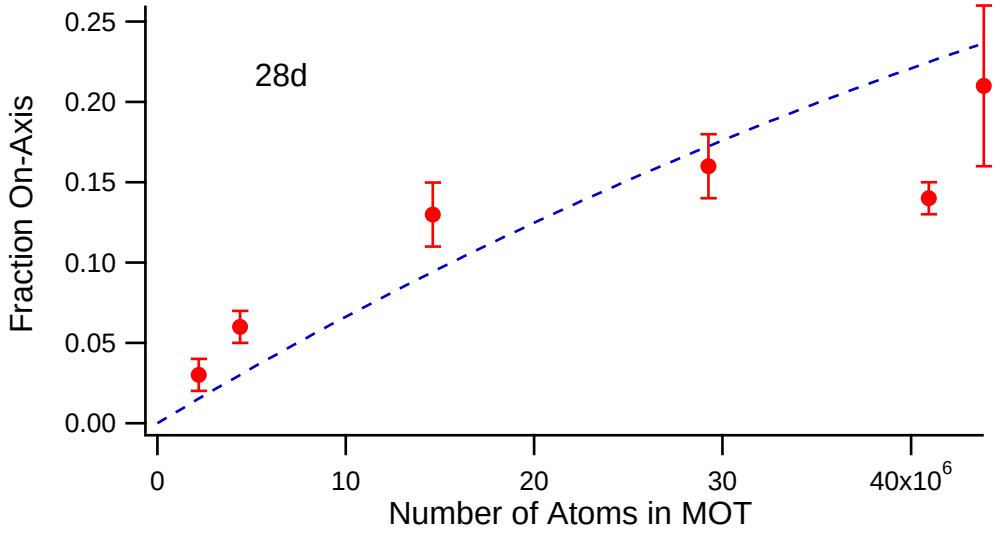

Fig. 7.3: The fraction of light emitted in the on-axis direction increases with the number of atoms in the MOT, as expected from the nonlinear character of four-wave mixing. The dashed line shows the model prediction.

phase-matched fraction with number of atoms at small atom numbers. As the cloud becomes optically thick, the phase-matched light is partially scattered due to the linear susceptibility of the atoms, and this scattered component, up to 24% for our conditions, is observed as additional off-axis light.

For a quantitative comparison with our observations, we have developed an effective three-level density matrix model of the four-wave mixing process. The $5S$ state "g" and the Rydberg state "r" are coupled by an effective two-photon Rabi frequency $\Omega_1\Omega_2/2\Delta$ ($\sim$ 4 kHz) obtained by adiabatic elimination of the $5P_{3/2}$ state. The Rydberg state is then coupled to the $6P_{3/2}$ state "e" with Rabi frequency $\Omega_3 \sim 1$ MHz. In order to simulate the effects of the substantial linewidths of the lasers used (1-3 MHz), plus other possible broadening mechanisms, we gave the σ_{rg} and σ_{re} coherences effective homogeneous broadening factors of 6 and 2 MHz chosen to reproduce the observed linewidths for two-photon excitation and non-phase-matched four-wave mixing,

respectively. In addition, the Rydberg state was assumed to have a shortened lifetime due to the effects of superradiance [Day *et al.*, 2008] as we have seen in the previous chapter, and the $6P$ state was assumed to decay at its spontaneous rate. The effects of nuclear spin were accounted for by calculating effective Rabi frequencies assuming nuclear spin conservation in the Rydberg state. Given measured intensities and atom numbers, the model then makes absolute predictions of the on- and off-axis count rates observed, and is typically within a factor of 3 of the observations.

Integral to these count rate predictions is a calculation of the distribution of atoms in the various magnetic sublevels of the $6P_{3/2}$ state. In the calculation we compute the branching ratios for all of the possible sublevel transitions in the $5S \rightarrow 5P \rightarrow nD \rightarrow 6P$ three-photon process. The calculation is cumbersome, and will be presented in full in Appendix B. As a result, we determine that the fraction of atoms in each of the hyperfine levels of the $6P$ hyperfine manifold (F=3, 2, 1, 0) is 0.498, 0.224, 0.201, and 0.074, respectively.

The on- and off-axis count rates as a function of k_3 are shown in Fig. 7.4. For off-axis light, the F′=3 count rate is slightly higher than the other F′ levels, with the F′=2 count rate being 65% of the F′=3 rate; the model predicts 48%. The on-axis light, on the other hand, has an observed 10:1 ratio for the two states. This is partly explained by a factor of $\sqrt{2}$ greater dipole matrix element for the $6P_{3/2}(\mathrm{F}' = 3) \rightarrow 5S_{1/2}(\mathrm{F}{=}2)$ transition as compared to the corresponding matrix element from the F′=2 state. In addition, there is a competition between the coherent de-excitation from the Rydberg state and the various decoherence processes that occur in the Rydberg state. This further favors the larger Rabi coupling to the F′=3 state. From these effects, the model predicts a ratio of 7.7, in reasonable agreement with the observations.

Figure 7.5 shows the on-axis fraction of the emitted light as the intensity of beam k_3 is varied, for two different hyperfine levels of the $6P$ state. The different dipole matrix

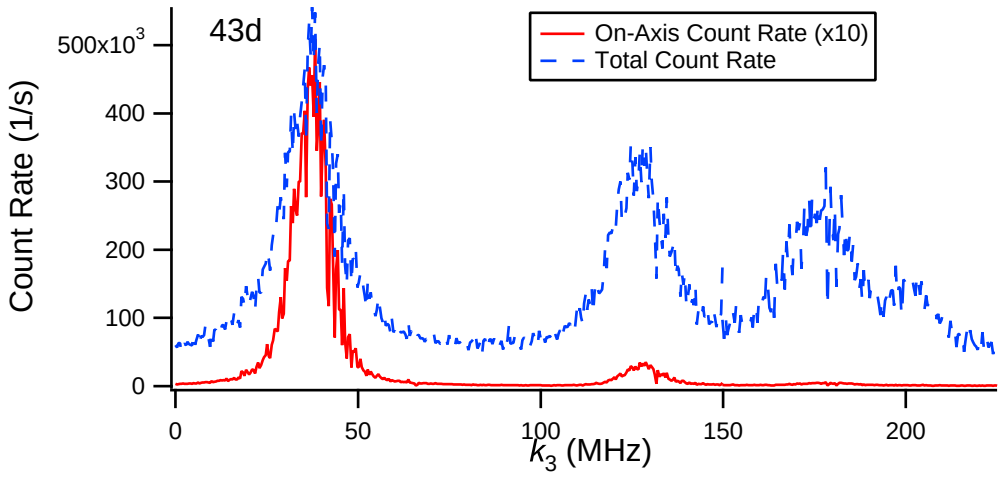

Fig. 7.4: Count rates as a function of k_3, showing the hyperfine manifold of the $6P_{3/2}$ state. The F′=3 produces strikingly more on-axis light than the other hyperfine levels due to its stronger coupling to the Rydberg state and the higher branching ratio into the F=2 ground state.

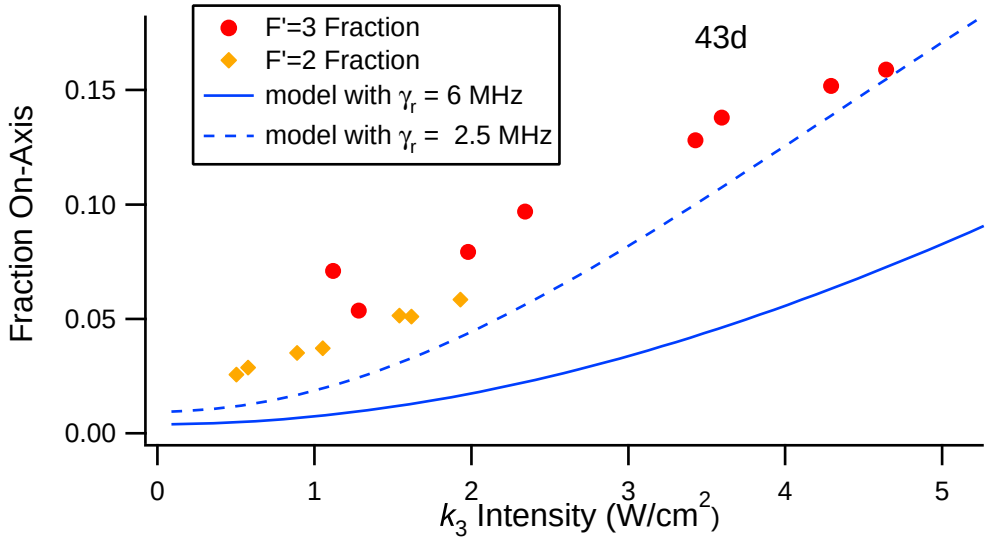

Fig. 7.5: Fraction of on-axis light as a function of intensity, with model predictions. The intensities and on-axis fractions for F′=2 data are scaled to reflect the reduced dipole matrix elements. The increased on-axis efficiency at higher intensity indicates the competition between four-wave mixing and decoherence processes.

elements for the two hyperfine levels are accounted for by scaling the F′=2 intensities by a factor of 0.48. The increase of the on-axis fraction with increased intensity shows that the four-wave mixing process is competing with decoherence. This is not surprising, since we saw in the previous two chapters that blackbody radiation and superradiance can affect the Rydberg state populations in a way that would prevent de-excitation to the $6P$ state. The model prediction is sensitive to the assumed broadening of the r-p coherence, with the data favoring a narrower (2.5 MHz) linewidth for this coherence than deduced from the off-axis spectroscopy.

7.5 Rydberg State Detuning

We now wish to take a closer look at the competition of these decoherence mechanisms with the phase-matching process. The goal here is to maximize the fraction of light that is emitted in the phase-matched direction, both to compare with our four-wave model as well as to maximize the efficiency of single-photon generation in the preferred direction for eventual use in quantum information experiments. In order to accomplish this, we will vary the Rydberg state population by detuning k_3 from the Rydberg state. I will present the data from these experiments and then compare the results with the model predictions.

If the k_2 frequency is swept across the $5P \rightarrow nD$ Rydberg transition while k_3 is detuned by a frequency δ_r from the $nD \rightarrow 6P$ transition, two resonances result. The first occurs when the excitation lasers are on resonance with the Rydberg state, giving significant Rydberg atom populations. The second resonance occurs when the three-photon process to the $6P$ state is on resonance, but two-photon excitation to the Rydberg state is off resonance by δ_r. An example of this data with k_3 tuned $\delta_r = 32$ MHz above the Rydberg-$6P_{3/2}$ F′=3 transition is shown in Fig. 7.6. As the figure shows,

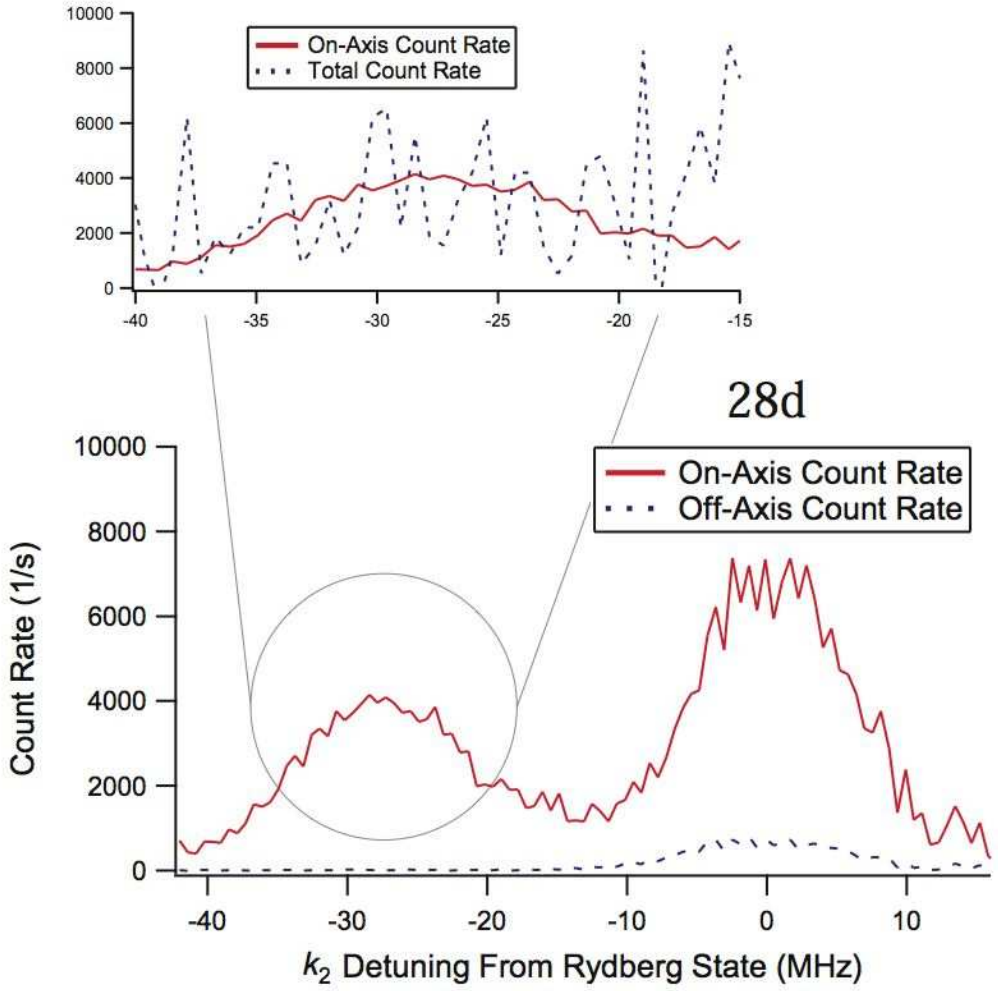

Fig. 7.6: Count rates in on- and off-axis counters as a function of the excitation frequency, showing both the non-resonant $5S$-nD excitation (left peak and inset) and resonant Rydberg-state excitation with off-resonant de-excitation to the $6P$ state. The k_3 laser was held 32 MHz above the Rydberg-$6P$ transition. The inset scales the off-axis count rate by the solid angle to show the total amount of light emitted. In this case, the amount of on-axis light is approximately equal to the total amount of light in all other directions.

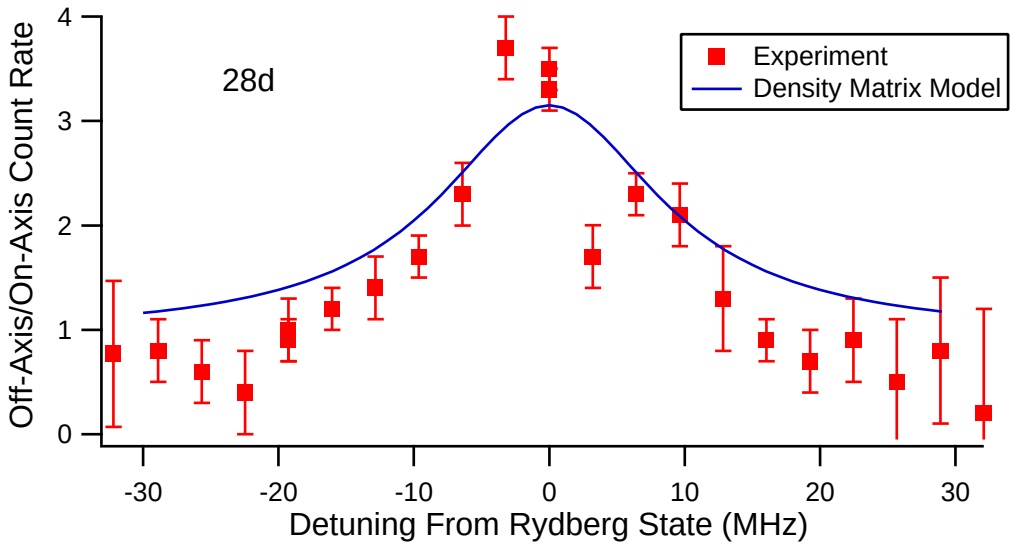

Fig. 7.7: The maximum ratio of random counts to phase-matched counts measured as a function of detuning from the Rydberg state. Here a ratio of zero corresponds to perfect phase matching. The efficiency of the phase-matching process is optimized when detuned from the Rydberg state.

the count rate on the off-axis counter is very small for off-resonant Rydberg excitation. The fraction of phase-matched light reaches 50% of the total $6P$-$5S$ emission. When the Rydberg states are resonantly produced, the fraction of phase matched light drops to 20%.

Figure 7.7 shows the ratio of off-axis to on-axis light as a function of two-photon detuning, with k_3 adjusted to maintain three-photon resonance. The ratio is displayed in this manner rather than as the phase-matched fraction because the number of detected off-axis counts is on the order of $\sim$10 s^{-1} for detunings larger than 15 MHz. This results in an error associated with the measurement of the off-axis count rate comparable to the measured rate. This in turn makes displaying a phase-matched fraction problematic since the error bars would be large. Instead, we display the ratio of the off-axis to on-axis count rate, which will go to zero when all of the light is phase-matched and

to infinity when all of the light is non-phase-matched. Again, the ratio in Figure 7.7 corresponds to a fraction of on-axis light of about 20% on resonance, increasing to 50% off resonance. This trend is accounted for by the model as seen in the Figure.

These results point out that Rydberg decoherence mechanisms are important for determining the on-axis emission efficiency. The data presented here are all obtained under weak excitation conditions where blockade effects should be unimportant. Under blockade conditions, Rydberg-Rydberg and superradiant decoherence mechanisms are predicted to be virtually eliminated. As a step towards using phase-matched four-wave mixing as a single-photon source, we have focused the 480 nm and 1015 nm beams to 12 μm. This results in a effective volume of $\sim 10^{-8}$ cm^3, which could be blockaded for reasonable n-levels [Walker and Saffman, 2008]. When using the focused beams, phase-matching was again achieved for the various n-levels, with the same dependence on F$'$ level, k_3 intensity, and detuning from the Rydberg state. The maximum percentage of light achieved in the phase-matched direction was reduced to below 1%, as expected from Eq. 7.3 since the relevant factor N_e/w^2 was reduced by a factor of 40. In the future, this could be be improved by increasing the density of the sample [Sebby-Strabley *et al.*, 2005], allowing both efficient phase-matching and dipole blockade and making a single-photon source possible.

8. CONCLUSION

8.1 Summary

In this thesis, I have presented the results of a variety of Rydberg atom experiments designed to give us a better understanding of the dynamics atomic interactions a Rydberg levels. In particular, we have observed wider than expected two-photon Rydberg transitions of 8-10 MHz and developed a novel technique for measuring these linewidths. The width of these transitions will make a dipole blockade more difficult, and will likely require the D-state Rydberg levels to be mixed with nearby F-states in order to utilize the dipole-dipole interactions that this state dressing would allow. Our attempts to coherently excite Rydberg states using STIRAP were unsuccessful because processes such as superradiance quickly populate other nearby Rydberg levels and dephase the coherent excitation/de-excitation process.

We have developed a state-probe laser as an alternative to field ionization in order to investigate the dynamics of atoms in the Rydberg state. This has allowed us to determine the transfer rate out of the Rydberg state into nearby states which led to the proposal of superradiant decay as the primary cause of this state transfer. The work presented here was the first published that recognized the importance of superradiance to the rapid population of other Rydberg states observed at higher Rydberg atom densities. Finally, we have accomplished coherent excitation through the Rydberg state with four-wave mixing. Coherent manipulation of Rydberg states has been accomplished by

only a few research groups up to this point ([Johnson *et al.*, 2008], [Cubel *et al.*, 2005], [Mohapatra *et al.*, 2007], [Reetz-Lamour *et al.*, 2008], [Heidemann *et al.*, 2008]) because of the strong interactions involved. Going forward, the four-wave geometry will provide an excellent setup for dipole blockade experiments.

8.2 Future Work

In the near future, the next phase in this experiment will be to return to the dressed state experiments using microwaves. In our most recent microwave experiments, we dressed the $43D$ Rydberg state with the nearby $42F$ state using strong microwave fields that were on the order of $\sim$100 MHz off resonance with the $43D \rightarrow 42F$ transition. By sweeping the 480 nm laser across this transition, we observed an Autler-Townes splitting similar to those seen in the experiments in Chapter 4. The difference, however, was that because of the detuning, one of the peaks was narrower than the 8 MHz Rydberg transition linewidths we have measured up to this point. This may have been a result of mixing the D- and F-states such that the narrow peak had a large F-state component and a small D-state component, but this is not entirely clear. This certainly merits further study since a reduction of the Rydberg linewidths would be very helpful in achieving a large blockade radius.

The difficulty with using detuned microwaves to dress Rydberg D-states with F- or P-states is that the AC Stark shift of the microwave beam will shift the sublevels in the excitation Rydberg state by different amounts, which should actually broaden the Rydberg transition. However, if two microwave frequencies, one tuned Δ^+ above the D-to-F transition and one tuned Δ^- below the transition, were applied to the atoms, then the AC Stark shifts on the sublevels should be equal and opposite. This should keep the microwave transition as narrow as possible while still providing the

state mixing with the nearby F- or P-state that would allow for stronger dipole-dipole interactions.

Following these microwave experiments, the next step will likely be to put the atoms into a Far Off-Resonance Trap (FORT) produced by a 20 W Nd:YAG laser and perform four-wave mixing with the atoms in this setup. We have used the YAG laser in the past to produce high density traps with $n = 2 \times 10^{15}$ cm^{-3} the highest density reported in an optical trap for incoherent matter [Sebby-Strabley *et al.*, 2005]. With densities of this order, we could greatly increase the collective dipole moment of the atoms in the four-wave mixing experiment, which would allow a higher fraction of light to be radiated into the phase-matched direction. This would be an ideal setup for a photon anti-bunching experiment, which would entail the measurement of the second-order correlation function, $g^{(2)}$ of the light emitted into the phase-matched direction. Under strong dipole-blockade conditions, the second-order correlation function will go to zero at small time delays. Physically, this means that only one atom can be excited to the Rydberg level at a time because of blockade effects, and thus the probability of observing two decay photons arriving within $\sim$ 100 ns of each other is vanishingly small.

Another interesting feature of the dipole blockade is that the blockaded atoms ought to collectively enhance the excitation of a single atom to the Rydberg state in much the same way that atoms in the Rydberg state collectively enhance the decay rate of the state to nearby Rydberg level via superradiance. Indeed, evidence for this effect was recently observed by Tilman Pfau's group [Heidemann *et al.*, 2007], though our FORT experiment ought to be able to produce a stronger signal since a few thousand atoms will be blockaded in such a setup [Sebby-Strabley *et al.*, 2005].

Finally, it would also be interesting to continue our experiments into the superradiant decay of Rydberg states. Although we presented strong evidence of superradiant

transfer from the excitation Rydberg state into other Rydberg levels, we were not able to directly observe the populations in these other states. It would be interesting to observe the rapid increase in the population of the $29P$ state shortly after excitation to the $28D$ Rydberg level. This might be possible using a $\sim$ 100 mW diode laser at 1260 nm to de-excite the $29P$ atoms down to the $5D$ state and then observing the decay along the $5D \rightarrow 5P$ transition at 775 nm. From our model, the $29P$ should have a higher equilibrium population than the $27D$ state that we tried to probe with the 1015 nm state probe laser.

8.3 Design of a Single-Photon Source

In order to determine how we might construct a single-photon source, I must first calculate what kind of photon rates we could expect from our experiment if it were conducted with a focused-beam four-wave mixing geometry in the Far Off-Resonance Trap. Using the FORT described here [Sebby-Strabley, 2004], we have produced optical microtraps after evaporation and recompression with dimensions 300 nm $\times$ 300 nm $\times$ 8 μm, where the long dimension is in the plane of the optical table orthogonal to the 480 nm laser direction (see Fig. 2.2). The center microtrap contained 2000 atoms for an average atomic density of $n_e = 2{\times}10^{15}$ cm^{-3}. For the four-wave geometry discussed in the previous chapter, the fraction of phase-matched light was found to go as $P_{pm}/P_o \propto N_e/w^2 \propto n_e w$ (see Eq. 7.3). Thus despite the factor of 40 reduction in the sample width, the density increases by a factor of $\sim$200,000 ensuring that practically all of the light emitted goes into the phase-matched direction. Similarly, the rate of production of phase-matched photons will be $\sim n_e w^4 \langle d_0 \rangle^2$ which amounted to a factor of $\sim$1000 reduction for the $43D$-state focused beam experiments (the phase-matched count rate for the $43D$ focused beam experiment was 500/s). However, this will once

again be offset by the increase in density so that our phase-matched count rate would increase by a factor of 200 to a rate of 10^5/s.

Provided that we have a perfect dipole blockade, the phase-matched photon beam should exhibit strong anti-bunching. Also, we should observe a $\sqrt{N}$ enhancement in the excitation rate and thus in the dipole moment d_0 which determines the rate of phase-matched photon generation [Saffman and Walker, 2002]. This would put our total rate over 10^6/s and thus the 780 nm excitation laser could be switched on for the duration of a 2π-pulse every 10 μs to produce a single photon on demand. However, since the atomic sample has a waist of 300 nm in the vertical direction, the 420 nm light emitted will diverge too rapidly to be completely collected by the collimating lens. Assuming diffraction-limited propagation, the 420 nm beam would overfill the 150 mm focal length collimating lens by a factor of 5, so some of this light would be lost. This would affect the fidelity of the production of single photons for a particular 2π-pulse, but would not affect the rate of photon production drastically. This could be remedied somewhat by changing the angle of intersection of the FORT beams from 100 mrad to 50 mrad [Newell, 2003]. In such a setup the effective microtrap size doubled, which means that we could expect a recompressed microtrap size of roughly 600 nm $\times$ 600 nm $\times$ 16 μm. The problem with such a setup is that the long dimension would then be longer than the 12μm beamwaist of the 480 nm excitation laser. This would mean that the edges of the microtrap would not experience as great an excitation rate which would mean a smaller effective number of atoms participating and a smaller phase-matched count rate. This might allow for simultaneous excitation of Rydberg atoms and compromise the blockade. A more permanent solution would be to use two FORT beams intersecting at a 90° angle to make the trap symmetric with a trap size of about 10 μm in each direction.

We also need to consider the atomic interaction strengths here. Excitation to the

$43D$-state is interesting because of the small energy defect of the $43D_{5/2} + 43D_{5/2}$ and $41P_{3/2} + 45F_{5/2}$ potential curves. By optically pumping the atoms in the MOT into the $5S, F = 2, m_F = +2$ sublevel and performing Rydberg excitation with σ^+ polarized light, we can prevent the excitation of linear combinations of Rydberg sublevels with zero van der Waals interaction [Walker and Saffman, 2008]. We can estimate the van der Waals interactions between these atoms as $V_{vdW} \sim C_6 D_\phi / R^6$, where for this channel $C_6 = -546$ GHz μm^6, and $D_\phi = .343$ [ibid.]. We need the interaction strength to be greater than the observed transition linewidth of 8 MHz ($V_{vdW} > \Gamma$) which will be true for R < 5.3 μm. This is not quite strong enough to prevent double excitation into the Rydberg state, but if we additionally couple the $43D$-state to the $42F$-state via resonant microwaves this should provide dipole-dipole interactions that should be more than enough to blockade the remainder of the microtrap with modest microwave powers.

APPENDIX

A. DERIVATION OF TRANSITION LINEWIDTHS FROM INTENSITY CORRELATED SPECTROSCOPY PEAKS

We wish to determine the transition linewidth starting from the width of the peaks on a coincidence delay time histogram as discussed in Chapter 4. Consider a triangle ramp (such as that seen in Fig. 4.3) with period T and angular frequency $\omega = 2\pi/T$ that sweeps the frequency of the Rydberg excitation lasers across the two-photon $5S \rightarrow nD$ resonance. The photon counter measures the intensity of incoming light $f(t)$, which is sharply peaked when the excitation lasers are on resonance at time t_a and later, when the ramp is moving in the opposite direction, at time t_b. The photon counter measures the intensity in discrete time bins n, so the intensity at time t will be given by:

$$f(t) = \sum_n f_n e^{-in\omega t}. \tag{A.1}$$

The function f(t) will be sharply peaked at times t_a and t_b. Let $S(\tau)$ represent the coincidence delay time histogram value for a delay time of τ. $S(\tau)$ will then be equal to,

$$S(\tau) = f(t)f(t+\tau) = \sum_n f_n f_{-n} e^{in\omega\tau}. \tag{A.2}$$

This is the equation that describes the data seen in Fig. 4.3(b). However, it will take some work to see how this will relate to the transition linewidths. We may take the inverse Fourier transform to find f_n,

$$f_n = \frac{1}{T}\int_0^t dt' f(t') e^{in\omega t'}. \tag{A.3}$$

Substituting $t = t' - t_a$ and $t = t' - t_b$ since these are the times of interest, the above equation becomes,

$$f_n \approx \left(\frac{e^{in\omega t_a}}{T} + \frac{e^{in\omega t_b}}{T}\right)\int_\infty^\infty dt\sigma(t) e^{in\omega t}, \tag{A.4}$$

where we have let $\sigma(t)$ represent $f(t)$ in the transform integral. As the excitation laser frequency sweeps across the transition resonance, the intensity will have a Gaussian profile with respect to time:

$$\sigma(t) = Ae^{\frac{-2t^2}{\delta^2}}, \tag{A.5}$$

where δ is the $1/e^2$ Gaussian transition linewidth. Now, for the purposes of determining the transition widths, we can ignore the constants $e^{in\omega t_a}/T$ and $e^{in\omega t_b}/T$. In addition, since the repetition period $T \gg \delta$ the repetition function $e^{in\omega t}$ will not affect the width either. Thus we can approximate the width of peaks on the correlated time delay histogram as,

$$S(\tau) = f(t)f(t+\tau) \propto \int_{-\infty}^{\infty} dt A^2 e^{\frac{-2t^2}{\delta^2}} e^{\frac{-2(t+\tau)^2}{\delta^2}}. \tag{A.6}$$

This is simply a convolution function of two Gaussians, the result is

$$S(\tau) \propto A^2 e^{\frac{-2\tau^2}{2\delta^2}} = A^2 e^{\frac{-2\tau^2}{(\sqrt{2}\delta)^2}} \tag{A.7}$$

Thus the width of the peaks on the coincidence time delay histogram will be $\sqrt{2}$ larger than the transition linewidths.

B. DISTRIBUTION OF ATOMS IN THE 6P HYPERFINE MANIFOLD

In the four-wave mixing experiments described in Chapter 7, we have a need to determine the relative population of the various hyperfine levels in the $6P_{3/2}$ state. This appendix will present the calculation that was performed in order to arrive at the numbers quoted in Chapter 7. In order to accomplish this we will need to begin with several assumptions. First, we assume for the purposes of this calculation that all atoms are in the $5S_{1/2}, F = 2$ ground state and that these atoms are equally distributed among the five magnetic sublevels ($m_F = 0, \pm 1, \pm 2$). Furthermore, we will assume that linearly polarized light is used and that the magnetic sublevels $|m_F\rangle$ are not good quantum numbers in the Rydberg level. We will deal with the latter by allowing the electron spin $|m_J\rangle$ to change while the nuclear spin $|m_I\rangle$ is conserved.

Now we will calculate the relative oscillator strengths between all of the relevant sublevels along the three-photon $5S \rightarrow 5P \rightarrow nD \rightarrow 6P$ transition. I will begin with the oscillator strength averaged over the polarization states of light. For this and the other oscillator strength formulae presented here, [Weissbluth, 1978] is an excellent reference and all of these formulae can be found within. I will then use the oscillator strength formula to determine the relative strength of the various sublevel transitions. This will allow me to calculate the transfer matrix from the $5S$ sublevels to the $5P$ sublevels. Next I will present the decomposition of the $5P_{3/2}, |Fm_F\rangle$ state into its $|Im_I\rangle\,|Jm_J\rangle$ components. These pieces will give me all that I need to calculate the

relative population of the $6P$ hyperfine levels.

The oscillator strength for a transition $|nFm_F\rangle \rightarrow |n'F'm'_F\rangle$, for linearly polarized light, is given by

$$f = \frac{2m\omega}{3\hbar(2F+1)} |\langle F'| |\mathbf{r}| |F\rangle|^2 \begin{pmatrix} F & 1 & F' \\ -m_F & 0 & m'_F \end{pmatrix}^2, \tag{B.1}$$

where m is the electron mass, and the parentheses represent the three-j symbol coupling the two hyperfine levels with the photon polarization vector. The quantity, $|\langle F'| |\mathbf{r}| |F\rangle|^2$ is the reduced matrix element for the hyperfine vectors. This in turn can be expressed as a reduced matrix element for the total angular momentum $\mathbf{J}$ as follows

$$|\langle F'| |\mathbf{r}| |F\rangle|^2 \propto (2F+1)(2F'+1) |\langle n'J'| |\mathbf{r}| |nJ\rangle|^2 \begin{Bmatrix} F' & 1 & F \\ J & I & J' \end{Bmatrix}^2, \tag{B.2}$$

where the quantity in the { } brackets is a 6-j symbol. The reduced matrix element in terms of $\mathbf{J}$ will be the same for all hyperfine levels F and magnetic sublevels m_F, thus we can disregard this term. In fact, combining Equations B.1 and B.2 we may collect the terms that affect the relative oscillator strength:

$$f \propto (2F'+1) \begin{pmatrix} F & 1 & F' \\ -m_F & 0 & m'_F \end{pmatrix}^2 \begin{Bmatrix} F' & 1 & F \\ J & I & J' \end{Bmatrix}^2. \tag{B.3}$$

Now we may calculate the transfer matrix from the $5S \rightarrow 5P$ state, $\mathbf{S} = \langle 5P| r |5S\rangle$, using $\sqrt{f}$ as calculated from equation B.3 for the elements of the transfer matrix. This matrix transforms the $|Fm_F\rangle$ vector of the $5S$ magnetic sublevel populations into the state vector $|F'm'_F\rangle$ of the $5P$ magnetic sublevel populations.

Since the excitation lasers are tuned above the $5P_{3/2}, F' = 3$ state by 470 MHz, we must have a detuning matrix $\mathbf{\Delta}$ which is a diagonal matrix where the elements are equal to $1/\sqrt{\delta_F}$ where δ_F is the detuning of the excitation lasers from the $5P_{3/2}, F'$ hyperfine level.

Now we must decompose the $|5P_{3/2}Fm_F\rangle$ into its $|Im_I\rangle\,|Jm_J\rangle$ components. The matrix **D1** which describes this basis state transformation has components:

$$|5P_{3/2}Fm_F\rangle = C^{Fm_F}_{\frac{3}{2}m_JIm_I}\,|5P_{3/2}m_Jm_I\rangle\,, \tag{B.4}$$

where the $C^{Fm_F}_{\frac{3}{2}m_JIm_I}$ term represents the Clebsch-Gordan coefficients which make up the matrix elements. We then can calculate the transfer matrix $\mathbf{R}$ for the $5P \rightarrow nD$ Rydberg transition using the $|Im_I\rangle\,|Jm_J\rangle$ basis. The elements of $\mathbf{R}$ are as follows,

$$\mathbf{R} = \langle nDJ'm'_J|\,r\,|5PJm_J\rangle \propto C^{J'm'_J}_{JmJ10} \tag{B.5}$$

where the Clebsch-Gordan coefficients are calculated using linearly polarized light, as noted at the beginning of the Appendix. Calculating the transfer matrix $\mathbf{P}$ for the $nD \rightarrow 6P$ transition is now straightforward as,

$$\mathbf{P} = \langle 6PJ'm'_J|\,r\,|nDJm_J\rangle \propto C^{J'm'_J}_{JmJ10}. \tag{B.6}$$

Similarly, the transformation **D2** from the $|Im_I\rangle\,|Jm_J\rangle$ basis in the $6P$ to the $|Fm_F\rangle$ basis goes as expected,

$$|6P_{3/2}m_Jm_I\rangle = C^{Fm_F}_{\frac{3}{2}m_JIm_I}\,|6P_{3/2}Fm_F\rangle\,. \tag{B.7}$$

We now have all of the matrices required to transform the state vector of the $5S$ sublevels, $|5S_{1/2}Fm_F\rangle$ = (0.2, 0.2, 0.2, 0.2, 0.2), into the state vector of the $6P_{3/2}$ sublevels. Namely,

$$|6P_{3/2}F'm'_F\rangle = (\mathbf{D2}\cdot\mathbf{R}\cdot\mathbf{P}\cdot\mathbf{D1}\cdot\mathbf{\Delta}\cdot\mathbf{S})^2\,|5S_{1/2}Fm_F\rangle\,. \tag{B.8}$$

Equipped with the $6P$ state vector, we may normalize the vector and sum the sublevels of similar F-levels to give us the hyperfine state distribution of atoms in the $6P$ state. As noted in the text, this is,

$$|6P_{3/2}F'\rangle = \begin{pmatrix} F'=3 \\ 2 \\ 1 \\ 0 \end{pmatrix} = \begin{pmatrix} 0.498 \\ 0.224 \\ 0.201 \\ 0.074 \end{pmatrix} \tag{B.9}$$

BIBLIOGRAPHY

[Afrousheh *et al.*, 2006] K. Afrousheh, P. Bohlouli-Zanjani, J. D. Carter, A. Mugford, and J. D. D. Martin, "Resonant electric dipole-dipole interactions between cold Rydberg atoms in a magnetic field", Phys. Rev. Lett. **73**, 063403 (2006).

[Amthor *et al.*, 2007] T. Amthor, M. Reetz-Lamour, S. Westermann, J. Denskat, and M. Weidemüller, "Mechanical Effect of van der Waals Interactions Observed in Real Time in an Ultracold Rydberg Gas", Phys. Rev. Lett. **98**, 023004 (2007).

[Anderson *et al.*, 1998] W. R. Anderson, J. R. Veale, and T. F. Gallagher, "Resonant Dipole-Dipole Energy Transfer in a Nearby Frozen Rydberg Gas", Phys. Rev. Lett. **80**, 249 (1998).

[Barreiro *et al.*, 2008] J. T. Barreiro, T. Wei, and P. G. Kwiat, "Beating the channel capacity limit for linear photonic superdense coding", Nature Physics **4**, 282 (2008).

[Bergmann *et al.*, 1998] K. Bergmann, H. Theuer, and B. W. Shore, "Coherent population transfer among quantum states of atoms and molecules", Rev. Mod. Phys. **70**, 1003 (1998).

[Beterov *et al.* (2007)] I. I. Beterov, D. B. Tretyakov, I. I. Ryabtsev, A. Ekers, and N. Bezuglov, "Ionization of sodium and rubidium nS, nP, and nD Rydberg atoms by blackbody radiation", Phys. Rev. A **75**, 052720 (2007).

[Bohlouli-Zanjani *et al.*, 2007] P. Bohlouli-Zanjani, J. A. Petrus, and J. D. D. Martin, "Enhancement of Rydberg Atom Interactions Using ac Stark Shifts", Phys. Rev. Lett. **98**, 203005 (2007).

[Boyd and Kleinman, 1968] G. D. Boyd, and D. A. Kleinman, "Parametric Interaction of Focused Gaussian Light Beams", J. Appl. Phys. **39**, 3597 (1968).

[Brekke *et al.*, 2008] E. Brekke, J. O. Day, and T. G. Walker, "Four-Wave Mixing in Ultracold Atoms using Intermediate Rydberg States", arXiv:0808.0862v1 (2008).

[Cubel *et al.*, 2005] T. Cubel, B. K. Teo, V. S. Malinovsky, J. R. Guest, A. Reinhard, B. Knuffman, P. R. Berman, and G. Raithel, "Coherent population transfer of ground-state atoms into Rydberg states", Phys. Rev. A **72**, 023405 (2005).

[Day *et al.*, 2008] J. O. Day, E. Brekke, and T. G. Walker, "Dynamics of low-density ultracold Rydberg gases", Phys. Rev. A **77** 052712 (2008).

[Dicke, 1954] R. H. Dicke, "Coherence in Spontaneous Radiation Processes", Phys. Rev. **93**, 99 (1954).

[DiVincenzo, 2000] D. DiVincenzo, "The Physical Implementation of Quantum Computation", arXiv:quant-ph/0002077v3 (1996).

[Dmitriev, 1997] V. G. Dmitriev, *Handbook of Nonlinear Optical Crystals*, 2nd. Ed., (Springer, New York, 1997.)

[Fan *et al.*, 1987] T. Y. Fan, C. E. Huang, B. Q. Hu, R. C. Eckardt, Y. X. Fan, R. L. Byer, and R. S. Feigelson, "Second harmonic generation and accurate index of refraction measurements in flux-grown $KTiOP0_4$", Appl. Opt. **26**, 2390 (1987).

[Farooqi *et al.*, 2003] S. M. Farooqi, D. Tong, S. Krishnan, J. Stanojevic, Y. P. Zhang, J. R. Enshwer, A. S. Estrin, C. Boisseau. R. Cote, E. E. Eyler, and P. L. Gould, "Long-Range Molecular Resonance in Cold Rydberg Gas", Phys. Rev. Lett. **91**, 183002 (2003).

[Fejer *et al.*, 1992] M. M. Fejer, G. A. Magel, D. H. Jundt, and R. L. Byer, "Quasi-Phase-Matched Second Harmonic Generation: Tuning and Tolerances", IEEE J. Quantum Electron. **28** 2631 (1992).

[Gallagher, 1994] T. F. Gallagher, *Rydberg Atoms*, (Cambridge University Press, Cambridge, 1994.)

[Gallagher *et al.*, 2003] T. F. Gallagher, P. Pillet, M. P. Robinson, B. Laburthe-Tolra, M. Noel, "Back and forth between Rydberg atoms and ultracold plasmas", J. Opt. Sci. Amer. B **20**, 1091 (2003).

[Gisin *et al.*, 2002] N. Gisin, G. Ribordy, W. Tittel, and H. Zbinden "Quantum cryptography", Rev. Mod. Phys., **74**, 145 (2002).

[Gounand *et al.*, 1979] F. Gounand, M. Hugon, P. R. Fournier, and J. Berlande, "Superradiant cascading effects in rubidium Rydberg levels", Journal of Physics B **12**, 547 (1979).

[Grabowski *et al.*, 2005] A. Grabowski, R. Heidemann, R. Löw, J. Stuhler, and T. Pfau, "High Resolution Rydberg Spectroscopy of ultracold Rubidium Atoms", arXiv:quant-ph/0508082v1 (2005).

[Gross and Haroche, 1982] M. Gross, and S. Haroche, "Superradiance: An Essay on the Theory of Collective Spontaneous Emission", Phys. Rep. 93 (1982) 301.

[Grover, 1996] L. Grover, "A Fast Quantum Mechanical Algorithm for Database Search", arXiv:quant-ph/9605043v3 (1996).

[Han *et al.*, 2006] J. Han, Y. Jamil, D. V. L. Norum, P. J. Tanner, and T. F. Gallagher, "Rb nf quantum defects from millimeter-wave spectroscopy of cold ^{85}Rb Rydberg atoms", Phys. Rev. A **74**, 054502 (2006).

[Hanbury Brown and Twiss, 1956] R. Hanbury Brown and R. Q. J. Twiss, "A Test of a New Type of Stellar Interferometer on Sirius", Nature **178**, 1046 (1956).

[Heidemann *et al.*, 2007] R. Heidemann, U. Raitzsch, V. Bendkowsky, B. Butscher, R. Löw, L. Santos, and T. Pfau, "Evidence for coherent collective Rydberg excitation in the strong blockade regime", Phys. Rev. Lett. **99**, 163601 (2007).

[Heidemann *et al.*, 2008] R. Heidemann, U. Raitzsch, V. Bendkowsky, B. Butscher, R. Löw, and T. Pfau, "Rydberg Excitation of Bose-Einstein Condensates", Phys. Rev. Lett. **100**, 033601 (2008).

[Högele *et al.*, 2008] A Högele, C. Galland, M. Winger, and A. Imamoğlu "Photon Antibunching in the Photoluminescence Spectra of a Single Carbon Nanotube", Phys. Rev. Lett. **100**, 217401 (2008).

[Jaksch *et al.*, 2000] D. Jaksch, J. I. Cirac, P. Zoller, S. L. Rolston, R. Cote, M. D. Lukin, "Fast Quantum Gates for Neutral Atoms", Phys. Rev. Lett **85**, 2208 (2000).

[Johnson *et al.*, 2008] T. A. Johnson, E. Urban, T. Henage, L. Isenhower, D. D. Yavuz, T. G. Walker, and M. Saffman "Rabi Oscillations between Ground and Rydberg States with Dipole-Dipole Atomic Interactions", Phys. Rev. Lett **100**, 113003 (2008).

[Kato, 1992] K. Kato, "Temperature insensitive SHG at 0.5321 μm in KTP", IEEE J. Quantum Electron. **28**, 1974 (1987).

[Killian *et al.*, 1999] T. C. Killian, S. Kulin, S. D. Bergeson, L. A. Orozco, C. Orzel, and S. L. Rolston, "Creation of an Ultracold Neutral Plasma", Phys. Rev. Lett. **83**, 4776 (1999).

[Knill *et al.*, 2001] E. Knill, R. Laflamme, and G. J. Milburn, "A scheme for efficient quantum computation with linear optics", Nature **409**, 46 (2001).

[Li *et al.*, 2003] W. Li, I. Mourachko, M. W. Noel, and T. F. Gallagher, "Millimeter-wave Spectroscopy of Cold Rb Rydberg Atoms in a Magneto-Optical Trap: Quantum Defects of the ns, np, and nd series", Phys. Rev. A **67**, 052502 (2003).

[Li *et al.*, 2004] W. Li, M. W. Noel, P. J. Tanner, and T. F. Gallagher, "Evolution dynamics of a dense frozen Rydberg gas to plasma", Phys. Rev. A **70**, 042713 (2004).

[Li *et al.*, 2005] W. Li, P. J. Tanner, and T. F. Gallagher, "Dipole-Dipole Excitation and Ionization in an Ultracold Gas of Rydberg Atoms", Phys. Rev. Lett. **94**, 173001 (2005).

[Lodahl *et al.*, 1997] P. Lodahl, J.L. Sorensen, E.S. Polzik "High efficiency second harmonic generation with a low power diode laser", Appl. Phys. B **64**, 383 (1997).

[Loudon, 1983] R. Loudon, *The Quantum Theory of Light*, 3rd Ed. (Clarendon Press, Oxford, 1983.)

[Lounis and Orrit, 2005] B. Lounis and M. Orrit "Single-photon sources", Rep. Prog. Phys. **68**, 1129 (2005).

[Ludvigsen *et al.*, 1998] H. Ludvigsen, M. Tossavainen, and M. Kaivola, "Laser linewidth measurements using self-homodyne detection with short delay", Opt. Comm. **155**, 180 (1998).

[Lukin *et al.*, 2001] M. D. Lukin, M. Fleischauer, R. Cote, L. M. Duan, D. Jaksch, J. I. Cirac, and P. Zoller, "Dipole Blockade and Quantum Information Processing in Mesoscopic Atomic Ensembles", Phys. Rev. Lett. **87**, 037901 (2001).

[McKeever *et al.*, 2004] J. McKeever, A. Boca, A. D. Boozer, R. Miller, J. R. Buck, A. Kuzmich, and H. J. Kimble, "Deterministic Generation of Single Photons from One Atom Trapped in a Cavity", Science **303** 1992 (2004).

[Metcalf and van der Straten, 1999] H. Metcalf and P. van der Straten, *Laser Cooling ad Trapping*, (Springer-Verlag, New York, 1999.)

[Mohapatra *et al.*, 2007] A. K. Mohapatra, T. R. Jackson, and C. S. Adams, "Coherent Optical Detection of Highly Excited Rydberg States Using Electromagnetically Induced Transparency", Phys. Rev. Lett. **98** 113003 (2007).

[Newell, 2003] R. T. R. Newell, "Cold and Dense Clouds of Atoms in a Holographic Atom Trap", Doctoral Thesis, University of Wisconsin-Madison, (2003).

[Nielsen *et al.*, 2000] M. A. Nielsen, and I. L. Chuang, *Quantum Computation and Quantum Information*, (Cambridge University Press, New York, 2000.)

[O'Hara *et al.*, 1999] K. M. O'Hara, S. R. Granade, M. E. Gehm, T. A. Savard, S. Bali, C. Freed, and J. E. Thomas, "Dynamics of noise-induced heating in atom traps", Phys. Rev. A **58**, 3914 (1998).

[Pan *et al.*, 2000] J. W. Pan, D. Bouwmeester, M. Daniell, H. Weinfurter, and A. Zeilinger, "Experimental test of quantum nonlocality in three-photon Greenberger-Horne-Zeilinger entanglement", Nature **403**, 515 (2000).

[Polzik and Kimble, 1991] E. S. Polzik, and H. J. Kimble, "Frequency doubling with $KNbO_3$ in an external cavity", Opt. Lett. **15**, 1400 (1991).

[Reetz-Lamour *et al.*, 2008] M. Reetz-Lamour, T. Amthor, J. Deiglmayr, and M. Weidemuller, "Rabi Oscillations and Excitation Trapping in the Coherent Excitation of a Mesoscopic Frozen Rydberg Gas", arXiv:0711.4321v2 (2008).

[Rarity *et al.*, 1994] J. G. Rarity, P. C. M. Owens, and P. R. Tapster, "Quantum random-number generation and key sharing", J. Mod. Opt. **41**, 2435 (1994).

[Rehler and Eberly, 1971] N. E. Rehler and J. H. Eberly, "Superradiance", Phys. Rev. A **3**, 1735 (1971).

[Roberts *et al.*, 2004] J. L. Robers, C. D. Fertig, M. J. Lim, S. L. Rolston, "Electron Temperature of Ultracold Plasmas", Phys. Rev. Lett. **92**, 253003 (2004).

[Saffman and Walker, 2002] M. Saffman and T. G. Walker, "Engineering single atom and single photon sources from entangled atomic ensembles", Phys. Rev. A **66**, 065403 (2002).

[Sebby-Strabley, 2004] J. Sebby-Strabley, "Demonstration of Dense Mesoscopic Atomic Clouds in a Holographic Atom Trap", Doctoral Thesis, University of Wisconsin-Madison, (2004).

[Sebby-Strabley *et al.*, 2005] J. Sebby-Strabley, R. T. R. Newell, J. O. Day, E. Breeke, and T. G. Walker, "High Density Mesoscopic Atom Clouds in a Holographic Atom Trap", Phys. Rev. A **71**, 021401(R) (2005).

[Shor, 1996] P. Shor, "Polynomial-Time Algorithms for Prime Factorization and Discrete Logarithms on a Quantum Computer", arXiv:quant-ph/9508027v2 (1996).

[Siegman, 1986] A. E. Siegman, *Lasers*, (University Science Books, Sausalito, CA, 1986.)

[Simien *et al.*, 2004] C. E. Simien, Y. C. Chen, P. Gupta, S. Laha, Y. N. Martinez, P. G. Mickelson, S. B. Nagel, and T. C. Kilian, "Using Absorption Imaging to Study Ion Dynamics in an Ultracold Neutral Plasma", Phys. Rev. Lett. **92**, 143001 (2004).

[Singer *et al.*, 2004] K. Singer, M. Reetz-Lamour, T. Amthor, L. G. Marcassa, and M. Weidemüller, "Suppression of Excitation and Spectral Broadening Induced by

Interaction in a Cold Gas of Rydberg Atoms," Phys. Rev. Lett. **93**, 163001 (2004).

[Singer *et al.*, 2005] K. Singer, M. Reetz-Lamour, T. Amthor, S. Fölling, M. Tscherneck, and M. Weidemüller, "Spectroscopy of an ultracold Rydberg gas and signatures of Rydberg-Rydberg interactions", J. Phys. B **38**, S321 (2005).

[Stenholm, 1984] S. Stenholm, *Foundations of Laser Spectroscopy*, (John Wiley & Sons, New York, 1984.)

[Sutherland, 2003] R. L. Sutherland, *Handbook of Nonlinear Optics*, 2nd. Ed., (Marcel Dekker, Inc., New York, 2003.)

[Svanberg, 2001] S. Svanberg, *Atomic and Molecular Spectroscopy*, 3rd. Ed. (Springer, New York, 2001.)

[Teo *et al.*, 2003] B. K. Teo, D. Feldbaum, T. Cubel, J. R. Guest, P. R. Berman, and G. Raithel, "Autler-Townes spectroscopy of the $5S_{1/2} - 5P_{3/2} - 44D$ cascade of Cold ^{85}Rb atoms", Phys. Rev. A **68**, 053407 (2003).

[Tong *et al.*, 2004] D. Tong, S. M. Farooqui, J. Stanojevic, S. Krishnan, Y. P. Zhang, R. Cote, E. E. Eyler, and P. L. Gould, "Local Blockade of Rydberg Excitation in an Ultracold Gas", Phys. Rev. Lett. **93**, 016406 (2004).

[Urban *et al.*, 2008] E. Urban, T. A. Johnson, T. Henage, L. Isenhower, D. D. Yavuz, T. G. Walker, and M. Saffman , "Observation of Rydberg blockade between two atoms", arXiv:0805.0758v1 (2008).

[Walker and Saffman, 2005] T. G. Walker and M. Saffman, "Zeros of Rydberg-Rydberg Föster Interactions", J. Phys. B **38**, S309 (2005).

[Walker and Saffman, 2008] T. G. Walker and M. Saffman, " Consequences of Zeeman degeneracy for the van der Waals blockade between Rydberg atoms", Phys. Rev. A **77**, 032723 (2008).

[Walz-Flannigan *et al.*, 2004] A Walz-Flannigan, J. R. Guest, J.-H. Choi, and G. Raithel, "Cold-Rydberg-gas dynamics", Phys. Rev. A **69**, 063405 (2004).

[Wang *et al.*, 2007] T. Wang, S. F. Yelin, R. Côté, E. E. Eyler, S. M. Farooqi, P. L. Gould, M. Koštrun, D. Tong, and D. Vrinceanu, "Superradiance in ultracold Rydberg gases", Phys. Rev. A **75**, 033802 (2007).

[Weissbluth, 1978] M. Weissbluth, *Atoms and Molecules*, (Academic Press, New York, 1978.)

[Yariv, 1971] A. Yariv, *Introduction to Optical Electronics*, (Holt, Rinehart and Winston, Inc., New York, 1971.)

[Yavuz *et al.*, 2006] D. D. Yavuz, P. B. Kulatunga, E. Urban, T. A. Johnson, N. Proite, T. Henage, T. G. Walker, and M. Saffman, "Fast Ground State Manipulation of Neutral Atoms in Microscopic Optical Traps", Phys. Rev. Lett. **96**, 063001 (2006).